The Hong Kong Polytechnic University

Department of Electronic & Information Engineering

Landmobile Communication-Channel Modelling & Microphone-Array Source Localization

WU, Yue

A thesis submitted in partial fulfilment of the requirements

for the degree of Doctor of Philosophy

November 2009

CERTIFICATE OF ORIGINALITY

I hereby declare that this thesis is my own work and that, to the best of my knowledge and belief, it reproduces no material previously published or written, nor material that has been accepted for the award of any other degree or diploma, except where due acknowledgement has been made in the text.

_____ (Signed)

_____ (Name of Students)

Abstract

The dissertation has three distinct but loosely complimentary components, which are briefly concluded below.

(1) Geometric modeling of landmobile radiowave propagation channels.

"Geometric modeling" idealizes the spatial geometric relationships among the transmitter, the scatterers, and the receiver in a wireless propagation channel - to produce closed-form formulas of various channel-fading metrics, (such as the distribution of the direction of arrival (DOA) and distribution of the time of arrival (TOA)) using only a very few degrees-of-freedom. In Chapter 2, we thoroughly assessed geometric models in terms of their DOA-distributions against all empirical data available from the open literature. In Chapter 3 a new model for the uplink/downlink multipahs' TOA-distribution is proposed, the proposed TOA-distribution is compared against some certain empirical data and can better fit them than the customary geometric models can.

(2) Near-field measurement model of a microphone-array called "acoustic vector-sensors"

The acoustic vector-sensor is a practical and versatile sound-measurement system in-room, open-air, or underwater. It consists of three identical but orthogonally oriented velocity-sensors plus a pressure-sensor, all spatially collocated. Though its far-field measurement-model has been known for over a decade, we, in chapter 4, pioneer its near-field measurement-model, based on rigorous acoustic physics. Section 4.1 to 4.3 derived the near-field model without any boundary near the acoustic vector-sensor, the closed-form CRB is derived and analyzed. Section 4.4 extends the measurement model from being without boundary to being with a boundary case.

(3) Microphone array source localization algorithms

In chapter 5, we propose a new algorithm to geolocate a source in 3D near-field space using only one spatially spread acoustic vector-sensor. This algorithm requires no prior knowledge of the temporal structure of the impinging signal, nor any iterative solution. However, this method can allow only one incident source with constant emitting power - a limitation common to basically all "received signal Strength Indication" (RSSI) methods of geolocation. A new adaptive "beamforming" signal-processing algorithm is developed in chapter 6 to locate noise-sources

aboard a rail-car that passes by a track-side immobile microphone-array. This proposed microphone-array beamformer tracks the rail-car's spatial movement, with the aid of two inaudible acoustic beacons placed abroad the rail-car. The proposed scheme then localizes the noise-sources with reference to the rail-car's coordinates. No auxiliary infrastructure (e.g., no radar nor video-camera) is needed besides the onboard beacons. Monte Carlo simulations and anechoic chamber experiments verify the proposed scheme's efficacy.

Publications

Journal Papers

1. **Y. I. Wu** & K. T. Wong, "A Geometric Model for the Uplink / Downlink Multipaths' TOA Distribution, Assuming the Scatterers of a Conical Spatial Density," *IEEE Antennas and Propagation Magazine*, vol. 50, no. 6, pp. 196-205, December 2008.

2. K. T. Wong & **Y. I. Wu**, "Spatio-Polarizational Correlation-Coefficient Function Between Receiving-Antennas in Radiowave Communications: Geometrically Modeled, Analytically Derived, Simple, Closed-Form, Explicit Formulas," accepted to appear in the December 2009 issue of *IEEE Transactions on Communications*.

3. K. T. Wong, **Y. I. Wu** & M. Abdulla, "Landmobile Radiowave Multipaths' DOA-Distribution: Assessing Geometric Models by the Open Literature's Empirical Datasets," accepted to appear in *IEEE Transactions on Antennas and Propagation*.

4. C.-L. J. Lam, K. T. Wong & **Y. I. Wu**, "The TOA-Distribution of Wireless Multipaths Between an Omni-Directional Transceiver & a Possibly Mis-Oriented Directional Transceiver," accepted to appear in *IEEE Transactions on Communications*.

5. **Y. I. Wu**, S. K. Lau, K. T. Wong & S. K. Tang, "Beacon-Aided Adaptive Localization of Noise-Sources Aboard a Pass-By Rail-Car Using a Track-Side Microphone-Array," under review by the *IEEE Transactions on Vehicular Technology*.

6. **Y. I. Wu**, K. T. Wong & Siu-Kit Lau, "The Acoustic Vector-Sensor's Near-Field Array-Manifold," under review by the *IEEE Transactions on Signal Processing*.

7. V. I. Piterbarg, K. T. Wong & **Y. I. Wu**, "Spatial Correlation-Coefficient Across the Base-Station's Receiving Sensor-Array — Analytically Derived, Closed-Form, and Accounting for Propagation Loss," under review by the *IEEE Antennas and Wireless Propagation Letters*.

Conference Papers

8. **Y. I. Wu** & K. T. Wong "Near-field Source Localization (over Azimuth / Elevation / Distance) Using a Single Spatially Extended Acoustic Vector-Sensor," accepted to appear on *IEEE Asia-Pacific Microwave Conference*, Singapore, 7-10 December, 2009.

9. **Y. I. Wu**, K. T. Wong & S. K. Lau, "Beacon-Aided Adaptive Azimuth-Elevation Localization of Sound-Sources aboard a Pass-By Rail-Car Using a Track-Side Acoustic Microphone Planar Array," *International Conference on Sensing Technology*, Tainan, Taiwan, 30 November to 3 December, 2008.

10. C.-L. J. Lam, K. T. Wong & **Y. I. Wu**, "Closed-Form Explicit Formula for the TOA-Distribution of Multipaths between a Mis-Aligned Directional Transceiver & an Omni-Directional Transceiver Enclosed among Scatterers," *International Symposium on Antennas & Propagation*, Taipei, Taiwan, 27-30 October, 2008.

11. **Y. I. Wu**, K. T. Wong & S. K. Lau, "Beacon-Aided Adaptive Localization of Sound-Sources aboard a Pass-By Rail-Car Using a Track-Side Acoustic Microphone Array," *Inter-Noise Conference*, Shanghai, China, 26-29 October, 2008.

Acknowledgments

I would like to thank my beloved family for its support throughout my student career.

I would like to thank my supervisor, Dr. Kainam Thomas Wong, for his guidance and great help during the past 3 years.

I would like to thank Dr. Siu-Kit Lau (Eddie), Dr. Petr Tichavsky, Chi-Ling Jerry Lam, Jeffrey Tam and many other research collaborators for their help to my work.

Contents

List of Figures

List of Tables

Chapter 1

Introduction

This dissertation presents much of the candidate student's research work during his past 2.5 years of study. The contents in this dissertation refer to 6 research projects, among which two have been published or accepted to publish in IEEE journals or magazines, two have been submitted to IEEE journals for peer-review, and two are under preparation.

This dissertation consists of six loosely related research topics, on geometric modeling of wireless channels (chapters 2-3) and on microphone array space-time processing (chapters 4-6).

1.1   The Motivation & Significance of the Investigation

In wireless communications, a transmitted signal reaches a receiver via multiple propagation paths, undergoing various sequences of reflection, diffraction, and scattering. Each such "multipath" carries its own propagation history, resulting in its particular amplitude, propagation delay, direction-of-arrival, polarization, and Doppler shift. At the receiving antenna, these multipaths are phasor-summed, constructively or destructively, to produce that antenna's measured data. Hence, the receiver "sees" the transmitter in space not as a geometrically point-like source, but as spatio-temporally spread over a range of time-of-arrival (TOA) and direction-of-arrival (DOA). It is important to model the wireless channel's DOA distribution at the receiver, for the development and analysis of smart-antennas spatial-diversity schemes, such as space-division frequency re-use, beamforming, emitter localization, etc. And it's also important to model the the wireless channel's TOA distribution at the receiver, because the TOA probability-density function characterizes the wireless propagation channel's temporal delay spread and frequency incoherence, which in turn determine the obtainable temporal diversity and the extent of inter-symbol interference in wireless communication. These constrain the capacity of information that can be communicated between the transmitter and the receiver. Hence, modeling the wireless propagation channel and investigating the DOA & TOA is always an active research area.

There exist various strategies to mathematically model the propagation channel. The most direct and the most site-specific approach is empirical measurement at the particular site / terrain / building of interest. Another approach, more labor-saving but still site-

specific, is to approximate the particular site under investigation as an electromagnetic-physics-based ray-tracing computer-model. These site-specific / terrain-specific / building-specific approaches are faithful to the particular site's idiosyncratic electromagnetic and spatio-temporal complexities. Each such simulation produces a quantitatively accurate model, but each simulation applies to only that one particular propagation setting under investigation (e.g., a particular city's particular cross-sectional street corner under a particular weather). With many simulations over many scenarios, the ray-tracing approach can be generalized to a wider class of environments (e.g., the class of "bad urban" settings of high-rises in all downtowns). In contrast, a "geometric model" can encapsulate the essence of a wide class of diverse propagation settings.

Between any communication transmitter and receiver, there lies the channel, from which much of the degradation effects arise. "Geometric modeling" idealizes the wireless electromagnetic propagation environment via a geometric abstraction of the spatial relationships among the transmitter, the scatterers, and the base-station. (For example, scatterers could be idealized as distributed evenly on only a small disc centered around the mobile) Geometric models attempt to embed measurable fading metrics (e.g., the DOA distribution) integrally into the propagation channel's idealized geometry, such that only a very few geometric parameters (e.g., the single model-parameter of the ratio between the aforementioned disc's radius R and the transmitter-receiver distance D) would affect these various fading metrics in an inter-connected manner, to conceptually reveal the channel's underlying geometric dynamics. This modeling's generic abstract geometry involves no site-specific or terrain-specific nor building-specific information, such as those used in empirical measurements or in ray-shooting / ray-tracing computer-simulation.

(Ch-2) Many geometric models have been proposed. However, numerous "geometric models" have emerged in the past decade, each based on a different spatial distribution of the scatterers. Each would thus offer a competing closed-form distribution-formula for the azimuth-DOA of the multipaths arriving at the receiver. Many authors proposed their geometric models without verification by empirical data, though a few were validated by a few empirical datasets pre-selected by the authors themselves. It remains unclear *which* "geometric model" is *how* best under *what* field scenarios and *why*. This literature gap is perhaps due to the labor-intensive nature of such an investigation. Chapter 2 aims to be an impartial third party, to thoroughly compare and contrast the accuracy of these competing geometric models' derived azimuth direction-of-arrival distribution in landmobile radiowave communications against the open literature's empirically measured data.

(Ch-3) Chapter 3 proposes a new geometric model for the arriving multipaths' TOA-distribution. The proposed model can better fit some certain empirical data from the field measurement in the open literature.

Besides modeling of the wireless propagation channel, to passively locate single/multiple sound sources in the wireless environment is also an important investigation topic in recent

years. In these localization problem, sensor array is typically and frequently used. In this thesis, two typical sensor array is presented, which are acoustic vector-sensor and customary two dimensional sensor-array. A new measurement model is proposed for the acoustic vector-sensor with sound source in its near-field. Some novel localization algorithms are also proposed in the later chapters.

An acoustic **vector**-sensor (a.k.a. vector-hydrophone) consists of three identical, but orthogonally oriented, acoustic velocity-sensors, plus an acoustic pressure-sensor — all spatially co-located in a point-like geometry. Each acoustic *velocity*-sensor measures one Cartesian component of the incident acoustic particle-field vector. The entire acoustic vector-sensor thus distinctly measures all three Cartesian components of the particle-velocity vector plus the pressure scalar. This contrasts with a customary microphone or hydrophone measuring only the acoustic pressure.

(Ch-4) Though a *far*-field measurement model was introduced to the signal-processing literature over a decade ago, the corresponding *near*-field measurement-model has not been investigated. This overlooked issue is herein investigated. As will be shown in the subsequent sections, the *far*-field measurement model's independence from the signal frequency, the source-sensor distance, and the propagation-medium in (4.1) is invalid for the *near*-field case. This is investigated in chapter 4.

(Ch-5) When the pressure-sensor is spatially separated from the velocity-sensor triad, the acoustic vector sensor can geolocate an emitter in three-dimensional space, not merely in two-dimensional space as mentioned earlier in chapter 4. This 3D geolocation (azimuth angle, elevation angle, and radial distance) is investigated in chapter 5.

(Ch-6) Chapter 6 uses a two-dimensional array of identical microphones to scan a pass-by train-carriage for any onboard noise sources. Like chapter 4 and 5, the emitters are taken to emit from the sensors' near-field. Moreover, the data are time-varying.

1.2 Literature Review

1.2.1 Literature Review of Geometric Modeling of Landmobile Wireless Channel

Numerous two-dimensional "geometric models" [98], [45], [144], [177], [91], [48], [143], [67], [133], [134] have been proposed for the radiowave outdoor landmobile cellular communication uplink's azimuth direction-of-arrival distribution. "Geometric models" typically model a multipath as the bouncing of the transmitted signal off one scatterer. A multipath's azimuth direction-of-arrival is thus determined by the spatial location of the scatterer off which the multipath is reflected before reaching the receiver. Hence, one pivotal character of any geometric model is how the model characterizes the scatterers' spatial distribution in relation to the transmitter and the receiver. Various geometric models differently idealize the scatterers' spatial distribution in relation to the transmitter and the

receiver. Table 2.3 comparatively summarizes these two-dimensional geometric models' contrasting scatterer spatial distributions and corresponding azimuth direction-of-arrival distributions.

All above-mentioned geometric models make these common assumptions:

a) All transmitting and receiving antennas are omni-directional.

b) Polarizational effects may be ignored.

c) Each propagation path, from the mobile to the base-station, reflects off exactly one scatterer.

d) Each scatterer acts (independently of other scatterers) as an omni-directional lossless re-transmitter.

e) Negligible complex-phase effects in the receiving-antenna's vector-summation of its arriving multipaths. That is, all arriving multipaths arriving at each receiving-antenna are assumed to be temporally in-phase among themselves.

All above models (except [91]) also ignore "propagation loss", i.e., the power loss experienced as a signal travels outwards from the transmitter, due to the signal wavefront's expanding area.

These models' different scatterer-distributions may be classified according to several perspectives:

A) Whether the scatterers surround only the transmitter, or surround also the receiver.

B) The shape of spatial density of the scatterers around the transmitter.

C) Unimodal vs. bimodal vs. multi-modal spatial densities for the scatterers.

For an elevated base-station receiver (Rx) in a macro-cell, most significant scatterers concentrate locally around the street-level transmitter (Tx) but away from the elevated receiver. Hence, a "geometric model" could idealize its scatterers' spatial support region as enclosing (and centering around) the mobile transmitter, but as excluding the base-station receiver itself. This is a "local scattering model" and is exemplified by the following models:

(1) a uniform density within a circular-disc support region of radius R, which is less than the transmitter-receiver separation D [45], [144], [177], [48], [143].

(2) a uniform density within a hollow circular-disc support region of outer radius $R \leq D$ [133]. Please refer to Figure 2.3a.

(3) an inverted-parabolic density within a circular-disc support region of radius $R \leq D$ [134].

(4) a conical density within a circular-disc support region of radius $R \leq D$ [45].

(5) a uniform density within an elliptical-disc support region centered at the transmitter but excluding the receiver [144].

On the other hand, for a micro-cell with a relatively low base-station height, significant scatterers may locate near the base-station. This is modeled with the scattering region enclosing both the base-station receiver and the mobile transmitter. The multipaths' DOAs could impinge from any direction 360°. The following models fall under this class.

(6) a uniform density within a circular-disc support region of radius $R > D$ [45], [177], [68].

(7) a uniform density within a support region of a 2β pie-shaped cut of a circular-disc of radius $R > D$ [68] (for a directional transmitter with a 2β azimuth beam-width). Please refer to Figure 2.3b.

(8) a conical density within a circular-disc support region of radius $R > D$ [45].

(9) a uniform density within an elliptical-disc support region focused at the transmitter and the receiver [48].

(10) a Gaussian density centered at the transmitter [67], [3], [15], [1].

(11) a Rayleigh density centered at the transmitter [91].[2]

The six "geometric models" in rows #1-4 and 8-9 of Table 2.3 have uniform densities; however, the remaining five models have unimodal densities peaking at the transmitter. Among the non-uniform densities, the "conical circular" model [45] has the most concentrated scatterers around the transmitter followed by the "inverted-parabolic circular (Rx outside)" model [134], then the "Rayleigh circular (Rx outside)" model [91], and lastly the "Gaussian" model [67] (which has an infinite spatial support region for the scatterers).

All aforementioned "geometric models" produce unimodal probability densities for the azimuth direction-of-arrival, except for the "uniform pie-cut (Rx inside)" model (row # 3 in Table 2.3) and the "uniform hollow-disc (Rx outside)" model (row # 4 in Table 2.3).

The "uniform hollow-disc (Rx outside)" model [133] has a bimodal DOA-density. It generalizes the "uniform circular (Rx outside)" model of [45], [144], [177], [48], [143]. Figure 2.3a shows the "uniform hollow-disc (Rx outside)" model's allowable locations for the scatterers. When the "uniform hollow-disc (Rx outside)" model has $r = 0$, it becomes the "uniform circular (Rx outside)" model. As $\frac{r}{R}$ increases for the "uniform hollow-disc (Rx outside)" model, the azimuth direction-of-arrival distribution's two peaks become narrower and "taller", as well as getting further apart from each other.

The "uniform pie-cut (Rx inside)" model has a trimodal DOA-density.

---

[1] The Gaussian spatial distribution is also investigated in [103], but its derived formula is $\frac{A}{2\sqrt{2\pi}\sigma} e^{\frac{D^2(\cos^2\theta - 1)}{2\sigma^2}} \text{erfc}\left(\frac{-D\cos\theta}{\sqrt{2}\sigma}\right)$. This formula disagrees with that derived in [67] for the same model and appears incorrect to the present authors. Hence, [103] will be ignored thereafter. Any subsequent reference to a Gaussian scatterer model would mean [67]

[2] The Rayleigh scatterer distribution of [91] assumes that $\frac{R}{D} \ll 1$, at which the DOA distribution would approach that of the Gaussian scatterer model in [67]. For $\frac{R}{D} \approx 1$, the DOA distribution $f_\theta(\theta)$ could become negative, unless (and unstated in [91] that) the azimuth angle, θ, is restricted to $\left(-\frac{\pi}{2}, \frac{\pi}{2}\right)$. This restriction turns out to be moot in this present work, as all empirical data-sets here satisfy the restriction.

1.2.2 Literature Review of Source Localization with Sensor Array

Source localization is increasingly important in the sensor network. [109] and [198] overview various localization methods which may be classified into 5 categories.

(1) Global Positioning System (GPS) offers very accurate localization, but requires complicated hardware at each sensor-node. GPS is expensive, power-hungry, hence unsuited for small networks or ad hoc networks.

(2) In the DOA (or AOA) approaches as [19], [87], [84], [28], [2], [94], [141], [75], [107], the source's DOA is estimated at each sensor-node with respect to that node, Each DOA-estimate constitute a straight line of possible locations of the emitter. The intersection of all such lines gives the emitter's location. This DOA-based approach requires at each node the complex and expensive hardware, e.g, antenna-array or ultrasound receiver.

(3) Ranging techniques, such as TOA/TDOA and (Receiving Signal Strength Indicator) RSSI. The TOA/TDOA approaches are often more accurate than RSSI approaches. However, the former approaches require highly accurate time-synchronization and iterative solution to the nonlinear equations. On the contrary, the RSSI-based approaches [96], [169], [30], [162], [29], [204], [90], [4], [49], and [197] require no additional hardware but are sensitive to any changes in the propagation environment.

(4) The Maximum Likelihood (ML) approaches [158], [131], [169], [204], [4], [130], [159], [112], and [182]. can be highly accurate, but require prior knowledge of the noise statistics, computationally an initial guess to start off the iteration.

1.3 Contributions of This Work

Listed below are the main contributions of my work presented in this thesis

(1) In chapter 2, numerous geometric models are compared, each advancing its own closed-form DOA formula, each based on a different idealization of the spatial geometry of the scatterers. Lacking in the open literature is a comprehensive and critical comparison among all such single-cluster geometric-model-based formulas of the arriving multipaths azimuth direction-of-arrival distribution. This work fills this literature gap. The comparison here uses all empirical data legibly available in the open literature for landmobile wireless radiowave propagation. No one geometric model is best by all criteria and for all environments. However, a safe choice is the model with a Gaussian density of scatterers centered at the transmitter. Despite this models simplicity of having only one degree of freedom, it is always either the best fitting model or offers an LSE within one third of an order-of-magnitude as the best fitting model for all empirical dataset of all environments.

(2) In chapter 3, A new geometric model is proposed and its TOA distributions of the uplink and downlink multipath is derived. In contrast to the customary uniform-disc

density, this "conical" scatterer density indirectly accounts for the multipath scattering power loss. These new TOA distribution formulas, herein derived explicitly in terms of the model's only two independent parameters, can better fit some empirical data than can all earlier models that also confine all scatterers to within a circular disc.

(3) The acoustic vector-sensor is a practical and versatile sound-measurement system, for applications in room, open-air, or underwater. Its far-field measurement model has been introduced into signal processing over a decade ago; and many direction-finding algorithms have since been developed for acoustic vector-sensors, but only for far-field sources. Missing in the literature is a near-field measurement model for the acoustic vector-sensor. Chapter 4 fills this literature gap.

(4) To localize a non-cooperative acoustic source, a new synergy is proposed in chapter 5. Unlike customary RSSI-based methods, the proposed approach needs only two (not three or more) passive anchor-nodes: one pressure-sensor, and one triad of three identical collocated acoustic velocity-sensors. This proposed algorithm is closed-form, non-iterative, requiring no initial estimate, and applicable to any path-loss exponent of known value.

(5) In chapter 6, a new adaptive "beamforming" signal-processing algorithm is developed to locate noise-sources aboard a rail-car that passes by a track-side immobile microphone-array. This proposed microphone array beamformer tracks the rail-cars spatial movement, with the aid of two inaudible acoustic beacons placed abroad the rail-car. The proposed scheme then localizes the noise-sources with reference to the rail-cars coordinates. No auxiliary infrastructure (e.g., no radar nor video-camera) is needed besides the onboard beacons. Monte Carlo simulations and anechoic chamber experiments verify the proposed schemes efficacy.

Chapter 2

Landmobile Radiowave Multipaths' DOA-Distribution : Assessing Geometric Models by the Open Literature's Empirical Datasets

2.1 Preliminary

2.1.1 Distribution of the Azimuth Direction-of-Arrival of the Arriving Multipaths

In wireless communications, a transmitted signal reaches a receiver via multiple propagation paths, undergoing various sequences of reflection, diffraction, and scattering. Each such "multipath" carries its own propagation history, resulting in its particular amplitude, propagation delay, direction-of-arrival, polarization, and Doppler shift. At the receiving antenna, these multipaths are phasor-summed, constructively or destructively, to produce that antenna's measured data. Hence, the receiver "sees" the transmitter in space not as a geometrically point-like source, but as spatio-temporally spread over a range of time-of-arrival (TOA) and direction-of-arrival (DOA). The above propagation phenomenon is labeled "small-scale fading", "local fading", or "microscopic fading" – because the multipaths' vector-summation would vary greatly in magnitude even if the receiver is displaced by a small distance at fractions of a wavelength. "Small-scale fading" is also called "fast fading", because a moving receiver would experience the small-scale fading's spatial variability as a fast temporal variability. "Small-scale fading" contrasts against "large-scale fading" (a.k.a. "slow fading"), which is caused by propagation-distance-related path-loss. "Small-scale fading" also contrasts against "shadowing", which is caused by sizeable obstacles blocking the receiver from the transmitter.

It is important to model the wireless channel's DOA distribution at the receiver, for

the development and analysis of smart-antennas spatial-diversity schemes, such as space-division frequency re-use, beamforming, emitter localization, etc. This DOA distribution may be obtained by "normalizing" the arriving multipaths' power distribution over all directions-of-arrival, by magnitude-scaling the multipaths' arrival-power distribution so that the power distribution sums to one over the entire range of the direction-of-arrival.

2.1.2 "Geometric Models" Versus Other Modeling Approaches of Microscopic Channel Fading

There exist various strategies to mathematically model the propagation channel. The most direct and the most site-specific approach is empirical measurement at the particular site / terrain / building of interest. Another approach, more labor-saving but still site-specific, is to approximate the particular site under investigation as an electromagnetic-physics-based ray-tracing computer-model. These site-specific / terrain-specific / building-specific approaches are faithful to the particular site's idiosyncratic electromagnetic and spatio-temporal complexities. Each such simulation produces a quantitatively accurate model, but each simulation applies to only that one particular propagation setting under investigation (e.g., a particular city's particular cross-sectional street corner under a particular weather). With many simulations over many scenarios, the ray-tracing approach can be generalized to a wider class of environments (e.g., the class of "bad urban" settings of high-rises in all downtowns). In contrast, a "geometric model" can encapsulate the essence of a wide class of diverse propagation settings.

"Geometric modeling" idealizes the wireless electromagnetic propagation environment via a geometric abstraction of the spatial relationships among the transmitter, the scatterers, and the base-station. (For example, scatterers could be idealized as distributed evenly on only a small disc centered around the mobile [45] [144] [177] [48] [143].) Geometric models attempt to embed measurable fading metrics (e.g., the DOA distribution) integrally into the propagation channel's idealized geometry, such that only a very few geometric parameters (e.g., the single model-parameter of the ratio between the aforementioned disc's radius R and the transmitter-receiver distance D) would affect these various fading metrics in an inter-connected manner to conceptually reveal the channel's underlying geometric dynamics. This modeling's generic abstract geometry involves no site-specific or terrain-specific or building-specific information, such as those used in empirical measurements or in any one ray-shooting / ray-tracing computer-simulation.

Much literature on "geometric models" involves little or no mathematically rigorous derivation of the received signal's measurable fading statistics, due to the inherent mathematical difficulties of such a rigorous derivation. Instead, a limited series of Monte Carlo simulations would approximate the numerical values of the channel-fading metrics. Such simulations can be performed only at relatively limited number of pre-set numerical values, which are geometrically independent of the model parameters. Hence, this would produce no closed-form mathematical relationship among the fading metrics, in terms of the geometric-model's independent parameters. Such simulations thereby limit the insight

obtainable from such a geometric model. This survey will focus only on those "geometric models" for which rigorous analytical derivation have closed-form expressions of the uplink azimuth direction-of-arrival distribution, explicitly in terms of the geometric parameters.

2.1.3 The Purpose of This Work

Geometric models of propagation-channels have been used in [24], [128], [53], [20], [150] (among others) to analytically predict the performance of communications systems (and not merely by computer-simulations). However, numerous "geometric models" have emerged in the past decade, each based on a different spatial distribution of the scatterers. Each would thus offer a competing closed-form distribution-formula for the azimuth-DOA of the multipaths arriving at the receiver. Many authors proposed their geometric models without verification by empirical data, though a few were validated by a few empirical datasets pre-selected by the authors themselves. It remains unclear *which* "geometric model" is *how* best under *what* field scenarios and *why*. This literature gap is perhaps due to the labor-intensive nature of such an investigation.

This present work aims to be an impartial third party, to thoroughly compare and contrast the accuracy of these competing geometric models' derived azimuth direction-of-arrival distribution in landmobile radiowave communications against the open literature's empirically measured data. More specifically, for every such empirical dataset available in the open literature (and listed in Tables 2.1 and 2.2), it is used herein to calibrate every known "geometric model" (listed in Table 2.3) for which a closed-form explicit formula has been analytically derived for the azimuth direction-of-arrival. Such two-dimensional modeling admittedly ignores the elevation, but often justifiably so, especially in a macro-cell situation where the transmitter-receiver separation would greatly exceeds the heights of the transmitter or the receiver. Conclusions are then drawn as to which, how, and why specific geometric models best fit what field situations.

Admittedly, partial listings of these "geometric models" can be found in [47], [99], [108]; however, those partial listings offer no comparative assessment of various "geometric models" against empirical data. This present work will complete this missing link.

The rest of this manuscript is organized as follows: Section 2.2 will survey various competing "geometric models". Section 2.3 will characterize the empirical data-sets to be used to calibrate the geometric models. Section 2.4 will define the least-squares errors (LSE) metric to measure how well any geometric model fits any empirical data-set, as well as fine points in the calibration algorithm. That section will also present calibration least-squares errors. Section 2.5.1 will discuss, for unimodal datasets, which "geometric models" best fits what types of field-scenarios and why, whereas Section 2.5.2 will do the same for bimodal or multi-modal datasets. Section 6.6 will conclude this work.

Table 2.1: Propagation & Measurement Environment for Empirical Datasets with a *Uni*-Modal Histogram.

Reference	Setting	Modal Type	Environment	Rx Height (m)	Tx Height (m)	LOS	Frequency (GHz)	Well-Fitting Model(s)	Model-Fitting Curves in Figure #
Matthews [113] Fig. 7	rural	unimodal	open site, valley area flats, and few buildings	55	47	yes	0.87	Rayleigh circular (Rx outside) & Gaussian	2.4
Pedersen [138] Fig. 1	rural	unimodal	unspecified	47	street level	yes	unspecified	Uniform elliptical (Rx outside)	2.5
Kuchar [85] Fig. 3	suburban	unimodal	3-5 storey buildings	50 on rooftop	50, on rooftop	yes	unspecified	Rayleigh circular (Rx outside) & Gaussian	2.6
Takada [168] Fig. 4	suburban	unimodal	residential area, 8-meter-high houses	4.4	2.7	no	8.45	Uniform elliptical (Rx outside)	2.7
Fleury [51] Fig. 16	urban	unimodal	downtown area 2 storey buildings	unspecified	unspecified	no	unspecified	Rayleigh circular (Rx outside), Gaussian & Uniform elliptical (Rx outside)	2.8
Mogensen [119] Fig. 3	urban	unimodal	irregular street layout 3-5 storey buildings a few taller buildings	41	street level	unspecified	1.8	Uniform elliptical (Rx outside)	2.9
Pedersen [140] Fig. 4 (Aarhus)	urban	unimodal	4-6 storey buildings, irregular street gird	32, on rooftop	street level	no	1.8	Uniform elliptical (Rx outside)	2.10
Pedersen [140] Fig. 4 (Stockholm)	urban	unimodal	4-6 storey buildings, irregular street gird	20, on rooftop	street level	no	1.8	Uniform elliptical (Rx inside) & Uniform elliptical (Rx outside)	2.11

Table 2.2: Propagation & Measurement Environment for Empirical Datasets with a *Non*-Uni-Modal Histogram.

Reference	Setting	Modal Type	Environment	Rx Height (m)	Tx Height (m)	LOS	Frequency (GHz)	Well-Fitting Model(s)	Model-Fitting Curves in Figure #
Matthews [113] Fig. 8	suburban	4-modal	open site, valley area flats, and few buildings	50	$\gg$ 50	no	0.87	Uniform pie-cut (Rx inside)	2.12
Pedersen [138] Fig. 5	urban	bimodal	4-7 story buildings	20	street level	no	unspecified	Uniform pie-cut (Rx inside)	2.13
Pedersen [140] Fig. 14	urban	bimodal	bad urban mixed with open areas, densely built up zones, 4-6 story buildings	21 on rooftop	street level	no	1.8	Uniform hollow-disc (Rx outside)	2.14
Kloch [83] Fig. 6 Blaunstein [17] Fig. 3	urban	bimodal	downtown area 2 story buildings	street level	4	unspecified	1.845	Uniform hollow-disc (Rx outside) & Uniform circular (Rx inside)	2.15
Eggers [46] Fig. 6	urban	4-modal	4-5 story buildings industrial buildings at the river shore.	40	street level	yes	2.145	Uniform pie-cut (Rx inside)	2.16

Table 2.3: Two-dimensional "geometrical models" for outdoor radiowave cellular communication's uplink azimuth direction-of-arrival distribution:

(D denotes the spatial separation between the base-station receiver and the mobile transmitter. The azimuth angle θ is defined with respect to the axis linking the mobile to the base-station.)

Reference	Scatterers' Spatial Distribution	Azimuth Direction-of-Arrival (DOA) Distribution $f_\theta(\theta)$ (where $f_\theta(\theta) \neq 0$)	$f_\tau(\tau)$
Eggers[45] Piechocki[144] Van Rheeden[177] Ertel[48] Petrus[143]	**Uniform circular (Rx outside):** uniform density on a circular-disc support region of radius $R \leq D$ & centered at Tx	$\frac{2}{\pi} \frac{D}{R} \cos\theta \sqrt{1 - \left(\frac{D}{R}\sin\theta\right)^2}$, $\forall |\theta| \in \left[0, \arcsin\frac{R}{D}\right]$	(42) in [48]
Eggers[45] Van Rheeden[177] Jiang[68]	**Uniform circular (Rx inside):** uniform density on a circular-disc support region of radius $R > D$ & centered at Tx	$\frac{1}{2\pi}\left(\frac{D}{R}\cos\theta + \sqrt{1 - (\frac{D}{R})^2 \sin^2\theta}\right)^2$, $\forall |\theta| \in [0, \pi]$	(8) of [70]
Jiang [68]	**Uniform pie-cut (Rx inside):** uniform density on a 2β pie-cut support region from a circular-disc of radius $R > D$ & centered at the Tx	$\left(\frac{D}{R}\right)^2 \cdot \frac{\sin^2\beta}{2\beta\sin^2(\beta+|\theta|)}$, $|\theta| \leq \theta_m$ $\frac{1}{2\beta}\left[\frac{D}{R}\cos\theta + \sqrt{1-\left(\frac{D}{R}\right)^2\sin^2\theta}\right]^2$, $|\theta| > \theta_m$ $\theta_m = \arcsin\left[\frac{\sin\beta}{\sqrt{1+\left(\frac{D}{R}\right)^2 - 2\frac{D}{R}\cos\beta}}\right]$, $\frac{D}{R} \geq \cos\beta$ $\theta_m = \pi - \arcsin\left[\frac{\sin\beta}{\sqrt{1+\left(\frac{D}{R}\right)^2 - 2\frac{D}{R}\cos\beta}}\right]$, $\frac{D}{R} < \cos\beta$	(10) of [70]
Olenko [133]	**Uniform hollow-disc (Rx outside):** uniform density on an hollow-disc support region centered around Tx, with outer radius $R \leq D$, & inner radius $r < R$	$\frac{2\cos\theta}{\pi} \frac{\sqrt{\left(\frac{R}{D}\right)^2 - \sin^2\theta} - \sqrt{\left(\frac{r}{D}\right)^2 - \sin^2\theta}}{\left(\frac{R}{D}\right)^2 - \left(\frac{r}{D}\right)^2}$, $\forall |\theta| \in \left[0, \arcsin\frac{r}{D}\right]$ $\frac{2\cos\theta}{\pi} \frac{\sqrt{\left(\frac{R}{D}\right)^2 - \sin^2\theta}}{\left(\frac{R}{D}\right)^2 - \left(\frac{r}{D}\right)^2}$, $\forall |\theta| \in \left[\arcsin\frac{r}{D}, \arcsin\frac{R}{D}\right]$	(9) in [133]
Olenko [134]	**Inverted-parabolic circular (Rx outside):** inverted parabolic density on a circular-disc support region of radius $R \leq D$ & centered at Tx	$\frac{8\cos\theta}{3\pi}\left(\frac{D}{R}\right)^4 \left[\left(\frac{R}{D}\right)^2 - \sin^2\theta\right]^{\frac{3}{2}}$, $\forall |\theta| \in \left[0, \arcsin\frac{R}{D}\right]$	(6) in [134]
Eggers [45]	**Conical circular (Rx outside):** conical density on a circular-disc support region of radius $R \leq D$ centered at Tx	$\frac{3}{2\pi}\frac{D}{R}(\cos\theta)\left\{2\sqrt{1 - \left(\frac{D}{R}\sin\theta\right)^2}\right.$ $\left. - \left(\frac{D}{R}\sin\theta\right)^2 \ln\left(\frac{1+\sqrt{1-\left(\frac{D}{R}\sin\theta\right)^2}}{1-\sqrt{1-\left(\frac{D}{R}\sin\theta\right)^2}}\right)\right\}$ $\forall |\theta| \in \left[0, \arcsin\frac{R}{D}\right]$	not derived
Eggers [45]	**Conical circular (Rx inside):** conical density on a circular-disc support region of radius $R > D$ centered at Tx	$\frac{3}{2\pi}\left\{\frac{1}{3} + \frac{2}{3}\left(\frac{D}{R}\right)^3 - \left(\frac{D}{R}\right)^2 + \frac{D}{R}(\cos\theta)\right.$ $\left[\left(2\frac{D}{R} - \left(\frac{D}{R}\right)^2\right)\cos\theta + \sqrt{1-\left(\frac{D}{R}\sin\theta\right)^2}\right.$ $\left.\left. - \left(\frac{D}{R}\sin\theta\right)^2 \ln\left(\frac{1+\sqrt{1-\left(\frac{D}{R}\sin\theta\right)^2}}{\frac{D}{R} - \frac{D}{R}\cos\theta}\right)\right]\right\}$, $\forall |\theta| \in [0, \pi]$	not derived
Piechocki [144]	**Uniform elliptical (Rx outside):** uniform density on an elliptical-disc support region of major-axis $2a$ & minor-axis $2b < 2a \leq D$, centered at Tx but excluding the Rx.	$\frac{2b^3 D^2}{\pi a^5} \cdot \frac{\cos\theta\left[\cos^2\theta - \left(\cos^2\theta + \frac{a^2}{b^2}\sin^2\theta\right)\left(1 - \frac{a^2}{D^2}\right)\right]^{\frac{1}{2}}}{\left(\frac{b^2}{a^2}\cos^2\theta + \sin^2\theta\right)^2}$, $\forall |\theta| \in [0, \theta_{\max})$ $\theta_{\max} = \arctan\left[\frac{b}{a}\tan\left(\arcsin\frac{a}{D}\right)\right]$	(24) in [164]
Liberti[98] Ertel[48] Khan[78]	**Uniform elliptical (Rx inside):** uniform density on an elliptical-disc support region focussed on Tx & Rx, of major axis L	$\frac{1}{2\pi \frac{L}{D}\sqrt{\left(\frac{L}{D}\right)^2 - 1}}\left[\frac{\left(\frac{L}{D}\right)^2 - 1}{\frac{L}{D} - \cos\theta}\right]^2$, $\forall |\theta| \in [0, \pi]$	(41) in [48]
Janaswamy[67] Andrade[3] Bevan[15]	**Gaussian:** Gaussian intensity with variance σ^2 & centered at Tx	$\frac{1}{2\pi}e^{\frac{-D^2}{2\sigma^2}} + \frac{D\cos\theta}{2\sqrt{2\pi}\sigma}e^{\frac{D^2(\cos^2\theta - 1)}{2\sigma^2}}\text{erfc}\left(\frac{-D\cos\theta}{\sqrt{2}\sigma}\right)$, $\forall |\theta| \in [0, \pi]$	not in closed form
Laurila [91]	**Rayleigh circular (Rx outside):** Rayleigh intensity with parameter $R \ll D$, & centered at Tx	$\frac{1}{2\pi}e^{-\frac{1}{2}\left(\frac{D}{R}\right)^2}$ $\left\{1 + \text{erf}\left(\frac{\cos\theta}{\sqrt{2}}\frac{D}{R}\right)\right\}\left\{1 + \sqrt{\frac{\pi}{2}}\frac{D}{R}(\cos\theta)e^{\frac{1}{2}\left(\frac{D}{R}\cos\theta\right)^2}\right\}$, $|\theta| \in [0, \pi]$	not in closed form

2.2 The Candidate "Geometric Models" for the Arriving Multipaths' Azimuth-DOA Distribution

Numerous two-dimensional "geometric models" [98], [45], [144], [177], [91], [48], [143], [67], [133], [134] have been proposed for the radiowave outdoor landmobile cellular communication uplink's azimuth direction-of-arrival distribution. "Geometric models" typically

26

model a multipath as the bouncing of the transmitted signal off one scatterer. A multipath's azimuth direction-of-arrival is thus determined by the spatial location of the scatterer off which the multipath is reflected before reaching the receiver. Hence, one pivotal character of any geometric model is how the model characterizes the scatterers' spatial distribution in relation to the transmitter and the receiver. Various geometric models differently idealize the scatterers' spatial distribution in relation to the transmitter and the receiver. Table 2.3 comparatively summarizes these two-dimensional geometric models' contrasting scatterer spatial distributions and corresponding azimuth direction-of-arrival distributions. Figures 2.1 and 2.2 graphically contrast these direction-of-arrival distributions at comparable model parameter values.
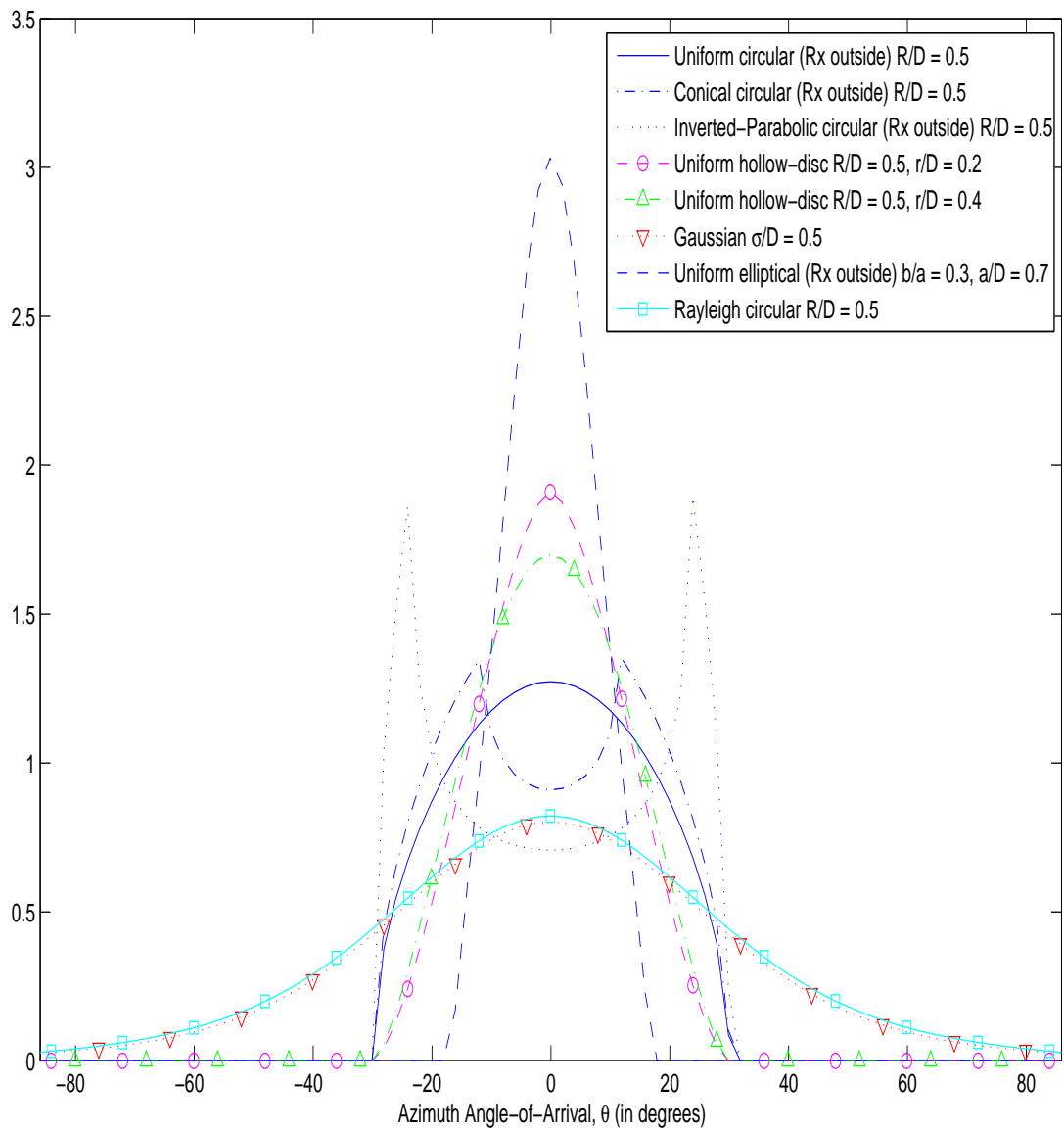
Figure 2.1: Azimuth DOA distributions for various "Rx outside" geometric models
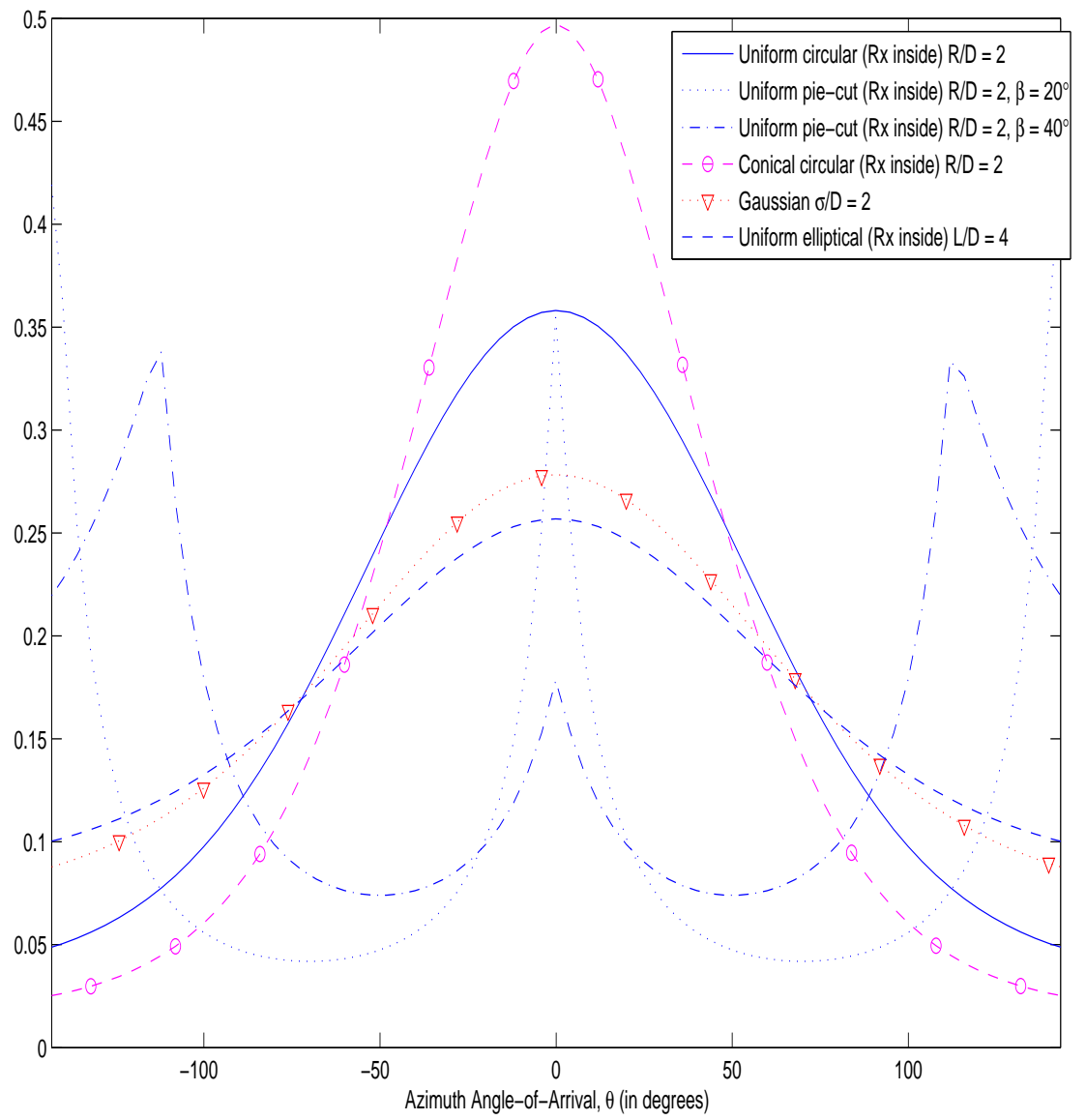
Figure 2.2: Azimuth DOA distributions for various "Rx inside" geometric models

All above-mentioned geometric models make these common assumptions:

a) All transmitting and receiving antennas are omni-directional.

b) Polarizational effects may be ignored.

c) Each propagation path, from the mobile to the base-station, reflects off exactly one scatterer.

d) Each scatterer acts (independently of other scatterers) as an omni-directional lossless re-transmitter.

e) Negligible complex-phase effects in the receiving-antenna's vector-summation of its arriving multipaths. That is, all arriving multipaths arriving at each receiving-antenna are assumed to be temporally in-phase among themselves.

All above models (except [91]) also ignore "propagation loss", i.e., the power loss experienced as a signal travels outwards from the transmitter, due to the signal wavefront's expanding area.

These models' different scatterer-distributions may be classified according to several perspectives:

A) Whether the scatterers surround only the transmitter, or surround also the receiver.

B) The shape of spatial density of the scatterers around the transmitter.

C) Unimodal vs. bimodal vs. multi-modal spatial densities for the scatterers.

The following subsections will analyze these categories one by one.

2.2.1 Geometric-Model Classification by Whether the Receiver Lies Within / Outside the Scatterers' Spatial Region

For an elevated base-station receiver (Rx) in a macro-cell, most significant scatterers concentrate locally around the street-level transmitter (Tx) but away from the elevated receiver. Hence, a "geometric model" could idealize its scatterers' spatial support region as enclosing (and centering around) the mobile transmitter, but as excluding the base-station receiver itself. This is a "local scattering model" and is exemplified by the following models:

(1) a uniform density within a circular-disc support region of radius R, which is less than the transmitter-receiver separation D [45], [144], [177], [48], [143].

(2) a uniform density within a hollow circular-disc support region of outer radius $R \leq D$ [133]. Please refer to Figure 2.3a.

(3) an inverted-parabolic density within a circular-disc support region of radius $R \leq D$ [134].

(4) a conical density within a circular-disc support region of radius $R \leq D$ [45].

(5) a uniform density within an elliptical-disc support region centered at the transmitter but excluding the receiver [144].

On the other hand, for a micro-cell with a relatively low base-station height, significant scatterers may locate near the base-station. This is modeled with the scattering region enclosing both the base-station receiver and the mobile transmitter. The multipaths' DOAs could impinge from any direction 360°. The following models fall under this class.

(6) a uniform density within a circular-disc support region of radius $R > D$ [45], [177], [68].

(7) a uniform density within a support region of a 2β pie-shaped cut of a circular-disc of radius $R > D$ [68] (for a directional transmitter with a 2β azimuth beam-width). Please refer to Figure 2.3b.

(8) a conical density within a circular-disc support region of radius $R > D$ [45].

(9) a uniform density within an elliptical-disc support region focused at the transmitter and the receiver [48].

(10) a Gaussian density centered at the transmitter [67], [3], [15], [1].

(11) a Rayleigh density centered at the transmitter [91].[2]

2.2.2 Geometric-Model Classification by the Spatial Concentration of the Scatterers Around the Transmitter

The six "geometric models" in rows #1-4 and 8-9 of Table 2.3 have uniform densities; however, the remaining five models have unimodal densities peaking at the transmitter. Among the non-uniform densities, the "conical circular" model [45] has the most concentrated scatterers around the transmitter followed by the "inverted-parabolic circular (Rx outside)" model [134], then the "Rayleigh circular (Rx outside)" model [91], and lastly the "Gaussian" model [67] (which has an infinite spatial support region for the scatterers).

The greater concentration of scatterers can be intuitively justified as follows: Recall that all aforementioned "geometric models" idealize every scatterer as an omni-directional lossless transmitter, thereby overlooking any power loss due to scattering. A unimodal concentration is an indirect way to account for this neglected scattering loss. The bounce off a distant scatterer in the model may correspond to only the last bounce in an actual

---

[1]The Gaussian spatial distribution is also investigated in [103], but its derived formula is $\frac{A}{2\sqrt{2\pi}\sigma} e^{\frac{D^2(\cos^2\theta-1)}{2\sigma^2}} \operatorname{erfc}\left(\frac{-D\cos\theta}{\sqrt{2}\sigma}\right)$. This formula disagrees with that derived in [67] for the same model and appears incorrect to the present authors. Hence, [103] will be ignored thereafter. Any subsequent reference to a Gaussian scatterer model would mean [67]

[2]The Rayleigh scatterer distribution of [91] assumes that $\frac{R}{D} \ll 1$, at which the DOA distribution would approach that of the Gaussian scatterer model in [67]. For $\frac{R}{D} \approx 1$, the DOA distribution $f_\theta(\theta)$ could become negative, unless (and unstated in [91] that) the azimuth angle, θ, is restricted to $\left(-\frac{\pi}{2}, \frac{\pi}{2}\right)$. This restriction turns out to be moot in this present work, as all empirical data-sets here satisfy the restriction.

Figure 2.3a: The support region of the "uniform hollow-disc (Rx outside)" model

Figure 2.3b: The support region of the "uniform pie-cut (Rx inside)" model

sequence of consecutive physical reflections farther and farther away from mobile. Each such reflection incurs power loss. Hence, the farther from the transmitter is a scatterer, the weaker its reflected path would be in actuality. Rather than accounting for such scattering-loss explicitly in the mathematical derivation, it is mathematically simpler to assume a denser distribution of "last-bounce" scatterers closer to the transmitter.

Far-off scatterers (like mountains, high-rises) could increase the angular spread and may be accounted for in the "geometric model" by a larger scattering area. A larger "normalized" radius $\frac{R}{D}$ leads to less concentration of scatterers around the receiver.

For $R \leq D$, the various "circular-disc (Rx outside)" models [45], [144], [177], [48], [143], [134] or "uniform hollow-disc (Rx outside)" model [133] can have multipaths arriving from only $|\theta| \in \left[0, \arcsin\left(\frac{R}{D}\right)\right]$. The circular-disc models' azimuth-DOA distribution's unimodal peak would have a width equal to $2\arcsin(R/D)$ radians in the azimuth direction-of-arrival. As $\frac{R}{D}$ decreases, $f_\theta(\theta)$ becomes narrower and "taller", such that $f_\theta(\theta) \to \delta(\theta)$ as $\frac{R}{D} \to 0$. Similar trends hold for the "Gaussian" model's σ [67], the "Rayleigh circular (Rx outside)" model's R [91], and the "uniform elliptical (Rx outside)" model's a [144].

2.2.3 Geometric-Model Classification by the Modality of the Scatterers' Spatial Density: Unimodal, Bimodal, or Multi-modal

All aforementioned "geometric models" produce unimodal probability densities for the azimuth direction-of-arrival, except for the "uniform pie-cut (Rx inside)" model (row # 3 in Table 2.3) and the "uniform hollow-disc (Rx outside)" model (row # 4 in Table 2.3).

The "uniform hollow-disc (Rx outside)" model [133] has a bimodal DOA-density. It generalizes the "uniform circular (Rx outside)" model of [45], [144], [177], [48], [143]. Figure 2.3a shows the "uniform hollow-disc (Rx outside)" model's allowable locations for the scatterers. When the "uniform hollow-disc (Rx outside)" model has $r = 0$, it becomes

the "uniform circular (Rx outside)" model. As $\frac{r}{R}$ increases for the "uniform hollow-disc (Rx outside)" model, the azimuth direction-of-arrival distribution's two peaks become narrower and "taller", as well as getting further apart from each other.

The "uniform pie-cut (Rx inside)" model has a trimodal DOA-density.

2.3   Empirical Data from the Open Literature

Spread through the open literature are empirical data for the uplink azimuth direction-of-arrival's distribution in radiowave wireless landmobile communications. The present authors have done an exhaustive search for such empirical data, which are listed in Tables 2.1 and 2.2. Surprisingly, only about a dozen *readable* data-sets can be located. To assure consistence in extracting numerical data from data graphs, the present authors use the software GetData instead of human visual reading. See http://www.getdata.com/

Excluded from Table 2.1 and Table 2.2 are many illegible graphical data from the open literature, often presented in poor-quality three-dimensional plots or contour maps, from which no numerical data can be reliably extracted. Examples of such numerically illegible empirical datasets include: Figure 7, 11, 13, 17 and 19 of Laurila [92]; Figure 8 and 9 of DeJong [36]; Figure 5, 9 and 10 of DeJong [37]; Figure 4 of DeJong [38]; Figure 5, 8, 9, 13, 14, 16, and 21 of Kuchar [86]; Figure 9 of Martin [111]; Figure 15-18 of Steinbauer [166]; Figure 7 and 8 of Thoma [171]; Figure 11 of Zhao [207]; Figure 6-9 of Zhu [208]; Figure 6 of Zhu [209]; Figure 1 of Toeltsch [174]; Figure 4 of Blanz [16]; Figure 4 and 6 of Kalliola [74]; Figure 1 of Larsson [89].

Table 2.1 and Table 2.2 describe each numerically legible empirical data-set's physical environment and setting, the channel-sounding signal's frequency, heights of the transmitting antenna and the receiving antenna – where such information is given in the corresponding reference. However, not all references give all of the above information.

Table 2.1's and Table 2.2's data-sets will provide the basis on which to compare what geometric model(s) can best describe what types of empirical propagation environment. The open literature appears to offer no such systematic and comparative validation of various competing geometric models. This literature gap is filled by this work.

Table 2.1's and Table 2.2's data-sets may be classified by the measurement's field environment and by the measured data's histogram shape:

2.3.1   Empirical Data-Set Classification by "Rural" vs. "Suburban" vs. "Urban"

The measurement's field environments may be roughly divided into the categories of "rural", "suburban", or "urban":

(R) The "rural" environment consists of flat or hilly terrains with large open spaces. It is mainly nature, possibly with forests or very few buildings.

(S) The "suburban" environment consists of small buildings of 3 to 5 stories, with much

less open space than does the rural environment. An example is a suburban residential neighborhood in North America.

(U) The "urban" environment consists of high-rises with narrow streets and no open space. An example is a downtown metropolis.

These categories are admittedly fuzzy but nonetheless often used in the literature. The "suburban" versus "urban" classification partly depends on the researcher's location. Many European "urban" environments may well be considered as "sub-urban" in Northeast Asia. Moreover, as subsequent sections will show, a equally critical consideration is the height of the transmitting antenna or receiving antenna relative to the surrounding buildings' height. Nonetheless, Table 2.1's and Table 2.2's rural / suburban / urban classification mostly honors each paper's own self-characterization.[3] The following datasets have no self-classification: Figures 7 and 8 in Matthews [113], Figure 6 in Kloch [83].

2.3.2 Empirical Data-Set Classification by Histogram's Modality

Another classification criterion is by the measured data's histogram shape. Table 2.1 lists all unimodal datasets, whereas Table 2.2 lists all bimodal and higher-modal datasets. This division will aid comparison with the "geometric models", most of which are unimodal but one is bimodal and another is trimodal. Among Table 2.2's five non-unimodal empirical data sets: four are "urban", only one is "suburban", and none is "rural". This is intuitively reasonable, because multiple clusters of scatterers are more likely in densely built-up environments.

2.4 The Goodness-of-Fit Metric & the Calibration Results

For each empirical dataset available in Table 2.1 and Table 2.2, this paper will use that dataset to calibrate each "geometric model" in Table 2.3. Conclusions will then be drawn in the next section as to what, how, when and why specific geometric models best fit what field situations.

The goodness-of-fit of any calibrated geometric model to the calibrating empirical data-set is the least-squares error (LSE) between the two. The first calibration-step is to normalized each empirical dataset to give unity area under the data-set, to match the unity area under each geometric-model's DOA density-distribution. The least-squares error (LSE) is defined as:

$$\text{LSE} \;=\; \frac{1}{N} \sum_{n=1}^{N} \left[y_n - f_\theta \left(\theta_n - \theta^{(0)} \right) \right]^2 \tag{2.1}$$

where $\{(\theta_n, y_n), \; n = 1, \dots, N\}$ denotes the normalized empirical dataset, $f_\theta(.)$ represents the geometric model's azimuth direction-of-arrival density distribution, N refers to

---

[3]The dataset from [83] is re-classified from "suburban" to "urban", because its receiving antenna was on the street level and was surrounded by two-storey buildings. The dataset from Figure 3 in [85] is re-classified here as "urban", despite its self-classification as "suburban". This re-classification is because both the transmitter and the receiver were placed atop buildings, thereby allowing LOS propagation.

the dataset's number of data points, and $\theta^{(0)}$ is a nuisance-parameter to align the data-set's transmitter-receiver line-of-sight DOA. Many empirical datasets do not state this transmitter-receiver line-of-sight DOA. The calibration here will search through all values of $\theta^{(0)}$ to identify the LSE. Note also that $\{\theta_n,\ n = 1, \ldots, N\}$ may be unevenly spaced along the θ coordinate. When a reference paper graphically presents its empirical data as curves, $\{\theta_n,\ n = 1, \ldots, N\}$ will be evenly spaced because a uniform grid is used with the GetData software. However, $\{\theta_n,\ n = 1, \ldots, N\}$ may be non-uniformly spaced when the reference presents its data as discrete icons. Moreover, $[f_\theta(-\infty), f_\theta(\theta_1)) \uplus (f_\theta(\theta_N), f(\infty)]$ does not contribute to the LSE. For most empirical data sets, y_n is not near zero for $n \approx 1$ or $n \approx N$. Hence, it is unlikely that y_n were zero for $\theta < \theta_1$ or for $\theta > \theta_N$. Rather, the empirical dataset has been truncated on both ends of the histogram. Consequently, the LSE should be computed only for $\theta \in [\theta_1, \theta_N]$.

Table 2.4 lists the LSE for each of Table 2.3's geometric model, calibrated by each empirical data-set of Tables 2.1 and 2.2. The geometric models, that "well fit" each empirical dataset of Tables 2.1 and 2.2, are listed in the second-to-last column thereof. This includes any geometric model with a calibration-LSE within 110% of the best-fitting geometrical model's. Figures 2.4 to 2.14 each plot one empirical data-set of Tables 2.1 and 2.2, along with the DOA-distributions of the geometric models calibrated to that empirical data-set.

Table 2.4: Least-Square Errors (LSE) When Each "Geometrical Model" of Table 2.3 is Calibrated by Each Empirical Data-Set of Tables 2.1 and 2.2.

Reference		Matthews [113] Fig. 7	Pedersen [138] Fig. 1	Kuchar [85] Fig. 3	Takada [168] Fig. 4	Matthews [113] Fig. 8	Fleury [51] Fig. 16	Mogensen [119] Fig. 3	Pedersen [140] Fig. 4 Aarhus	Pedersen [140] Fig. 4 Stockholm	Pedersen [138] Fig. 5	Pedersen [140] Fig. 14	Kloch [83] Fig. 6	Eggers [46] Fig. 6
Setting		R	R	S	S	S	U	U	U	U	U	U	U	U
Uniform circular (Rx outside)	LSE	0.020934	9.9512	0.054238	0.29076	0.027377	0.058121	0.080796	0.5247	0.24605	1.3376	0.17065	0.0077162	0.09473
	$\frac{R}{D}$	0.23	0.04	0.2	0.06	0.01	0.19	0.18	0.14	0.25	0.19	1	1	1
Uniform circular (Rx inside)	LSE	0.29533	68.806	0.52424	2.7471	0.026014	0.31762	0.37981	2.681	1.0186	4.044	0.16572	**0.0037308**	0.08117
	$\frac{R}{D}$	1.0101	1.0101	1.0101	1.0101	1.2048	1.0101	1.0101	1.0101	1.0101	1.0101	1.2195	**1.1905**	1.4286
Uniform Pie-cut (Rx inside)	LSE	0.060911	2.6735	0.11829	0.42063	**0.018143**	0.059188	0.067282	0.17247	0.092347	**0.58869**	0.094049	0.0099959	**0.04808**
	$\frac{R}{D}, \beta$	1, 7°	1, 1°	1, 5°	1, 2°	**1.11, 19°**	1, 5°	1, 6°	1, 3°	1, 6°	**1, 4°**	1, 137°	1, 46°	**1.1, 21°**
Uniform hollow-disc, (Rx outside)	LSE	0.020948	9.9529	0.05426	0.29078	0.025019	0.058151	0.080841	0.52593	0.2466	1.2231	**0.080347**	**0.0037231**	0.074012
	$\frac{R}{D}, \frac{r}{D}$	0.23, 0.0023	0.04, 0.0004	0.2, 0.002	0.06, 0.0006	0.78, 0.4056	0.19, 0.0019	0.18, 0.0018	0.14, 0.0014	0.25, 0.0025	0.18, 0.0522	**0.66, 0.4686**	**1, 0.37**	1, 0.51
Inverted-parabolic circular (Rx outside)	LSE	0.0080128	6.2716	0.017466	0.19749	0.031985	0.028218	0.0364	0.32988	0.14859	1.2118	0.21977	0.035098	0.12044
	$\frac{R}{D}$	0.31	0.05	0.25	0.07	1	0.23	0.22	0.17	0.3	0.24	1	1	1
Conical circular (Rx outside)	LSE	0.0061122	4.4233	0.010303	0.17439	0.032259	0.023144	0.028878	0.25407	0.11267	1.1492	0.23274	0.047145	0.12481
	$\frac{R}{D}$	0.33	0.05	0.27	0.08	1	0.25	0.23	0.18	0.33	0.25	1	1	1
Conical circular (Rx inside)	LSE	0.21752	65.717	0.45047	2.5717	0.023636	0.28307	0.31534	2.3385	0.76586	3.426	0.17252	0.0065201	0.079593
	$\frac{R}{D}$	1.0101	1.0101	1.0101	1.0101	1.6129	1.0101	1.0101	1.0101	1.0101	1.0101	2	1.8182	2
Uniform elliptical (Rx outside)	LSE	0.0054104	**1.6483**	0.0069964	**0.12699**	0.027536	**0.020099**	**0.01438**	**0.084363**	**0.043075**	0.99888	0.17236	0.0088632	0.096185
	$\frac{b}{a}, \frac{a}{D}$	0.27, 0.81	**0.03, 0.99**	0.21, 0.81	**0.05, 0.96**	0.98, 0.99	**0.17, 0.99**	**0.16, 0.99**	**0.11, 0.99**	**0.2, 0.99**	0.14, 0.99	0.99, 0.99	0.99, 0.99	0.99, 0.99
Uniform elliptical (Rx inside)	LSE	0.0098299	39.696	0.032237	1.1525	0.021374	0.027642	0.01824	0.19629	**0.040088**	0.99239	0.17649	0.0095826	0.078971
	$\frac{L}{D}$	1.0204	1.0101	1.0101	1.0101	1.3514	1.0101	1.0101	1.0101	**1.0204**	1.0101	1.7857	1.6393	1.5873
Gaussian	LSE	**0.0041719**	3.2328	**0.0060807**	0.14807	0.023555	**0.019722**	0.019087	0.19192	0.083137	1.1181	0.17199	0.0071247	0.08039
	$\frac{\sigma}{D}$	**0.14**	0.02	**0.11**	0.03	0.66	**0.1**	0.1	0.07	0.13	0.1	0.85	0.78	0.84
Rayleigh circular (Rx outside)	LSE	**0.0041526**	6.3259	**0.0060807**	0.14178	0.028019	**0.018841**	0.018867	0.18705	0.081898	1.1168	0.20754	0.025242	0.10243
	$\frac{R}{D}$	**0.139**	0.027	**0.11**	0.032	0.5	**0.104**	0.098	0.073	0.134	0.102	0.5	0.5	0.5

2.5 Insights from Calibration

2.5.1 Insights from the Unimodal Empirical Datasets

For the uni-model datasets, the well-fitting models are "Rayleigh circular (Rx outside)", "Gaussian", "uniform elliptical (Rx outside)", and (in only one case) "uniform elliptical (Rx inside)".

In both the "Rayleigh circular (Rx outside)" and the "Gaussian" models, the scatterers become denser as they are closer to the transmitter. Indeed, for whichever empirical dataset well-fit by either the "Gaussian" model or the "Rayleigh circular (Rx outside)" model, the other model is also well-fitting for that data-set. In such well-fitting cases, the calibrated model parameters $\frac{R}{D} \approx \frac{\sigma}{D} \approx 0.10, 0.15$, for both of these geometric models. (Please refer to Table 2.3 for all symbol-definitions in this section.) Moreover, such a range of values for the "Gaussian" model's $\frac{\sigma}{D}$ implies that the receiver is far from most scatterers, even though the "Gaussian" model has a nominally infinite spatial support region for the scatterers.

Table 2.5: Comparing the Arriving Multipaths' Azimuth-Spreads for the Empirical Data-Sets Well-Fit by the "Uniform Elliptical (Rx Outside)" Geometric Model

Reference	Setting	$\frac{b}{a}$	$2\arctan(\frac{b}{a})$
Pedersen [138] Fig. 1	Rural	0.03	3.4°
Takada [168] Fig. 4	Suburban	0.05	5.7°
Fleury [51] Fig. 16	Urban	0.17	19°
Mogensen [119] Fig. 3	Urban	0.16	18°
Pedersen [140] Fig. 4 (Aarhus)	Urban	0.11	13°
Pedersen [140] Fig. 4 (Stockholm)	Urban	0.2	22°

The well-fitting "uniform elliptical (Rx outside)" and the "uniform elliptical (Rx inside)" models have the model-parameter $a/D \in [0.96, 1.02]$, i.e., the receiver is just marginally inside or marginally outside the ellipse. Moreover, it is on the ellipse's longer axis that the receiver lies, showing that the "depth" is more important than the "breadth" (i.e., the azimuth-spread) of the scatterers' spatial distribution between the transmitter and the receiver. Table 2.5 lists the azimuth-spreads of the arriving multipaths for the several empirical datasets that are well-fit by the "uniform elliptical (Rx outside)" geometric model. As the model-parameter of $b/a \ll 1$ in all those cases, the azimuth-spread approximately equals $2\arctan(b/a)$. Table 2.5 shows that the arriving multipaths' azimuth-spread increases as the propagation environment setting moves from "rural" to "suburban" to "urban", fitting the intuitive expectation that the more clustered environment will result in multipaths arriving from a wider azimuth-spread. Note that the "uniform elliptical (Rx outside)" model is the only unimodal geometric model with two degrees of freedom.

The "Rx inside" models are not well-fitting, except for one "urban" case. This conforms to the intuitive expectations that the more urban is the propagation environment setting,

the transmitter needs to be modeled as located more among the scatterers.

Which of the four above-mentioned well-fitting models is best for performance-analysis of a communication system? Recall from Table 2.3 that both the "Gaussian" model and the "Rayleigh circular (Rx outside)" model have open-form expressions for the arriving multipaths' DOA-distribution; however, Gaussianity may ease further mathematical analysis. As these two geometric models are comparable in their calibration-LSE, the "Gaussian" model may be preferred over the "Rayleigh circular (Rx outside)" model. If a closed-form DOA-distribution is required, the choice will be the "uniform elliptical (Rx outside)" geometric model.

2.5.2   Insights from the Bimodal & Higher-Model Empirical Datasets

For the five bimodal and trimodal empirical datasets in Table 2.2, the best-fitting model is either the "uniform pie-cut (Rx inside)" model or the "uniform hollow-disc (Rx outside)" model.[4] Both models have two degrees of freedom.

These two models are in fact the only two geometric models with more than one peak in the DOA-distribution: the "uniform pie-cut (Rx inside)" model is trimodal, whereas the "uniform hollow-disc (Rx outside)" model is bimodal. For the two tetra-modal empirical data-sets, they are both best-fit by the "uniform pie-cut (Rx inside)" geometric model, which alone (among all geometric models) offers three peaks.

Considering the three empirical datasets best-fit by the "uniform pie-cut (Rx inside)" geometric model:

a. Two empirical datasets are "urban", while one is "suburban". This dove-tails with the intuitive expectation that a more clustered propagation-environment would more likely produce a non-unimodal DOA-distribution.

b. All calibrated "uniform pie-cut" models have a beamwidth under $45°$.

c. All calibrated "uniform pie-cut" models have the model-parameter $1 \leq \frac{R}{D} \leq 1.11$, i.e., the receiver is at or very close to the pie-cut rim. This suggests that the scatterers at the receiver's backside are of only marginal importance.

The "Gaussian" model, though best fitting for none of the five non-unimodal datasets in Table 2.2, is at worst only roughly double the lowest LSE. The "Gaussian" model can thus offer modeling simplicity for an LSE still within about one third of an order-of-magnitude of the best fitting model.

2.6   Summmary

For the uni-modal datasets, the well-fitting geometric models are mainly "Rayleigh circular (Rx outside)", "Gaussian", and "uniform elliptical (Rx outside)". The "Gaussian" model

---

[4]The "uniform circular (Rx inside)" model comes in second for the one dataset from Figure 6 of Kloch [83]. There, the receiver at the street level surrounded by two-storey buildings.

may be preferred over the "Rayleigh circular (Rx outside)" model, because Gaussianity may ease further mathematical analysis of a communication system's performance. If a closed-form DOA-distribution is required, the choice will be the "uniform elliptical (Rx outside)" geometric model.

The non-uni-modal empirical datasets are best-fit by the "uniform pie-cut (Rx inside)" geometric model or the "uniform hollow-disc (Rx outside)" geometric model, which have three and two peaks, respectively.

Though no one geometric model is best by all criteria and for all environments, a safe choice is the "Gaussian" model, with a Gaussian density of scatterers centered at the transmitter. Despite this model's simplicity with only one degree of freedom, it is *always* either the best fitting model or offers an LSE within one third of an order-of-magnitude as the best fitting model – The only other model that offers such robust fitting is the "Rayleigh" model with two degrees of freedom.
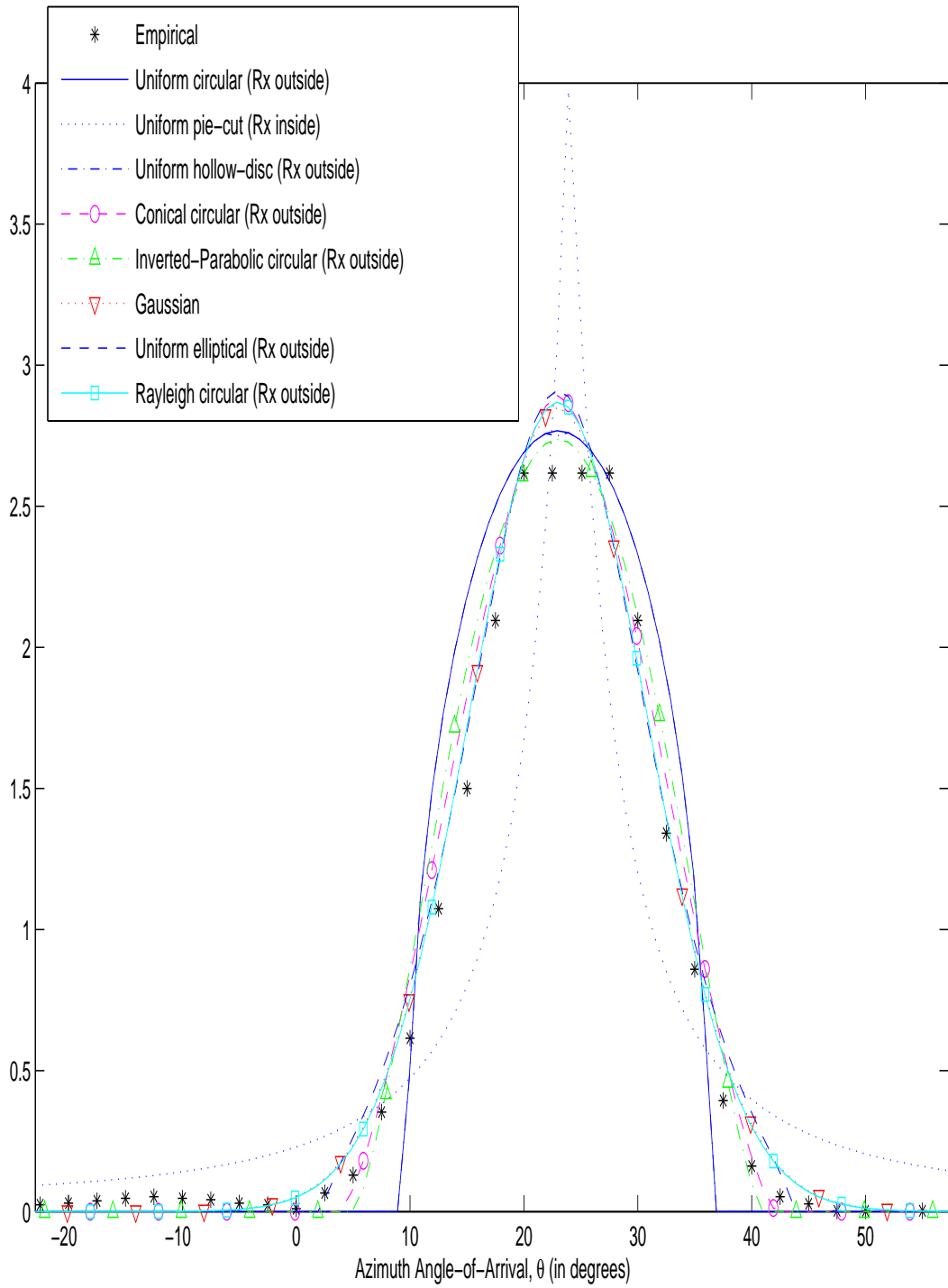
Figure 2.4: Curve-Fitting Various Geometric Model to the Empirical Data in Figure 7 of Matthews [113]
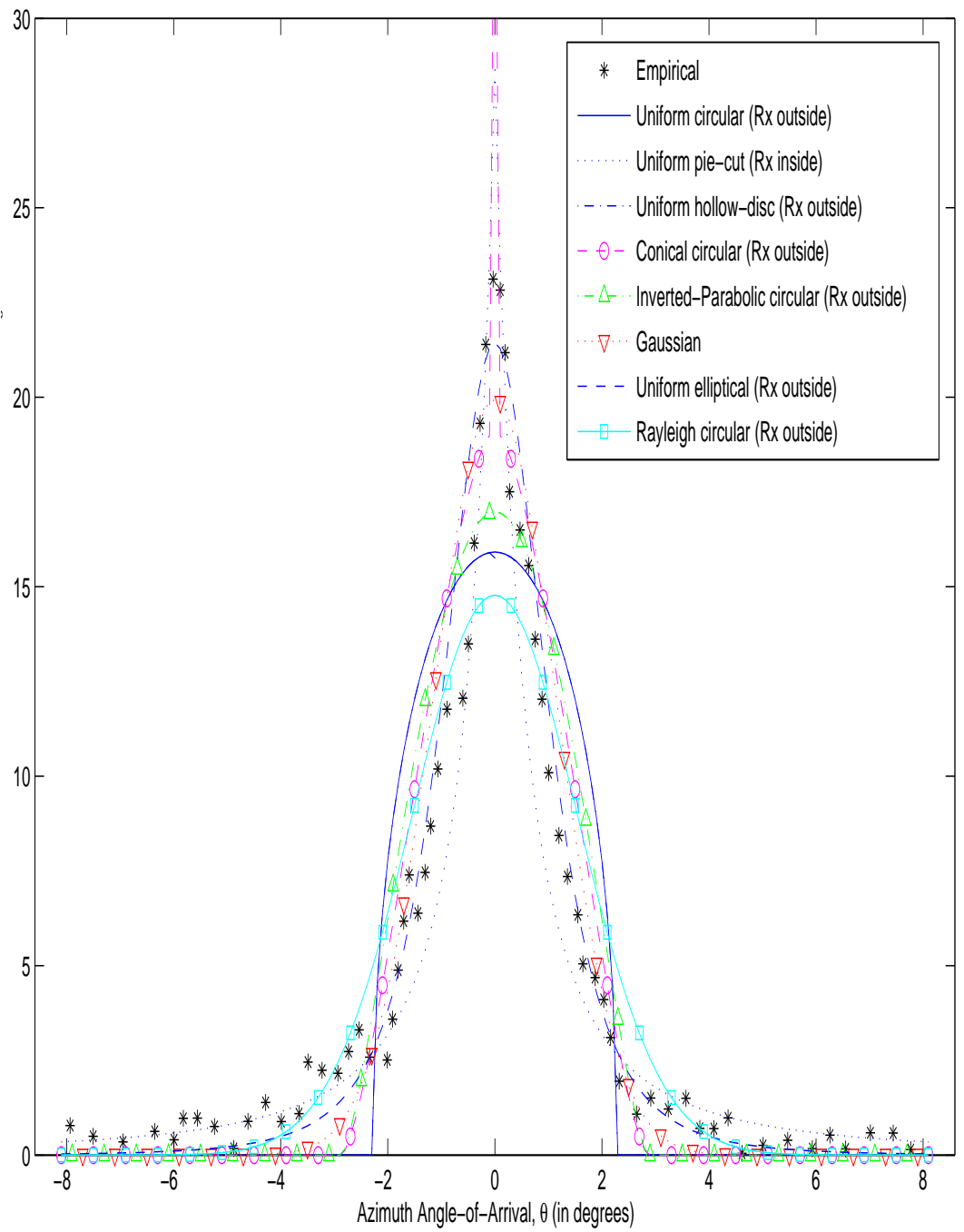
Figure 2.5: Curve-Fitting Various Geometric Model to the Empirical Data in Figure 1 of Pedersen [138]
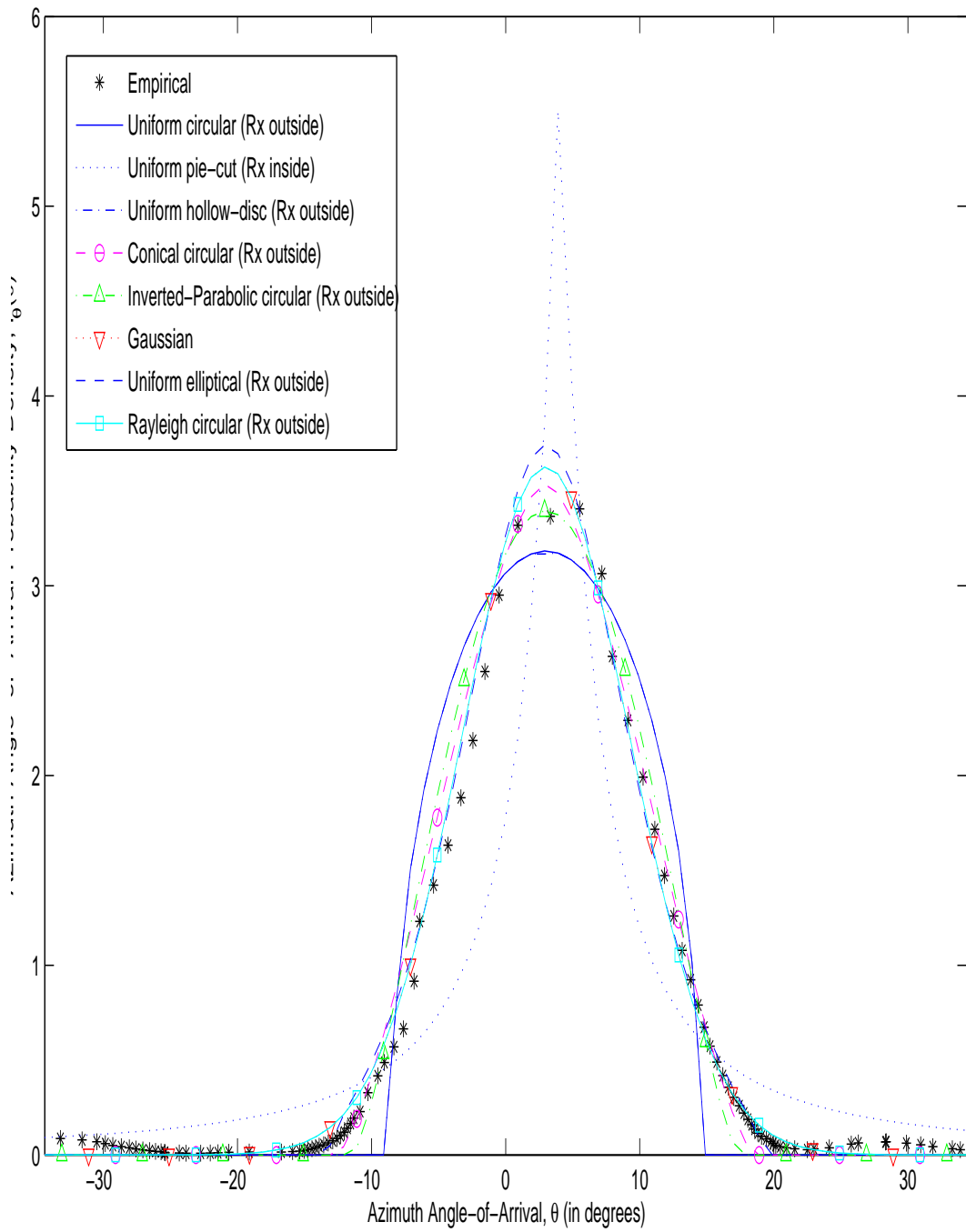
Figure 2.6: Curve-Fitting Various Geometric Model to the Empirical Data in Figure 3 of Kuchar [85]
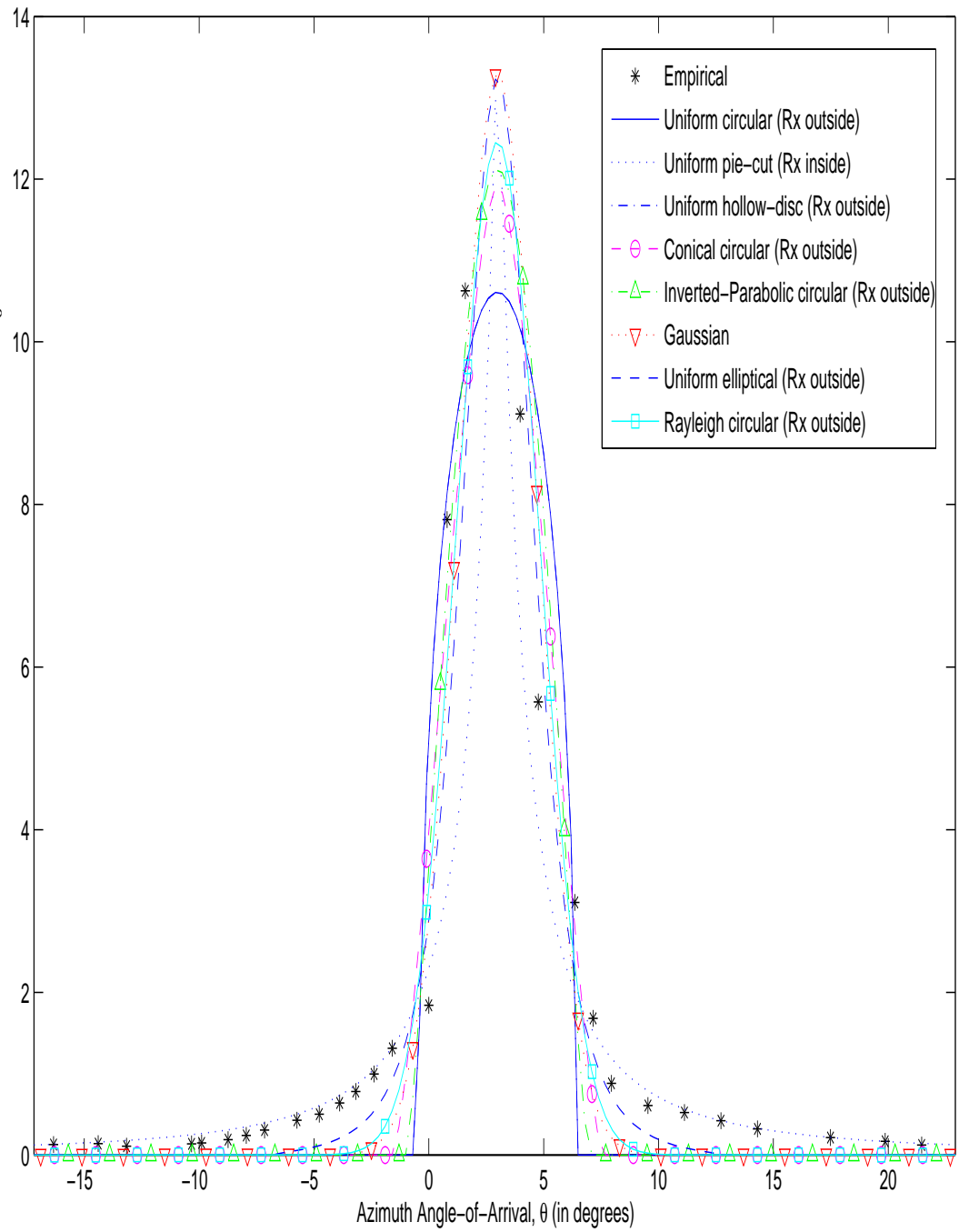
Figure 2.7: Curve-Fitting Various Geometric Model to the Empirical Data in Figure 4 of Takada [168]
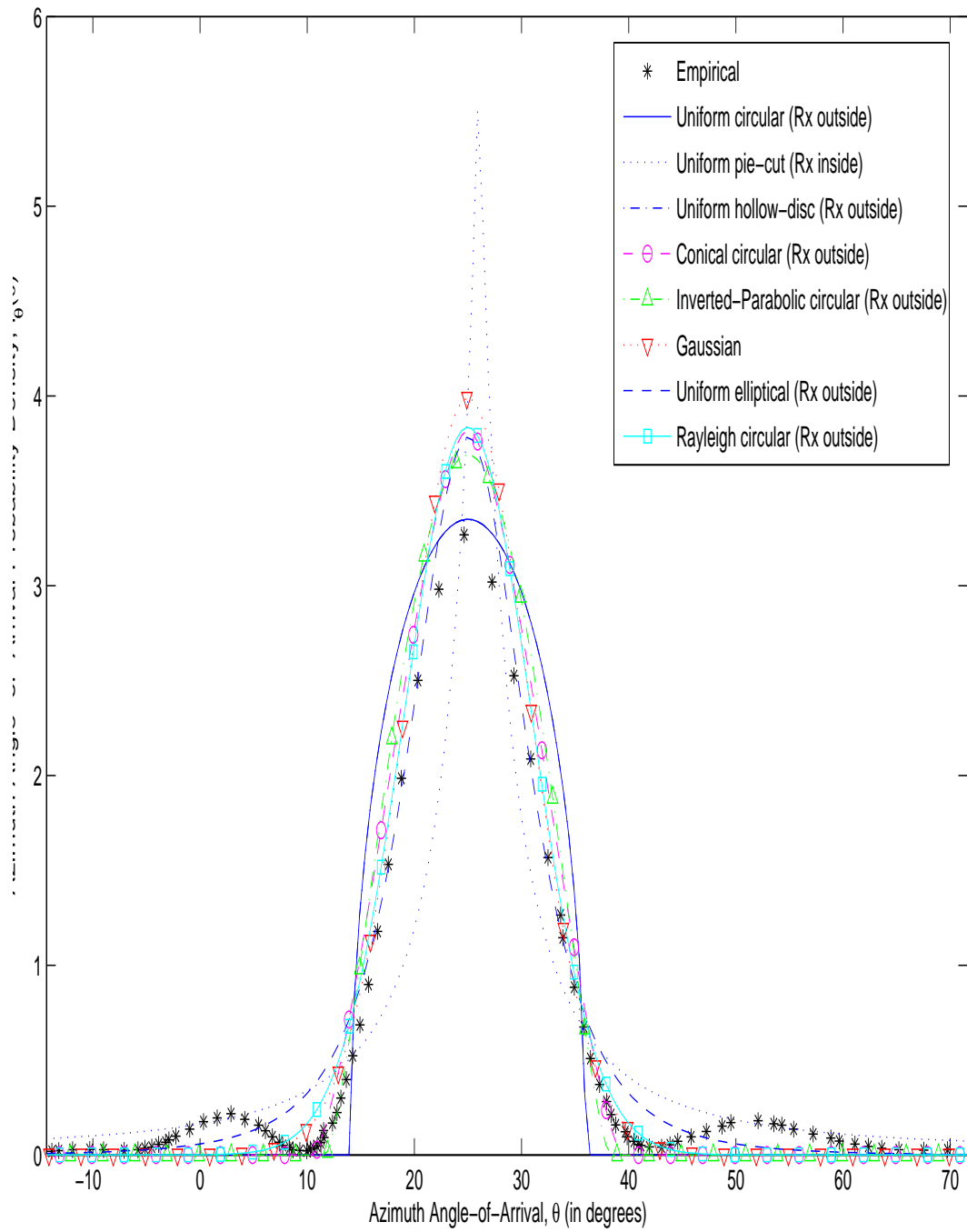
Figure 2.8: Curve-Fitting Various Geometric Model to the Empirical Data in Figure 16 of Fleury [51]
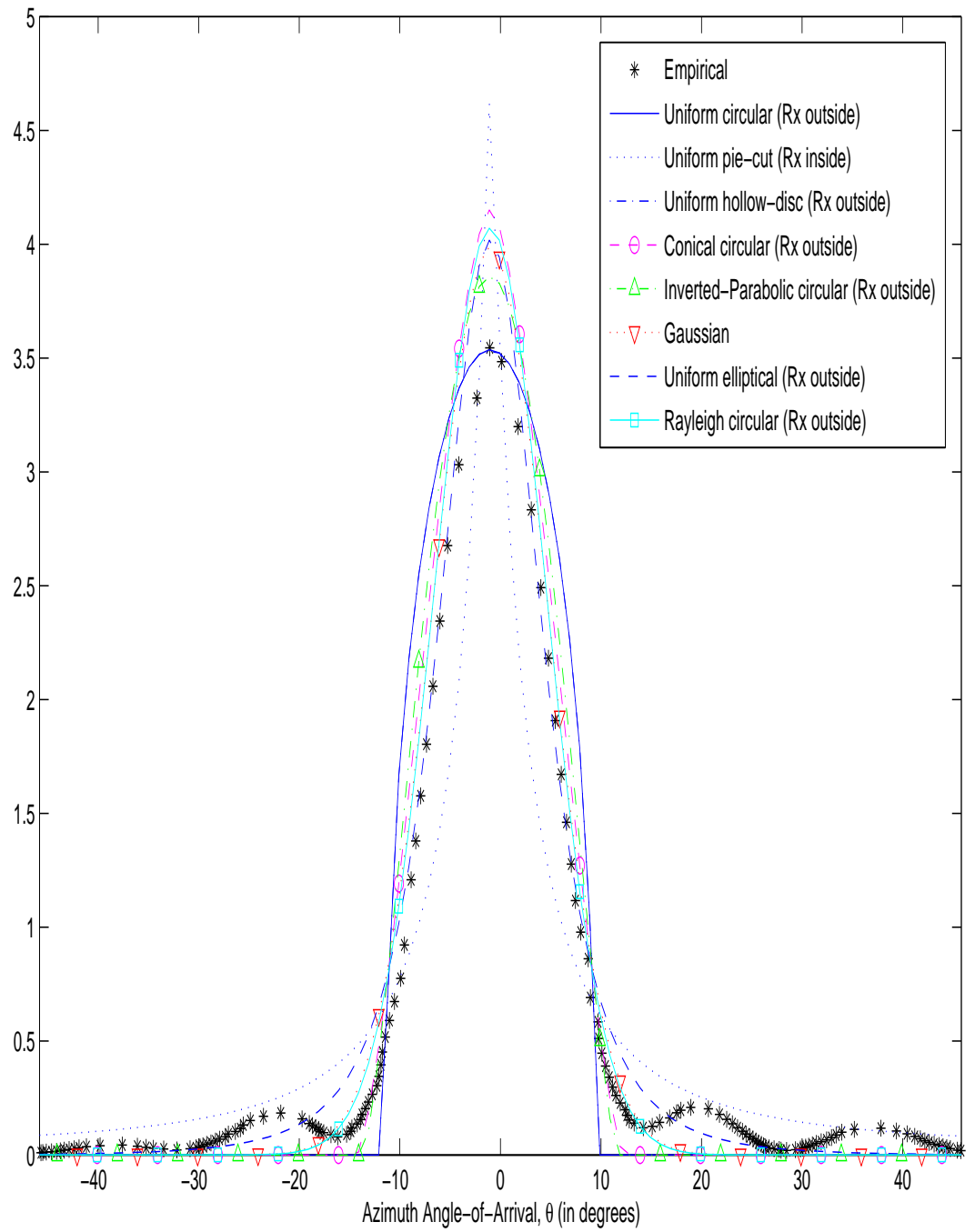
Figure 2.9: Curve-Fitting Various Geometric Model to the Empirical Data in Figure 3 of Mogensen [119]
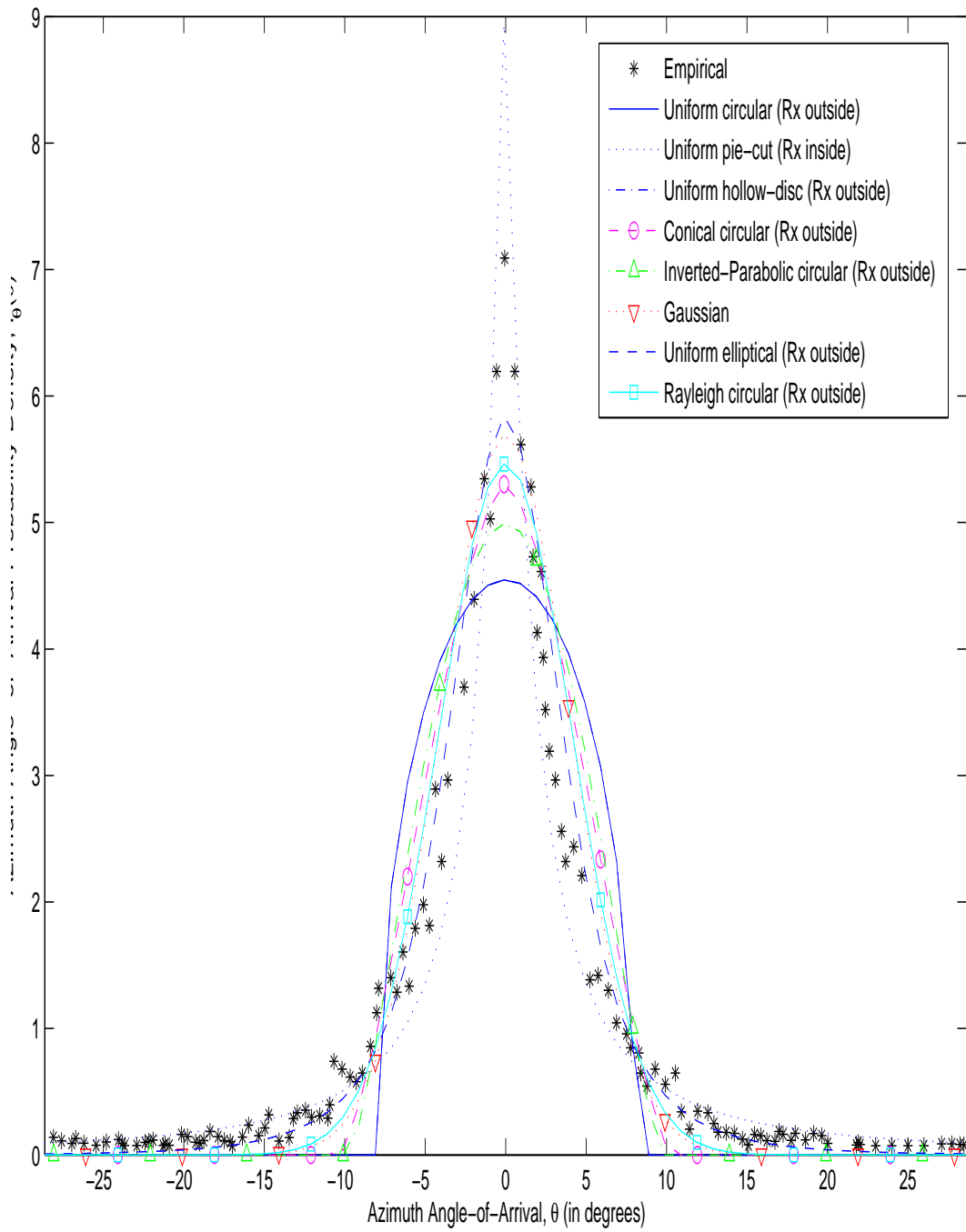
Figure 2.10: Curve-Fitting Various Geometric Model to the Empirical Data in Figure 4 of Pedersen [140] Aarhus
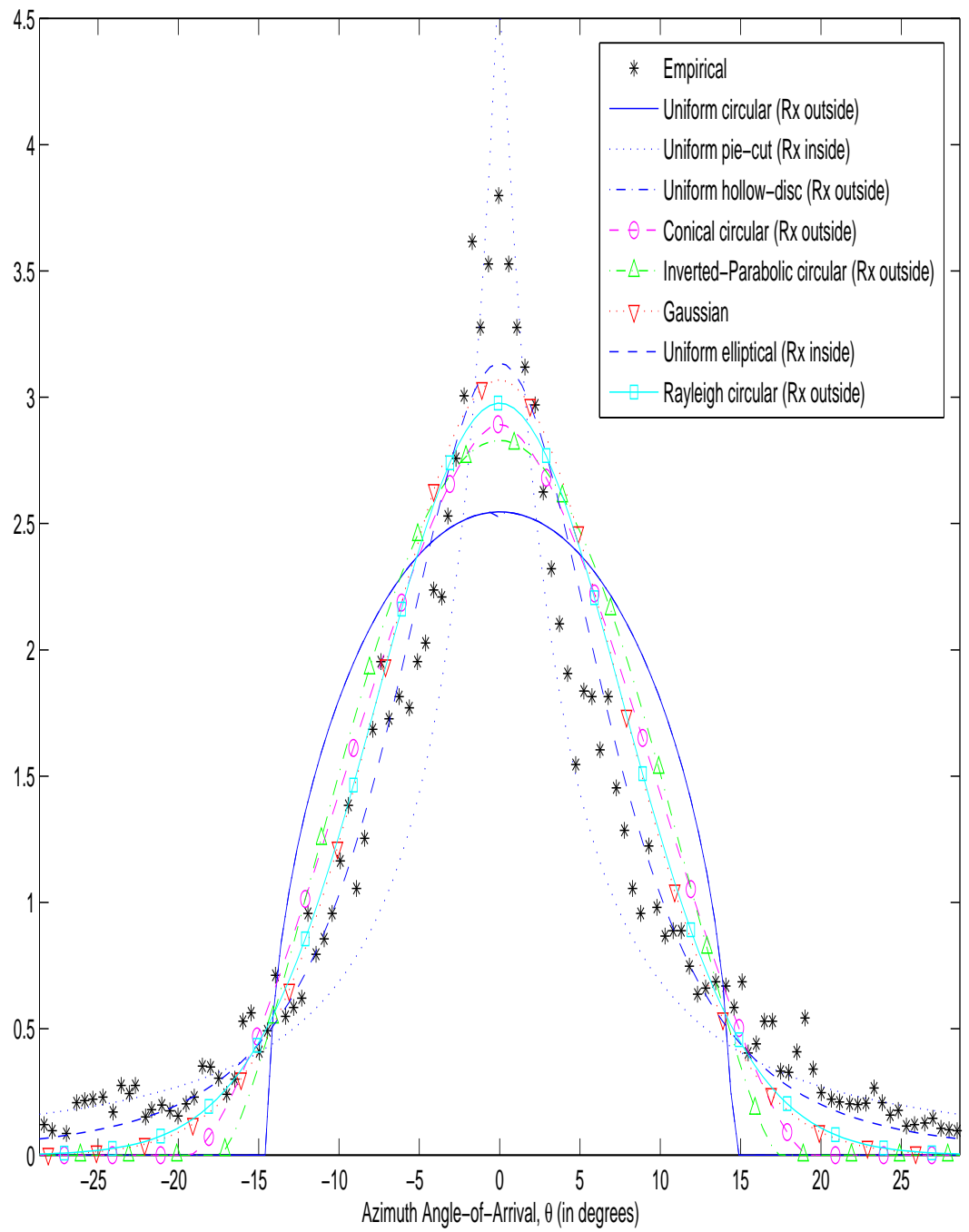
Figure 2.11: Curve-Fitting Various Geometric Model to the Empirical Data in Figure 4 of Pedersen [140] Stockholm
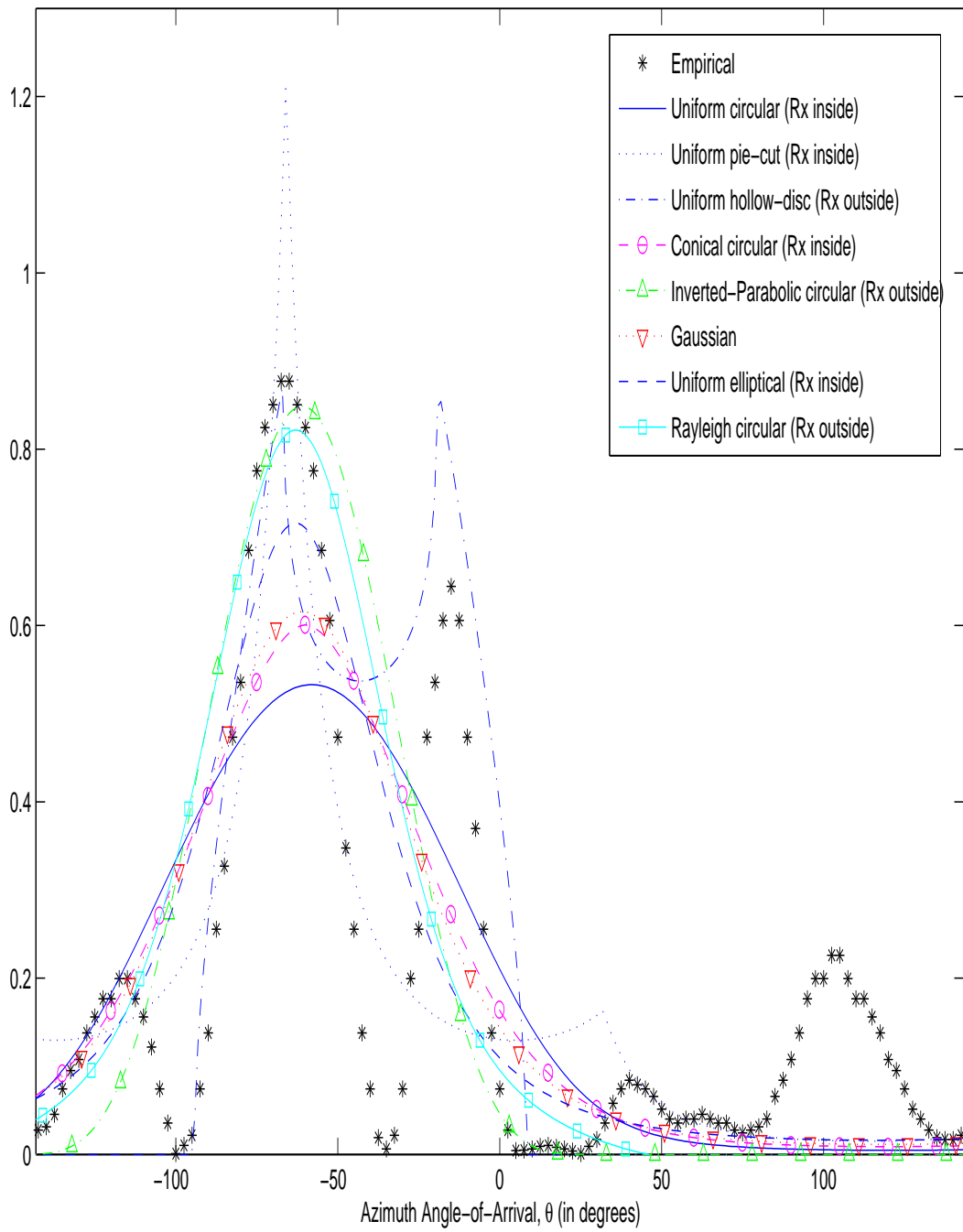
Figure 2.12: Curve-Fitting Various Geometric Model to the Empirical Data in Figure 8 of Matthews [113]
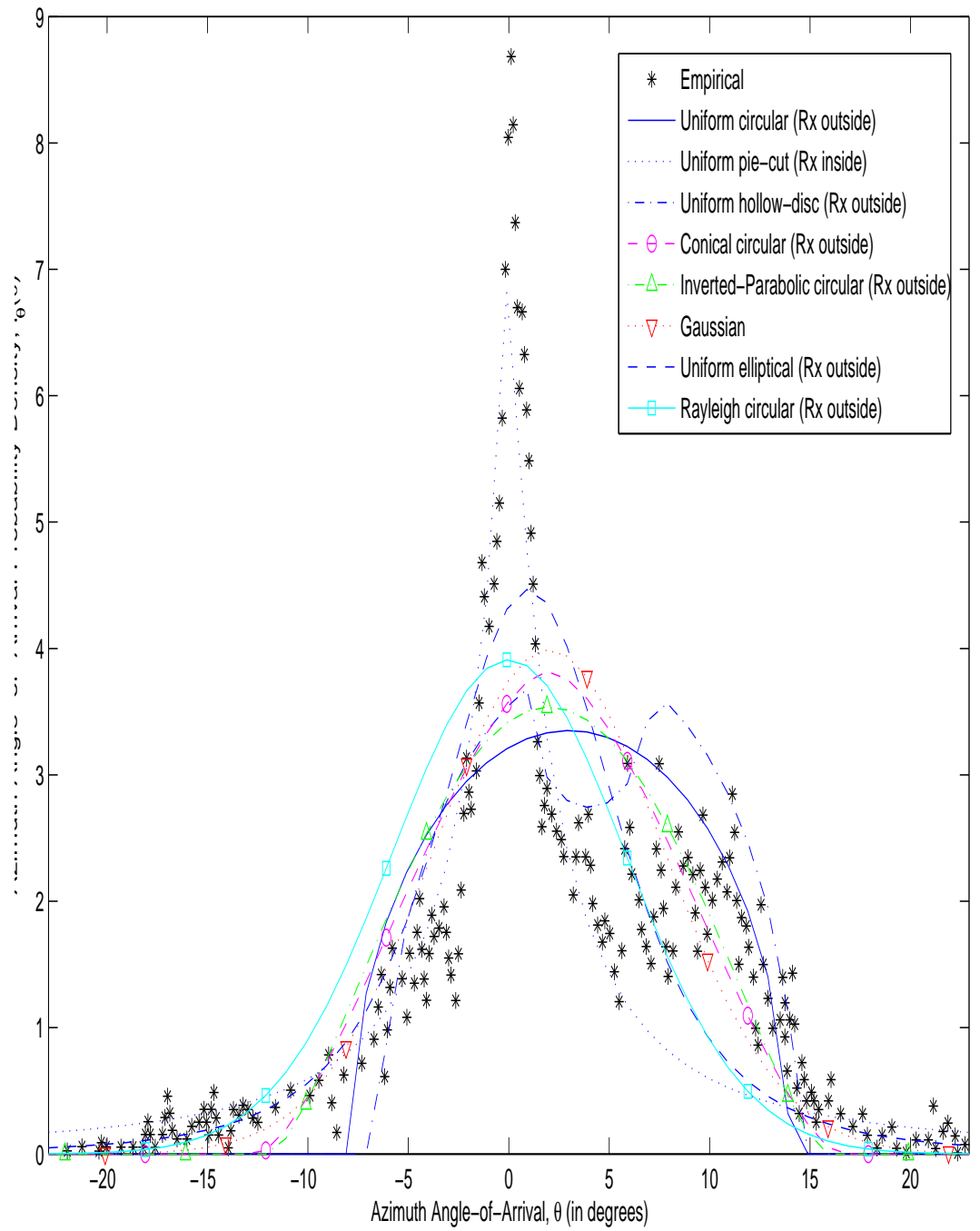
Figure 2.13: Curve-Fitting Various Geometric Model to the Empirical Data in Figure 5 of Pedersen [138]

49
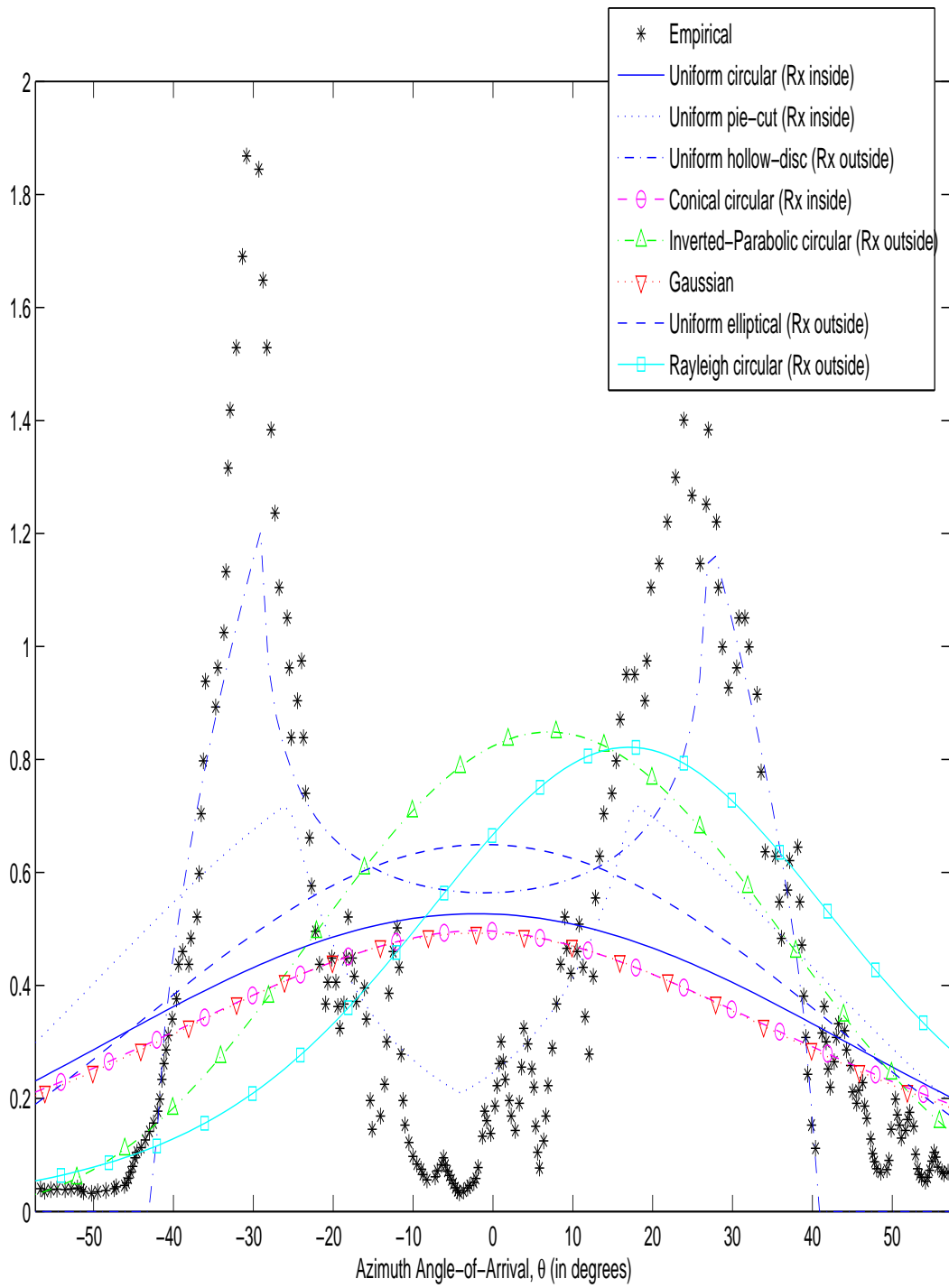
Figure 2.14: Curve-Fitting Various Geometric Model to the Empirical Data in Figure 14 of Pedersen [140]
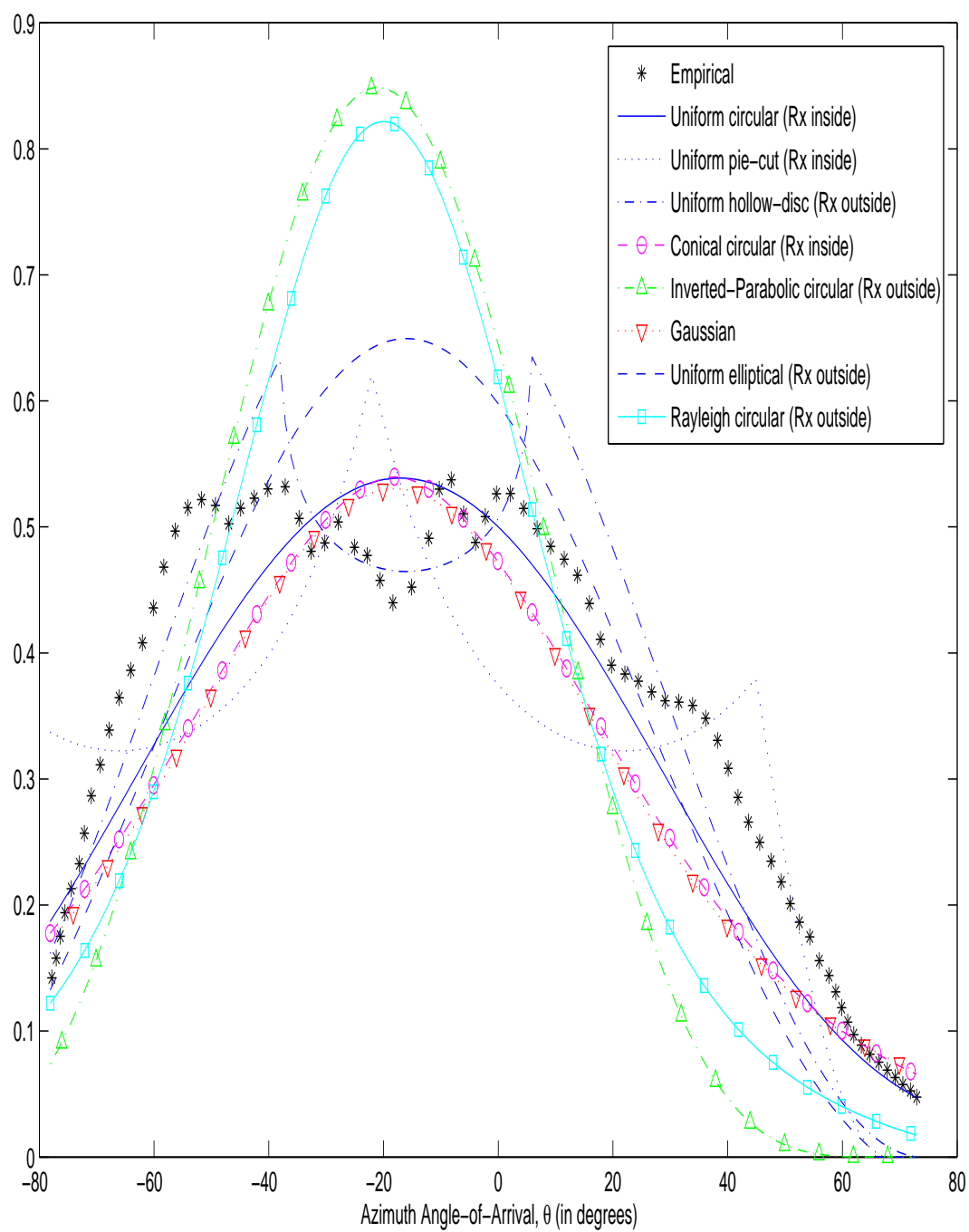
Figure 2.15: Curve-Fitting Various Geometric Model to the Empirical Data in Figure 6 of Kloch [83]
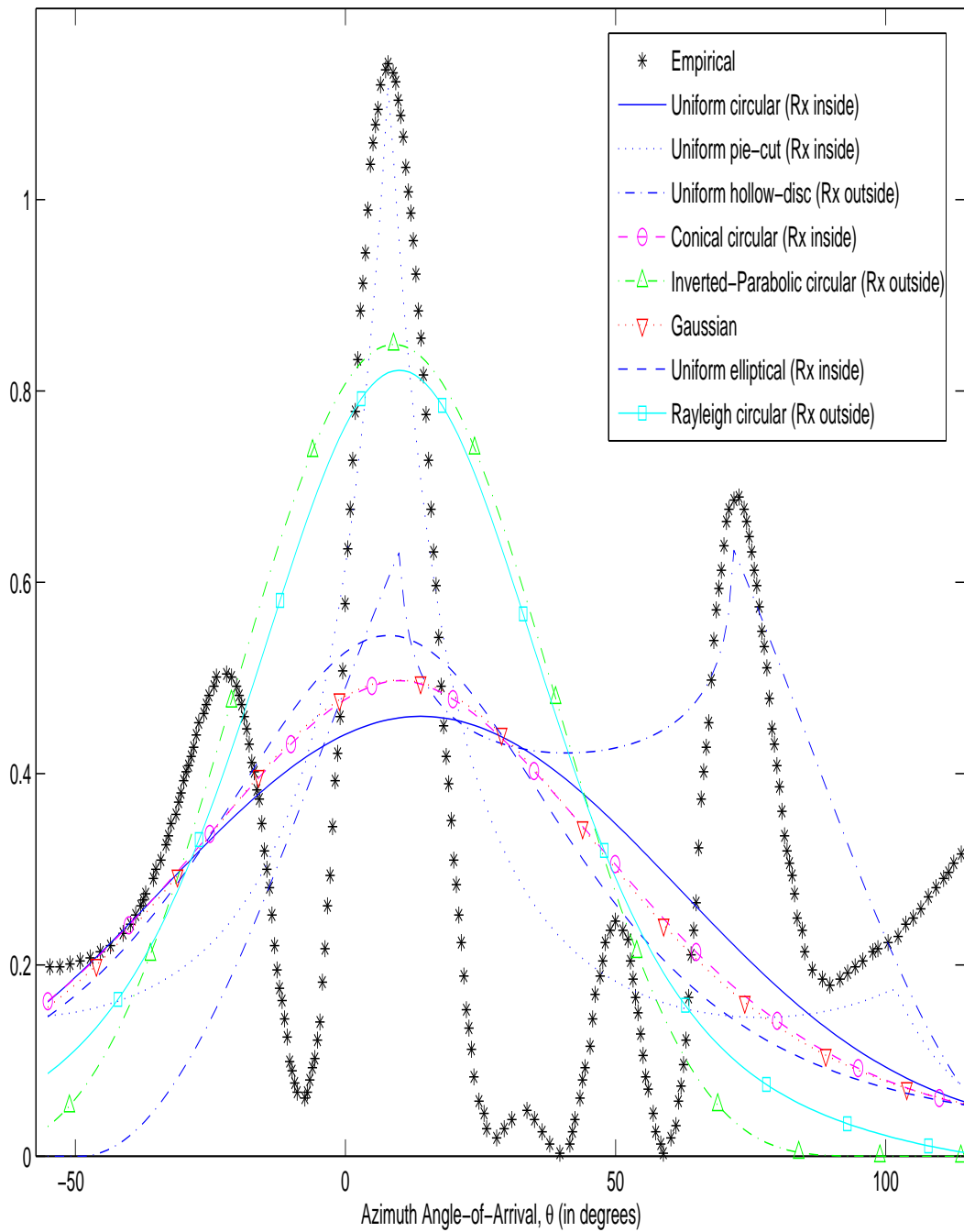
Figure 2.16: Curve-Fitting Various Geometric Model to the Empirical Data in Figure 6 of Eggers [46]

Chapter 3

A Geometric Model for the Uplink/Downlink Multipaths' TOA Distribution, Assuming the Scatterers of a Conical Spatial Density

3.1 Preliminary

3.1.1 The Propagation Delay in Wireless Communications

A signal, transmitted from a mobile user in a landmobile radiowave wireless cellular communication system, arrives at the cellular base-station through multiple propagation multipaths. Each multipath carries its own propagation history of electromagnetic reflections and diffractions and corruption by multiplicative noise — a history reflected in that multipath's amplitude, Doppler, arrival angle, and arrival time delay at the receiving antenna(s). The values of these amplitudes, Doppler frequency shifts, arrival angles and arrival time delays depend on the electromagnetic properties of and the spatial geometry among the mobile transmitter, the scatterers, and the receiving antennas. Each receiving antenna's data measurement sums these individually unobservable multipaths.

A channel's impulse response (IR) may be represented by a linear time-invariant filter $f_\tau(\tau)$, if the channel is (or can be approximated as) temporally stationary. The corresponding spectrum would generally not have a flat magnitude over the frequency coordinate, hence the term "frequency selective". Only in the degenerate case of $f_\tau(\tau)$ being a single impulse, would the channel's spectrum have a flat magnitude-response over all frequencies. That is, spreading along the delay coordinate τ produces (via a Fourier-type transform) frequency distortions. These are to be distinguished from spreading in the frequency coordinate, which corresponds to temporal variability in the channel (i.e., temporal non-stationarity in the channel's impulse response).

For each uplink multipath that travels from the mobile transceiver to the base-station transceiver, there could exist a corresponding downlink multipath traversing the same spatial path but in the opposite direction from the base-station transceiver to the mobile transceiver. Hence, the uplink $f_\tau(\tau)$ equals downlink $f_\tau(\tau)$.

The time-of-arrival (TOA) probability-density function characterizes the wireless propagation channel's temporal delay spread and frequency incoherence, which in turn determine the obtainable temporal diversity and the extent of inter-symbol interference in wireless communication. These constrain the capacity of information that can be communicated between the transmitter and the receiver. Incidentally, many applications (like single-input single-output communication systems) are interested only in the above-mentioned temporal metric but not in any spatial metric.

This TOA-distribution could be measured (or computer-estimated) in site-specific / terrain-specific / building-specific empirical measurements (or ray-shooting and ray-tracing computer simulations). However, such results would be applicable only to the particular propagation setting under investigation and cannot be easily generalized to a wider class of scenarios. A rough model applicable to a wide class of field scenarios could be to the system-development engineer to develop his/her products, which must be usable in a wide class of environments, like "bad urban" city blocks with high-rises as scatterers on all sides, or "rural" settings with few scatterers close by an elevated base-station. Hence, geometric modeling has also been applied to analyze the TOA-distribution.

3.1.2   Survey of Geometric Models to Derive TOA-Distribution

Within the geometric-modeling literature that analytically derives closed-form formulas of the TOA-distribution explicitly in terms of the model-parameters, one simplest and commonest class of geometric models are the "circular disc" models. There, all scatterers are idealized to be spatially distributed only within a circular disc, according to different spatial densities in different geometric models. This circular disc centers upon the mobile transceiver, whereas the base-station transceiver may lie either inside or outside the disc. Within this class of geometric models:

(1) The scatterers are modeled as *uniformly* distributed within the circular disc,

    (1a) with the base-station transceiver lying *out*side the circular disc [48]. This model could apply where an outdoor base-station transceiver is placed on an elevated tower and thus has few scatterers in the base-station's immediate vicinity. Please see Figure 3.1a.

    (1b) with the base-station transceiver lying with*in* the circular disc [70]. This model could apply for "bad urban" or indoor scenarios, where the base-station transceiver is surrounded by scatterers. Please see Figure 3.1b.

(2) The scatterers are modeled as distributed on the circular disc according to an *inverted parabola* shaped density, with the mobile transceiver lying *out*side the circular disc for a base-station transceiver on an elevated tower outdoor and thus

with few scatterers in the receiver's immediate vicinity [134].[1] Please see Figure 3.1a.

2

Unlike the abovementioned uniform-density models in (1a) and (1b), the "conical" spatial density (like the *inverted parabola* shaped density of model (2)) can account for the more frequent reflections off scatterers nearer to the mobile transceiver. Intuitively in the above geometric abstraction, a reflection farther from the mobile transceiver may correspond in physical reality to a sequence of consecutive reflections occurring spatially farther and farther away from mobile, but these reflections incur power loss. The consequence is roughly equivalent to more single-bounce scatterers closer to the mobile transceiver. Rather than modeling the scatterers' re-transmission power as spatially non-stationary, it is mathematically simpler to model scatterers to have identical re-transmission characteristics, but more densely spaced the closer to the mobile transceiver. Instead of assuming lossy scatterers (which would further complicate the present mathematical derivation), the present model has a lower spatial density of scatterers where the physical propagation paths would likely have their "last bounces" (and would have already suffered much reflection power loss) before reaching the base-station transceiver.

The scatterers' conical-distribution geometric model has in fact been first proposed in [45], but only the azimuth *direction*-of-arrival (DOA) distribution was derived only for the *up*link. No TOA-distribution is yet derived in [45]. This paper will fill this literature gap.

3.2 The Presently Advanced "Geometric" Models

Figures 3.1a and 3.1b show the spatial geometries relating the mobile transceiver, a scatterer, and the base-station transceiver. Let the base-station transceiver (BS) be located at the origin of a two-dimensional plane, whereas the mobile transceiver (MS) is located at the Cartesian coordinates $(D, 0)$ with D being the BS-MS distance. Symbolize the aforementioned circular disc's radius as R. The scatterers' spatial locations are idealized

---

[1]The open literature currently has no result for the case of the scatterers distributed on the circular disc according to an *inverted parabola* shaped density, with the mobile transceiver lying *in*side the circular disc.

[2]The above circular-disc support region has been generalized to:

(3) an *hollow circular* disc (on which the scatterers are uniformly distributed) [133],

(4) an *elliptical disc* (on which the scatterers are uniformly distributed)

  (4a) focused at the mobile transceiver and the base-station transceiver [100], [48], [164],

  (4b) centered at the mobile transceiver *alone*, with the base-station transceiver outside of the ellipse [164], [5],

(5) a three-dimensional *hemi − spheroid* region above the mobile transceiver [135].
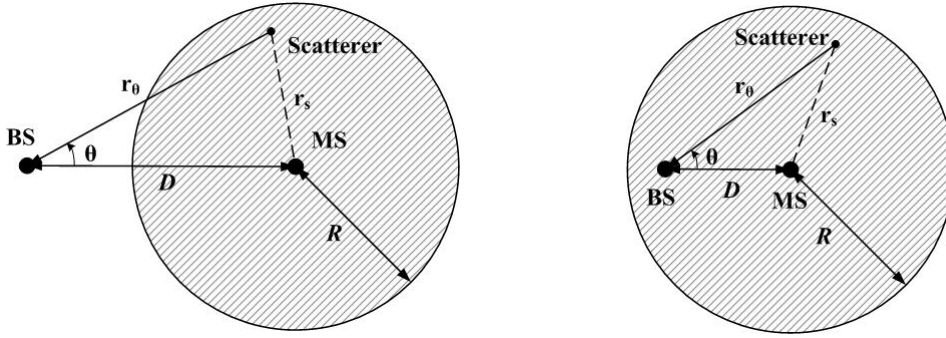
Figure 3.1a: The scatterers' spatial support region in the proposed outdoor model with the base-station (BS) transceiver on an elevated tower and away the dominant scatterers.

Figure 3.1b: The scatterers' spatial support region in the proposed indoor model, with the base-station (BS) transceiver lying *among* the scatterers.

as conically distributed within this circular disc [45],

$$
f_{x,y}(x,y) \;=\; \begin{cases} \left(1 - \frac{\sqrt{(x-D)^2+y^2}}{R}\right)\frac{3}{\pi R^2}, & \text{if } (x-D)^2 + y^2 \le R^2; \\ 0, & \text{otherwise.} \end{cases} \tag{3.1}
$$

Figure 3.2 illustrates this conical spatial density.

For an outdoor base-station on an elevated tower (and thus *away* from any dominant scatterer), the $D \ge R$ case in Figure 3.1a applies. For an indoor or "bad urban" base-station transceiver lying *among* from the scatterers, 3.1b's $D \le R$ case applies.

The propagation time-of-arrival (TOA) equals $\tau = \frac{r_\theta + r_s}{c}$ for a propagation-path from the mobile transmitter, reflecting off a scatterer at (x,y), and arriving at the base-station transceiver, where c denotes the speed of propagation, τ symbolizes the propagation time-of-arrival, θ refers to azimuth-angle of that scatterer as seen by the receiver, $r_s = \sqrt{(x-D)^2 + y^2}$, and r_θ denotes the distance between the base-station transceiver and any scatterer, as shown in Figure 3.1a.

Like all earlier papers that analytically derive closed-form explicit expression of the TOA-distribution based on geometrical models, these following four standard assumptions are made:

(A) Each propagation path, from/to the mobile transceiver to/from the base-station transceiver, reflects off exactly one scatterer.

(B) Each scatterer acts (independently of other scatterers) as an omni-directional lossless re-transmitter.

(C) Negligible complex-phase effects in the receiving-antenna's vector-summation of its arriving multipaths. That is, all arriving multipaths arriving at each receiving-antenna are assumed to be temporally in-phase among themselves.

(D) Polarizational effects may be ignored.
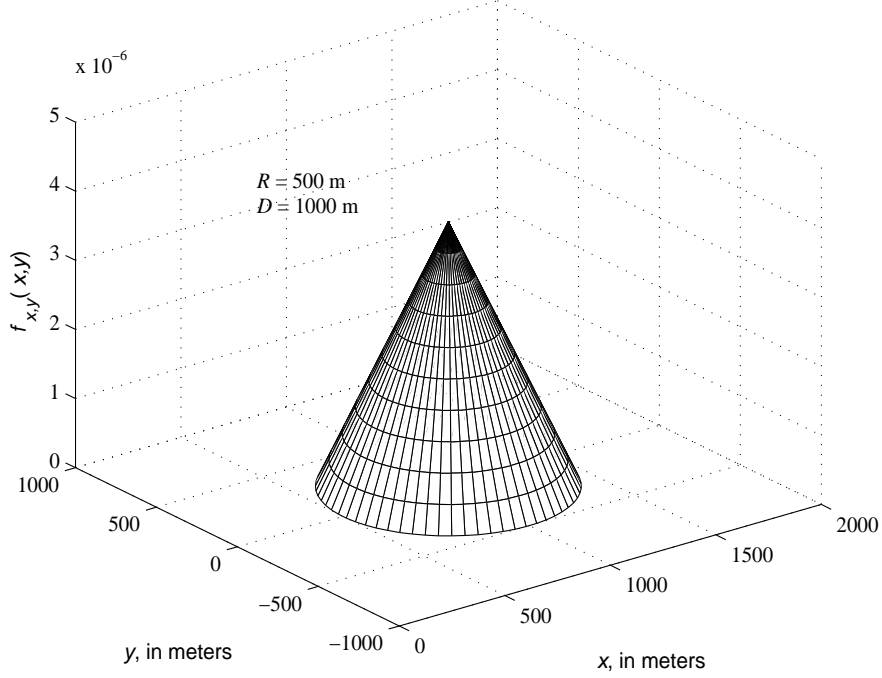
Figure 3.2: Conical spatial density, at $R = 500$ meters and $D = 1000$ meters.

3.3   The Conical Model's TOA-DOA Joint Distribution

Towards deriving the time-of-arrival's distribution density $f_\tau(\tau)$, first express the above spatial density's circular-disc support region in terms of the polar coordinates (r_θ, θ), giving: [134]

$$(r_\theta \cos \theta - D)^2 + (r_\theta \sin \theta)^2 \leq R^2. \tag{3.2}$$

Applying the cosine law to the geometries in Figures 3.1a and 3.1b, [48], [134]

$$r_\theta(\theta) = \frac{D^2 - \tau^2 c^2}{2(D \cos \theta - \tau c)}, \tag{3.3}$$

Next, transform the bivariate spatial density into a bivariate density of the azimuth direction-of-arrival (DOA) and the time-of-arrival (TOA). This is achieved through a Jacobian transformation. For where the constraint in (3.2) is satisfied, [45], [48]:

$$
\begin{aligned}
f_{\tau,\theta}(\tau,\theta) &= |J_1| f_{r_\theta,\theta}(r_\theta,\theta) \\
&= |J_1||J_2| f_{x,y}(x,y)|_{x=r_\theta \cos \theta, y=r_\theta \sin \theta}
\end{aligned}
$$

where

$$J_1 = \left| \frac{\partial r_\theta}{\partial \tau} \right| = \frac{c \left[\left(\frac{\tau c}{D} \right)^2 - 2 \frac{\tau c}{D} \cos \theta + 1 \right]}{2 \left(\cos \theta - \frac{\tau c}{D} \right)^2} \tag{3.4}$$

$$J_2 = \begin{vmatrix} \frac{\partial x}{\partial r_\theta} & \frac{\partial x}{\partial \theta} \\ \frac{\partial y}{\partial r_\theta} & \frac{\partial y}{\partial \theta} \end{vmatrix} = \frac{D \left[1 - \left(\frac{\tau c}{D} \right)^2 \right]}{2 \left(\cos \theta - \frac{\tau c}{D} \right)} \tag{3.5}$$

57

Hence,

$$
\begin{aligned}
f_{\tau,\theta}(\tau,\theta) &= \underbrace{\frac{Dc\left[1-\left(\frac{\tau c}{D}\right)^2\right]\left[\left(\frac{\tau c}{D}\right)^2 - 2\frac{\tau c}{D}\cos\theta + 1\right]}{4\left(\cos\theta - \frac{\tau c}{D}\right)^3}}_{=|J_1||J_2|} \underbrace{\left(1 - \frac{\sqrt{(r_\theta\cos\theta - D)^2 + (r_\theta\sin\theta)^2}}{R}\right)\frac{3}{\pi R^2}}_{=f_{x,y}(r_\theta\cos\theta,\, r_\theta\sin\theta)} \\
&= \frac{3c}{4\pi R}\frac{\left[1-\left(\frac{\tau c}{D}\right)^2\right]\left[\left(\frac{\tau c}{D}\right)^2 - 2\frac{\tau c}{D}\cos\theta + 1\right]}{\frac{R}{D}\left(\cos\theta - \frac{\tau c}{D}\right)^3}\left[1 - \frac{\left(\frac{\tau c}{D}\right)^2 - 2\frac{\tau c}{D}\cos\theta + 1}{2\frac{R}{D}\left(\frac{\tau c}{D} - \cos\theta\right)}\right]. \qquad (3.6)
\end{aligned}
$$

Where the constraint in (3.2) is violated, $f_{\tau,\theta}(\tau,\theta) = 0$.

The TOA-distribution may then be obtained by integrating $f_{\tau,\theta}(\tau,\theta)$ with respect to θ, as will be done in the next section.[3]

3.4 The Outdoor "Conical" Model's TOA-Distribution

In outdoor propagation environments where a base-station transceiver is housed on an elevated tower, few scatterers would surround the mobile transceiver. The scatterers may thus be modeled to cluster only around the mobile transceiver. This corresponds to the $R \geq D$ case in Figure 3.1a.

For any specific $\tau \in \left[\frac{D}{c}, \frac{D+2R}{c}\right]$, there exists a τ-constant spatial ellipse focusing at the base-station's and the mobile's spatial locations. Any propagation path must bounce off a scatterer lying on this ellipse's rim. This elliptical rim intersects with the circle (within which the scatterers lie) on at most two points, namely at $r_\theta(\theta_0) = \tau c - R$ in Figure 3.1a, where $\theta_0 = \arccos\left(\frac{\left(\frac{\tau c}{D}\right)^2 + 1 - 2\frac{\tau c}{D}\frac{R}{D}}{2\left(\frac{\tau c}{D} - \frac{R}{D}\right)}\right)$. These considerations lead to an integration-range of $\theta \in [-\theta_0, \theta_0]$.

Hence, the TOA's marginal density equals:

$$
\begin{aligned}
f_\tau^{(\text{Con,Out})}(\tau) &= \int_{-\theta_0}^{\theta_0} f_{\tau,\theta}(\tau,\theta)\, d\theta \\
&= \frac{3Dc\left[1-\left(\frac{\tau c}{D}\right)^2\right]}{2\pi R^2}\int_0^{\theta_0} \frac{\left[\left(\frac{\tau c}{D}\right)^2 - 2\frac{\tau c}{D}\cos\theta + 1\right]}{\left(\cos\theta - \frac{\tau c}{D}\right)^3}\left[1 - \frac{\left(\frac{\tau c}{D}\right)^2 - 2\frac{\tau c}{D}\cos\theta + 1}{2\frac{R}{D}\left(\frac{\tau c}{D} - \cos\theta\right)}\right] d\theta \\
&= \frac{3Dc\left[1-\left(\frac{\tau c}{D}\right)^2\right]}{\pi R^2}\int_0^{x_0} \frac{\left[\left(\frac{\tau c}{D}\right)^2 - 2\frac{\tau c}{D}\frac{1-x^2}{1+x^2} + 1\right]}{(1+x^2)\left(\frac{1-x^2}{1+x^2} - \frac{\tau c}{D}\right)^3}\left[1 - \frac{\left(\frac{\tau c}{D}\right)^2 - 2\frac{\tau c}{D}\frac{1-x^2}{1+x^2} + 1}{2\frac{R}{D}\left(\frac{\tau c}{D} - \frac{1-x^2}{1+x^2}\right)}\right] dx
\end{aligned}
$$

where the last equality above has used the following transformations [134]: $x = \tan\frac{\theta}{2}$, $\cos\theta = \frac{1-x^2}{1+x^2}$, $d\theta = \frac{2dx}{x^2+1}$, and $x_0 = \sqrt{\frac{\left(\frac{R}{D}\right)^2 - \left(1 - \frac{\tau c}{D} + \frac{R}{D}\right)^2}{\left(1 + \frac{\tau c}{D} - \frac{R}{D}\right)^2 - \left(\frac{R}{D}\right)^2}}$. Mathematica's symbolic integration produces a closed form of $f_\tau^{(\text{Con,Out})}(\tau)$ that explicitly depends on the model parameters of R and D as follows:

$$
f_\tau^{(\text{Con,Out})}(\tau) = \frac{c}{8\pi R}\frac{\left[h(\delta - 2\varepsilon + 1)(7\delta^2 - 4\delta\varepsilon + 4\varepsilon^2 - 4) - 6(2\delta^2 - 1)(\delta - 2\varepsilon)\arctan(h)\right]}{\varepsilon^2\sqrt{\delta^2 - 1}}
$$

---

[3] The TOA must satisfy $\tau \in \left[\frac{D}{c}, \frac{D+2R}{c}\right]$. This is because no propagation path can traverse the MS-BS distance D under $\frac{D}{c}$ of propagation delay. On the other hand, the latest arriving propagation path must have bounced off a scatterer on the circle's circumference at a direction diametrically opposite the BS-to-MS direction.
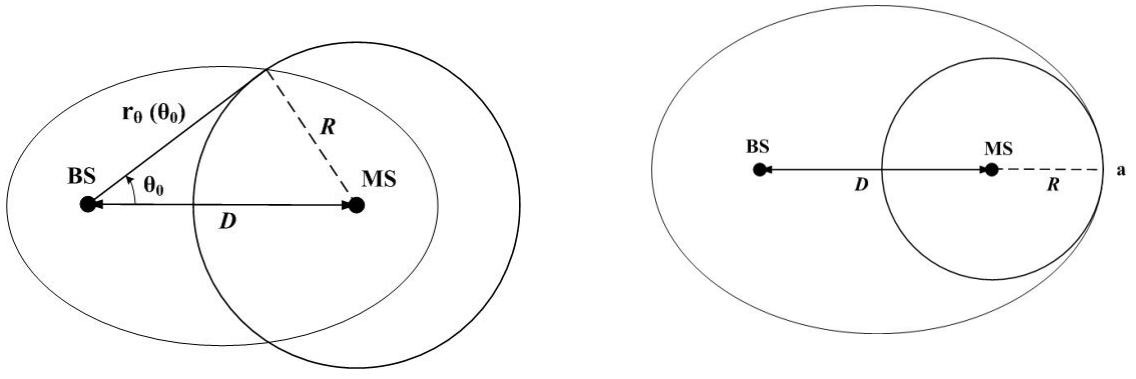
Figure 3.3a: This figure helps to obtain the appropriate integration range of θ. This result is used towards deriving $f_\tau^{(\text{Con,Out})}(\tau)$.

Figure 3.3b: To show that the τ-constant ellipse can intersect with the circle at only two or fewer points. This fact is used towards deriving $f_\tau^{(\text{Con,Out})}(\tau)$.

where $\delta = \frac{\tau c}{D}$, $\varepsilon = \frac{R}{D}$, and $h = \sqrt{\frac{1-\delta+2\varepsilon}{1+\delta-2\varepsilon}}$.

The τ-constant ellipse can intersect the circle at not more than two points, as shown in Figure 3.3a and 3.3b. Otherwise, R would exceed the distance from the mobile to certain points on the elliptical rim — thereby contradicting the fact that the shortest distance from the mobile to the elliptical rim is via point a in Figure 3.3b.

For $\forall \tau > \frac{D+2R}{c}$, $f_\tau^{(\text{Con,Out})}(\tau) = 0$.

To summarize, the "conical" model (for outdoor environments with an elevated base-station) has a TOA-density equal to:

$$f_\tau^{(\text{Con,Out})}(\tau) = \begin{cases} \frac{c}{8\pi R} \frac{\left[h(\delta-2\varepsilon+1)(7\delta^2-4\delta\varepsilon+4\varepsilon^2-4)-6(2\delta^2-1)(\delta-2\varepsilon)\arctan(h)\right]}{\varepsilon^2\sqrt{\delta^2-1}}, & \tau \in \left[\frac{D}{c}, \frac{D+2R}{c}\right] \\ 0, & \text{Otherwise} \end{cases} \quad (3.7)$$

where δ, ε, h have been previously defined. Note that $f_\tau^{(\text{Con,Out})}(\tau)$ peaks at $\tau = \tau_0^{(\text{Con,Out})} = \frac{D}{c}$. By reciprocity between the base-station and the mobile for the propagation delay, the above derived formula applies for the uplink as well as the downlink.

3.5 The Indoor "Conical" Model's TOA-Distribution

In indoor or "bad urban" environments, scatterers may be omni-present, even in the base-station's immediate vicinity. This corresponds to the $R \geq D$ case in Figure 3.1b, where the base-station lies *among* the circular disc of scatterers.

For this indoor or "bad urban" model, the τ-constant ellipse intersects with the circle (within which the scatterers lie) under three disjoint cases:

For $\forall \tau \in \left[\frac{D}{c}, \frac{2R-D}{c}\right)$, the τ-constant ellipse lies wholly within the circular disc. Hence, to obtain the TOA marginal density, $f_{\tau,\theta}(\tau,\theta)$ in (3.6) is to be integrated over $\theta \in [-\pi, \pi)$.

Mathematica's symbolic integration gives:

$$
\begin{aligned}
f_\tau^{(\text{Con,In})}(\tau) &= \int_{-\pi}^{\pi} f_{\tau,\theta}(\tau,\theta)\,d\theta \\
&= \frac{3Dc\left[1-\left(\frac{\tau c}{D}\right)^2\right]}{2\pi R^2} \int_0^\pi \frac{\left[\left(\frac{\tau c}{D}\right)^2 - 2\frac{\tau c}{D}\cos\theta + 1\right]}{\left(\cos\theta - \frac{\tau c}{D}\right)^3}\left[1 - \frac{\left(\frac{\tau c}{D}\right)^2 - 2\frac{\tau c}{D}\cos\theta + 1}{2\frac{R}{D}\left(\frac{\tau c}{D} - \cos\theta\right)}\right]d\theta \\
&= \frac{3D^2c}{8R^3}\frac{\left[2\left(\frac{\tau c}{D}\right)^2 - 1\right]\left(2\frac{R}{D} - \frac{\tau c}{D}\right)}{\sqrt{\left(\frac{\tau c}{D}\right)^2 - 1}} \\
&= \frac{3c}{8R}\frac{(2\delta^2 - 1)(2\varepsilon - \delta)}{\varepsilon^2\sqrt{\delta^2 - 1}}
\end{aligned}
$$

For $\forall\tau \in \left[\frac{2R-D}{c}, \frac{2R+D}{c}\right]$, the τ-constant ellipse intersects with the circle at exactly two points, just as in the preceding section. Here, the θ-integration range equals $[-\theta_0, \theta_0]$. Mathematica's symbolic integration gives:

$$
\begin{aligned}
f_\tau^{(\text{Con,In})}(\tau) &= \int_{-\theta_0}^{\theta_0} f_{\tau,\theta}(\tau,\theta)\,d\theta \\
&= \frac{3Dc\left[1-\left(\frac{\tau c}{D}\right)^2\right]}{2\pi R^2} \int_0^{\theta_0} \frac{\left(\frac{\tau c}{D}\right)^2 - 2\frac{\tau c}{D}\cos\theta + 1}{\left(\cos\theta - \frac{\tau c}{D}\right)^3}\left[1 - \frac{\left(\frac{\tau c}{D}\right)^2 - 2\frac{\tau c}{D}\cos\theta + 1}{2\frac{R}{D}\left(\frac{\tau c}{D} - \cos\theta\right)}\right]d\theta \\
&= \frac{c}{8\pi R}\frac{\left[h(\delta - 2\varepsilon + 1)(7\delta^2 - 4\delta\varepsilon + 4\varepsilon^2 - 4) - 6(2\delta^2 - 1)(\delta - 2\varepsilon)\arctan(h)\right]}{\varepsilon^2\sqrt{\delta^2 - 1}}
\end{aligned}
$$

For all other τ values, $f_\tau^{(\text{Con,In})}(\tau) = 0$.

To summarize, the "conical" indoor model's (or the "conical" "bad urban" model's) TOA-density equals:

$$
f_\tau^{(\text{Con,In})}(\tau) = \begin{cases} \frac{3c}{8R}\frac{(2\delta^2-1)(2\varepsilon-\delta)}{\varepsilon^2\sqrt{\delta^2-1}}, & \tau \in \left[\frac{D}{c}, \frac{2R-D}{c}\right) \\ \frac{c}{8\pi R}\frac{\left[h(\delta-2\varepsilon+1)(7\delta^2-4\delta\varepsilon+4\varepsilon^2-4)-6(2\delta^2-1)(\delta-2\varepsilon)\arctan(h)\right]}{\varepsilon^2\sqrt{\delta^2-1}}, & \tau \in \left[\frac{2R-D}{c}, \frac{D+2R}{c}\right] \\ 0, & \text{Others} \end{cases} \tag{3.8}
$$

To obtain the τ value (to be labeled as $\tau_0^{(\text{Con,In})}$) at which $f_\tau^{(\text{Con,In})}(\tau)$ peaks, obtain solution to the equation $\frac{d\left(f_\tau^{(\text{Con,In})}(\tau)\right)}{d\tau} = 0$, with $\frac{d^2\left(f_\tau^{(\text{Con,In})}(\tau)\right)}{d\tau^2} < 0$. This gives:

$$
\tau_0^{(\text{Con,In})} = \frac{D}{c}\left\{\frac{\varepsilon}{4} + \frac{\sqrt{3Z_2}}{12} + \frac{\sqrt{6}}{12}\left[3\varepsilon^2 + 12 - \sqrt[3]{Z_1} - \frac{18\varepsilon^2 + 21}{\sqrt[3]{Z_1}} + \frac{3\sqrt{3}\varepsilon^3 - 18\sqrt{3}\varepsilon}{\sqrt{Z_2}}\right]^{\frac{1}{2}}\right\} \tag{3.9}
$$

where $Z_1 = 189\varepsilon^2 + 81 + 3\sqrt{-648\varepsilon^6 + 1701\varepsilon^4 + 756\varepsilon^2 - 300}$, and $Z_2 = 3\varepsilon^2 + 12 + 2\sqrt[3]{Z_1} + \frac{36\varepsilon^2+42}{\sqrt[3]{Z_1}}$.

By reciprocity between the base-station and the mobile for the propagation delay, the above derived formulas for $f_\tau^{(\text{Con,In})}(\tau)$ and for $\tau_0^{(\text{Con,In})}$ apply for the uplink as well as the downlink.

3.6 Comparing the "Conical Circular Disc" Models Against Earlier "Circular Disc" Models

The above "conical disc models" are proposed as close variants and alternatives to the customary "circular disc" models (1a), (1b) and (2) in Section 3.1.2 and further elaborated

below:

(1a) The "Uniform Scatterer Density Circular Disc" Model for Outdoor: [48]

For this customary model (with the base-station lying outside the uniform-density scatterer region), the TOA-distribution equals

$$
f_\tau^{(\mathrm{Uni,Out})}(\tau) =
\begin{cases}
\frac{c}{\pi D \varepsilon^2}\left\{\frac{\pi\delta^2 k_2 - \delta k_2^2 + \pi k_2 k_1^2 + \delta k_1^2 - 2\varepsilon k_1^2}{4 k_1 k_2} + \frac{\delta^2 k_0 k_4 + \delta k_0 k_1^2}{2k_4^2 + 2k_0^2 k_1^2}\right. \\
\left. +\frac{\delta^2 + k_1^2}{2k_1}\arctan\left(\frac{k_0 k_1}{k_4}\right) - \frac{\varepsilon - \delta}{\left[4\varepsilon^2 - k_3^2\right]^{1/2}}\left[2\varepsilon^2 + \frac{\delta k_1^2 k_4 (1+k_0^2)}{2k_4^2 + 2k_0^2 k_1^2}\right]\right\}, & \tau \in \left[\frac{D}{c}, \frac{2R+D}{c}\right) \\
0, & \text{Otherwise}
\end{cases}
\tag{3.10}
$$

where $k_0 = \tan\left[\frac{1}{2}\arccos\left(\frac{-\delta^2 + 1 + 2\cdot\varepsilon\delta}{2\varepsilon}\right)\right]$, $k_1 = \sqrt{\delta^2 - 1}$, $k_2 = \sqrt{1 - 4\varepsilon^2 - \delta^2 + 4\varepsilon\delta}$, $k_3 = -\delta^2 + 1 + 2\varepsilon\delta$, $k_4 = 1 - \delta$. Note that $f_\tau^{(\mathrm{Uni,Out})}(\tau)$ peaks at $\tau = \tau_0^{(\mathrm{Uni,Out})} = \frac{D}{c}$.

(1b) The "Uniform Scatterer Density Circular Disc" Model for Indoor: [70]

If the base-station lies inside the uniform-density scatterer region, The TOA-distribution of (1a) becomes:

$$
f_\tau^{(\mathrm{Uni,In})}(\tau) =
\begin{cases}
\frac{c(\delta^2 + S_1^2)}{4D\varepsilon^2 S_1}, & \tau \in \left[\frac{D}{c}, \frac{2R-D}{c}\right) \\
\frac{c}{D}\left[\frac{S_5}{\pi\varepsilon \sin S_0} + \frac{\delta^2 + S_1^2}{4\varepsilon^2 S_1} - \frac{S_6 + S_7}{\pi\varepsilon^2}\right], & \tau \in \left[\frac{2R-D}{c}, \frac{2R+D}{c}\right] \\
0, & \text{Otherwise}
\end{cases}
\tag{3.11}
$$

where $S_0 = \arccos\frac{1 + 2\delta\varepsilon - \delta^2}{2\varepsilon}$, $S_1 = \sqrt{\delta^2 - 1}$, $S_2 = \arctan\left(\sqrt{\frac{\delta+1}{\delta-1}}\tan\frac{S_0}{2}\right)$, $S_3 = \delta - 1 + (\delta+1)\tan^2\frac{S_0}{2}$, $S_4 = \delta - \cos S_0$, $S_5 = \delta - \varepsilon$, $S_6 = \frac{\delta\sin S_0}{2S_4} + \frac{S_1^2 S_5 \cos S_0}{4\varepsilon S_4 \sin S_0} - \frac{\delta S_1^2 \sin S_0}{4\varepsilon S_4^2}$, $S_7 = \frac{\delta}{2S_3}\left[\frac{S_1^2 S_5}{\varepsilon(1+\cos S_0)\sin S_0} - \tan\frac{S_0}{2}\right] + \frac{(\delta^2 + S_1^2)S_2}{2S_1}$.

Note that $f_\tau^{(\mathrm{Uni,In})}(\tau)$ peaks at $\tau = \tau_0^{(\mathrm{Uni,In})} = \frac{2R-D}{c} = \frac{D(2\varepsilon-1)}{c}$. This is because $f_\tau^{(\mathrm{Uni,In})}(\tau)$ monotonously increases for $\tau \in \left[\frac{D}{c}, \frac{2R-D}{c}\right)$ but monotonically decreases in $\tau \in \left[\frac{2R-D}{c}, \frac{2R+D}{c}\right]$.

(2) The "Inverted Parabolic Scatterer Density Circular Disc" Model for Outdoor: [134]

This represents one nonuniform-density alternative to the outdoor model in (1a). Again for a base-station lying outside the circular disc (within which lie the scatters), but according to an inverted-parabola spatial density, the TOA-distribution equals:

$$
f_\tau^{(\mathrm{Inv,Out})}(\tau) =
\begin{cases}
\frac{c}{96 Q_2 \pi D(1-\delta)\varepsilon^4}\left\{48\varepsilon\delta^3 Q_1 Q_2 - 18\delta Q_3 + 23 Q_1 Q_2 \delta\right. \\
-28\varepsilon\delta Q_1 Q_2 + 192\varepsilon^2\delta^2 Q_3 + 23\delta^2 Q_1 Q_2 + 48\delta^5 Q_3 \\
-36\varepsilon^2 Q_1 Q_2 - 128\varepsilon^3\delta Q_1 Q_2 - 192\varepsilon^2\delta^3 Q_3 + 96\varepsilon^4 Q_1 Q_2 \\
-28\varepsilon\delta^2 Q_1 Q_2 - 96\varepsilon^2 Q_3 + 18 Q_3 - 38\delta^4 Q_1 Q_2 \\
-48\varepsilon^3 Q_1 Q_2 - 38\delta^3 Q_1 Q_2 + 18 Q_1 Q_2 \varepsilon - 48\delta^4 Q_3 \\
\left. +96\delta\varepsilon^2 Q_3 + 96\varepsilon^2\delta^2 Q_1 Q_2 + 40\varepsilon^2\delta Q_1 Q_2\right\} & \tau \in \left[\frac{D}{c}, \frac{2R+D}{c}\right] \\
0 & \text{Others}
\end{cases}
\tag{3.12}
$$

where $Q_0 = \delta + 1$, $Q_1 = \left\{\frac{-1 + 2\delta - 2\varepsilon - \delta^2 + 2\delta\varepsilon}{1 + 2\delta - 2\varepsilon + \delta^2 - 2\delta\varepsilon}\right\}^{1/2}$, $Q_2 = \sqrt{(\delta-1)(\delta+1)}$, and $Q_3 = \arctan(Q_0 Q_1 / Q_2)$.

Common to the model-formulas of (3.7), (3.8), (3.10), (3.11) and (3.12) is the model-variable $\varepsilon = \frac{R}{D}$ which controls the shape of the model-geometry. Also common to these equations is the model-variable D which scales the spatial size of the entire model-geometry. Figures 3.4a through 3.5b compare all five TOA-distributions, illustrating the followings:

(i) The support range of τ increases as $\frac{R}{D}$ increases for all five models.

(ii) For each $\frac{R}{D}$ value, $f_\tau^{(\cdot,\mathrm{Out})}(\tau)$ peaks at the initial value of $\frac{\tau_{\mathrm{re}}c}{D} = 0$ and monotonically decreases towards zero as $\frac{\tau c}{D}$ increases. That is, the first arriving non-line-of-sight (NLOS) propagation-path is always the strongest propagation-path. Moreover, more abrupt is the drop to zero for $f_\tau^{(\mathrm{Uni},\mathrm{Out})}(\tau)$ than for $f_\tau^{(\mathrm{Con},\mathrm{Out})}(\tau)$.

(iii) For each $\frac{R}{D}$ value, no $f_\tau^{(\cdot,\mathrm{In})}(\tau)$ is any longer monotonic. That is, the first arriving non-line-of-sight propagation-path is no longer always the strongest propagation-path. Moreover, for any particular $\varepsilon = \frac{R}{D}$, it is always true that $\tau_0^{(\mathrm{Con},\mathrm{In})} < \tau_0^{(\mathrm{Uni},\mathrm{In})}$.

Figure 3.6a shows that the proposed (Con, Out) model (i.e., the base-station lies outside the circular disc, wherein the scatterers follow a conical spatial density) better fits certain empirical data [12] taken in urban Chicago than can the customary (Uni, Out) and (Inv, Out) models. The abovementioned field-measurements involved an elevated base-station atop a building and was 160 feet on average above the surrounding terrain. The mobile receiver was in a vehicle and 2.7 meters aboveground. The channel-sounding signal was 20 MHz in bandwidth and centered around 3.676 GHz. The model-calibration, by the present authors, is via minimization of the mean squared error (MSE) between the "normalized"[4] empirical dataset of arrival-delay distribution $\{(\tau_i, y_i), i = 1, \ldots, I\}$ and the corresponding values $\{(\tau_i, f^X(\tau_i - \tau_1 + \frac{D}{c})), i = 1, \ldots, I\}$ from the geometric model's TOA distribution,

$$\mathrm{MSE} = \frac{1}{I}\sum_{i=1}^{I}\left[y_i - f^{(X)}\left(\tau_i - \tau_1 + \frac{D}{c}\right)\right]^2 \tag{3.13}$$

where $X \in \{(\mathrm{Con, Out}), (\mathrm{Con, In}), (\mathrm{Uni, Out}), (\mathrm{Uni, In})\}$. The best-fitting (Uni, Out) model, at $D = 707$ meters and $R = 169.68$ meters, suffers an MSE of 0.012782. The best-fitting (Inv, Out) model, at $D = 326$ meters and $R = 208.64$ meters, suffers an MSE of 0.010255. In contrast, the best-fitting (Con, Out) model, at $D = 262$ meters and $R = 222.7$ meters, suffers an MSE of only, 0.009325, which is 27% less than that of (Uni, Out) and 9% less than that of (Inv, Out).

Likewise, Figure 3.6b shows that the proposed (Con, In) model better fits certain in-building empirical data [34] than can the customary (Uni, In) model. The channel-sounding signal has a 250 MHz bandwidth, in a seriously clustered environment. The

---

[4]This "normalization" is to ensure a unit-area under the empirical dataset. The normalization proceeds as follows: Let $\tilde{y}_i$ denote the empirical value as presented in [152]; and let $a_{i,i+1}$ denote the area of a trapezoid with its four corners at $(\tau_i, 0), (\tau_i, \tilde{y}_i), (\tau_{i+1}, 0), (\tau_{i+1}, \tilde{y}_{i+1})$. Then the normalized empirical value, at τ_i, is $y_i = \frac{\tilde{y}_i}{\sum_{i=1}^{I-1} a_{i,i+1}}$.

best-fitting (Con, In) model, at $D = 4$ meters and $R = 28$ meters, suffers an MSE of 1.2143, whereas the best-fitting (Uni, In) model, at $D = 10$ meters and $R = 25$ meters, suffers a 57% higher MSE of 1.9039.

3.7   Summary

Presented in this chapter (for indoor or outdoor wireless cellular communications) is an idealized spatial geometry among the base-station transceiver, the scatterers, and the mobile transceiver. These scatterers are spatially confined to a circular disc centered around the mobile transceiver. The scatterers are distributed according to a conical spatial density, in contrast to the customary uniform density. The scatterers are modeled as omni-directional lossless re-transmitters of incoming rays from the transmitter. Analytically derived are closed-form expressions for the uplink/downlink multipaths' time-of-arrival distribution; these expressions are explicitly in terms of the two model-parameters of the idealized geometry. This geometric model is shown to better-fit certain empirical TOA data than the more customary uniform-density or inverted-parabola-density scatterer-geometries.
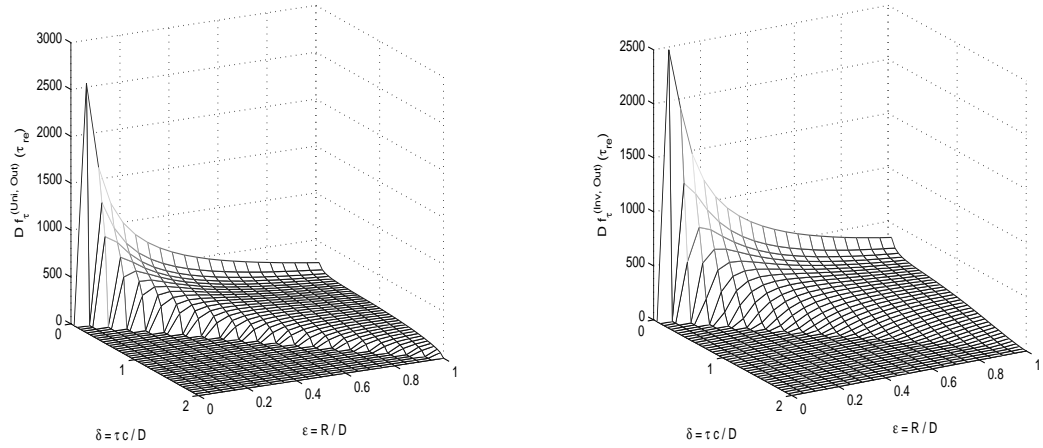
Figure 3.4a: The TOA-distribution of the customary (Uni-Out) "geometric model" of (1a), which has the base-station lying outside the circular disc, wherein the scatterers follow a uniform spatial density.

Figure 3.4b: The TOA-distribution of the customary (Inv-Out) "geometric model" of (2), which has the base-station lying outside the circular disc, wherein the scatterers follow a invert-parabola spatial density.
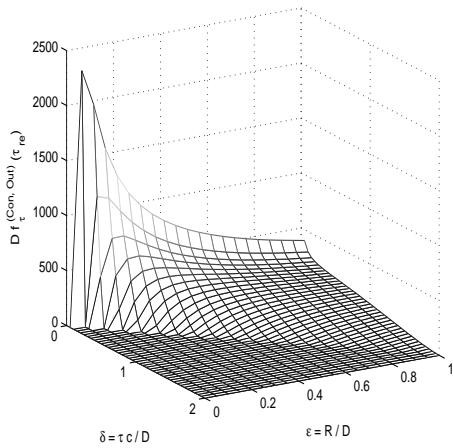
Figure 3.4c: The TOA-distribution of the herein advanced (Con-Out) "geometric model", which has the base-station lying outside the circular disc, wherein the scatterers follow a conical spatial density.
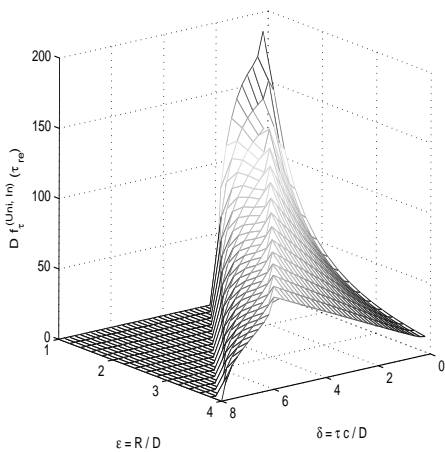
Figure 3.5a: The TOA-distribution of the cus- Figure 3.5b: The TOA-distribution of the tomary (Uni-In) "geometric model" of (1b), herein advanced (Con-In) "geometric model", which has the base-station lying inside the which has the base-station lying inside the circular disc, wherein the scatterers follow a cular disc, wherein the scatterers follow a conuniform spatial density. ical spatial density.
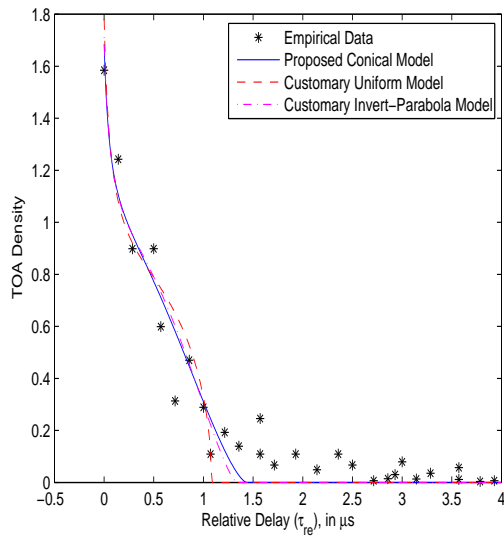
Figure 3.6a: The (Con, Out) model can better fit this empirical dataset than the (Uni, Out) and (Inv, Out) model.
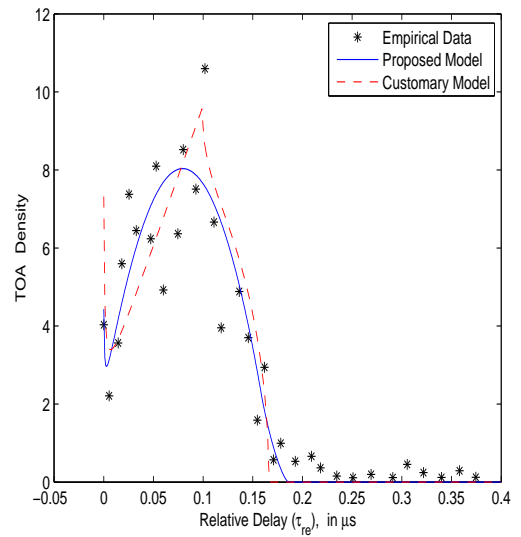
Figure 3.6b: The (Con, In) model can better fit this empirical dataset than the (Uni, In) model.

Chapter 4

The Acoustic Vector-Sensor's Near-Field Array-Manifold

4.1   The Acoustic Vector-Sensor & Particle-Velocity Wave-field

An acoustic **vector**-sensor (a.k.a. vector-hydrophone) consists of three identical, but orthogonally oriented, acoustic velocity-sensors, plus an acoustic pressure-sensor — all spatially co-located in a point-like geometry. Each acoustic ***velocity***-sensor measures one Cartesian component of the incident acoustic particle-field vector. [1]The entire acoustic vector-sensor thus distinctly measures all three Cartesian components of the particle-velocity vector plus the pressure scalar. This contrasts with a customary microphone or hydrophone measuring only the acoustic pressure.

More precisely: for a point-source incident with unit-power from the **far** field [2], an acoustic **vector**-sensor (located at the Cartesian coordinates' origin) has this array manifold, [125], [115]

$$
\mathbf{a}_{\mathrm{far}} \;\overset{\mathrm{def}}{=}\;
\begin{bmatrix}
u(\psi,\phi) \\
v(\psi,\phi) \\
w(\psi) \\
1
\end{bmatrix}
\;\overset{\mathrm{def}}{=}\;
\begin{bmatrix}
\sin\psi\cos\phi \\
\sin\psi\sin\phi \\
\cos\psi \\
1
\end{bmatrix}
\tag{4.1}
$$

where $0 \leq \psi \leq \pi$ symbolizes the elevation-angle measured from the vertical z-axis, $0 \leq \phi < 2\pi$ denotes the azimuth-angle measured from the positive x-axis, $u(\psi, \phi)$ refers to the direction-cosine along the x-axis, $v(\psi, \phi)$ refers to the direction-cosine along the y-axis, and $w(\theta)$ refers to the direction-cosine along the z-axis. Specifically, the first, second, and third components in (4.1) correspond to the acoustic ***velocity***-sensors aligned along

---

[1]Acoustic ***velocity***-sensor technology has been used in underwater-acoustics and air-acoustics [95] for over a century, and is the subject of recently renewed interest [14], [157]. Many different types of acoustic velocity-sensors are available [93], with designs ranging from mechanically-based [71], to thermally based [176], to optically-based [65], to derivative-based [165], [102], [180].

[2]An emitter (with a "characteristic source dimension" L, wavelength λ, and a distance of R from the receiver) lies in the receiver's acoustic far field, if $2\frac{R}{L} \gg \max\{2, \frac{\lambda}{2\pi}\}$ and $2\frac{R}{L^2} \gg \pi/\lambda$.

the x-axis, the y-axis, and the z-axis, respectively. These three Cartesian components of particle-velocity field-vector has a Euclidean norm $\left([u(\psi, \phi)]^2 + [v(\psi, \phi)]^2 + [w(\psi)]^2\right)$ equal to the unity pressure, for all ψ and ϕ.

This acoustic **vector**-sensor concept is practical. It has been implemented in hardware in various forms for underwater or sea-surface applications [41, 42, 129, 39, 163, 160, 116], or for air-acoustic applications [35, 136]. Acoustic vector-sensors are commercially available as the "Uniaxial P-U Probe" from Acoustech.[3] Acoustic vector-sensors have undergone sea trials [41, 42, 153, 154, 43, 23, 155, 44, 39, 156, 66, 211, 148, 31, 13, 54]. Acoustic vector-sensors have undergone in-building room trials or atmospheric trials [102]. Acoustic vector-sensors have been proposed for use for underwater port and waterway security [161] and for underwater wireless communications [105, 190, 1, 202].

The acoustic vector-sensor concept is versatile for direction-finding, due to these properties:

(i) A single acoustic vector-sensor intrinsically possesses a two-dimensional azimuth-elevation directivity, because all three Cartesian components of the acoustic velocity-vector-field are simultaneously measured.

(ii) Multiple incident sources' azimuth-angles and the elevation-angles may be estimated and automatically matched with only one acoustic vector-sensor [190], [101], [172].

Direction-finding algorithms that exploit the acoustic vector-sensor's unique array-manifold have been developed in [23, 125, 63, 165, 187, 188, 58, 156, 189, 190, 191, 210, 50, 172, 55, 110, 25, 60, 26, 106, 56, 27, 205, 118, 33, 211, 196, 6, 7, 123, 199, 181, 200, 206, 201, 88, 147, 62]. DOA-tracking algorithms have been developed for the acoustic vector-sensor in [126], [101], [192].

Though the above **far**-field measurement model in (4.1) was first introduced to the signal-processing literature by [125] over a decade ago, the corresponding **near**-field measurement-model has not been investigated. This overlooked issue is herein investigated. As will be shown in the subsequent sections, the **far**-field measurement model's independence from the signal frequency, the source-sensor distance, and the propagation-medium in (4.1) is invalid for the **near**-field case.

4.2 Derivation of the Acoustic Vector-Sensor's Near-Field No-Boundary Array-Manifold

Consider an acoustic vector-sensor located at the Cartesian origin, with a position-vector $\mathbf{r}_0 = [0, 0, 0]^T$. Let R denote the distance between the acoustic vector-sensor and an emitting source located at

$R \underbrace{[\cos\phi\sin\psi, \sin\phi\sin\psi, \cos\psi]^T}_{=\bar{\mathbf{r}}}$. The source emits a signal into an half-space of infinite radius of quiescent isotropic homogeneous fluid, such as air or water. A pressure-field

---

[3]http://www.acoustechcorporation.com

$p(\mathbf{r}, t)$ (a *scalar* function at spatial location $\mathbf{r}$ and time t) and a corresponding particle-velocity-field vector-field $\mathbf{v}(\mathbf{r}, t)$ (a *vector*-function) will result. To relate $p(\mathbf{r}, t)$ to $\mathbf{v}(\mathbf{r}, t)$, apply Euler's equation:[4]

$$\rho_0 \frac{\partial \mathbf{v}(\mathbf{r}, t)}{\partial t} = -\nabla p(\mathbf{r}, t) \tag{4.2}$$

where ρ_0 refers to the ambient fluid density [5].

To avoid distraction from the present focus on the array-manifold, a simple signal-model will be used: Let the emitted signal be a pure tone of angular frequency ω and complex-amplitude A. This results in a complex-value pressure-field at the acoustic vector-sensor

$$p(\mathbf{r}_0, t) = \frac{A}{|\mathbf{r}_0 - R\,\bar{\mathbf{r}}|} \exp\left\{ j \left[\omega t - \mathbf{k}^T (\mathbf{r}_0 - R\,\bar{\mathbf{r}}) \right] \right\} = \frac{A}{R} \exp\left[j \left(\omega t - \frac{2\pi}{\lambda} R \right) \right] \tag{4.3}$$

where $\mathbf{k} = -\frac{\omega}{c}\bar{\mathbf{r}}$ denotes the incident wavenumber-vector pointing along the propagation-direction and with modulus $\frac{\omega}{c} = \frac{2\pi}{\lambda}$, c symbolizes the propagation-speed, and λ signifies the signal wavelength. Moreover,

$$-\nabla p(\mathbf{r}_0, t) = -\frac{\partial p(\mathbf{r}_0, t)}{\partial R} \bar{\mathbf{r}}, \tag{4.4}$$

because $p(\mathbf{r}_0, t)$ depends on R, but not ϕ or ψ. Likewise, the particle-velocity vector $\mathbf{v}(\mathbf{r}_0, t)$ may be represented as $|\mathbf{v}(\mathbf{r}_0, t)|\bar{\mathbf{r}}\, e^{j\omega t}$ at spatial location $\mathbf{r}_0$ and time t, where $|\cdot|$ refers to the Euclidean norm of the vector inside the pair of vertical lines. Hence,

$$\frac{\partial \mathbf{v}(\mathbf{r}_0, t)}{\partial t} = j\omega \mathbf{v}(\mathbf{r}_0, t) \tag{4.5}$$

Combining the above equations,

$$
\begin{aligned}
\mathbf{v}(\mathbf{r}_0, t) &= -\frac{1}{j\omega\rho_0} \frac{\partial}{\partial R} \left[\frac{A}{R} \exp\left\{ j \left(\omega t - \frac{2\pi}{\lambda} R \right) \right\} \right] \bar{\mathbf{r}} \\
&= \frac{A}{\rho_0 c R} \left(1 + \frac{\lambda}{j 2\pi R} \right) \exp\left\{ j \left(\omega t - \frac{2\pi}{\lambda} R \right) \right\} \bar{\mathbf{r}} \\
&= \frac{p(\mathbf{r}_0, t)}{\rho_0 c} \left(1 + \frac{\lambda}{j 2\pi R} \right) \bar{\mathbf{r}}
\end{aligned}
\tag{4.6}
$$

[6]

Using the definition of the source's direction-vector $\bar{\mathbf{r}}$, (4.6) becomes:

$$\mathbf{v}(\mathbf{r}_0, t) = p(\mathbf{r}_0, t) \begin{bmatrix} \cos\phi\sin\psi \\ \sin\phi\sin\psi \\ \cos\psi \end{bmatrix} \frac{\sqrt{1 + \left(\frac{\lambda}{2\pi R}\right)^2}}{\rho_0 c} \exp\left(-j \arctan \frac{\lambda}{2\pi R} \right) \tag{4.7}$$

From (4.34), the acoustic vector-sensor **near**-field array-manifold equals:

<hr/>

[4] Please see equation (1-3.7) in [145].

[5] For air-acoustic applications, $\frac{\omega}{2\pi} \in [20, 2 \times 10^4]$ Hz, $c = 343.3$ m/s, the air density $\rho_0 = 1.204$ kg/m^3 at $20°$C, and hence $\rho_0 c \approx 413.3$.

[6] In a far-field case where $R \gg \lambda$, it holds that $\frac{\lambda}{j 2\pi R} \to 0$. Thus, the pressure scalar field would relate to the particle-velocity vector-field as in equation (2) of [59], which presumes a planar wavefront upon the acoustic vector-sensor.

$$\mathbf{a}_{\text{near}} = \begin{bmatrix} \cos\phi\sin\psi \\ \sin\phi\sin\psi \\ \cos\psi \\ \dfrac{\rho_0 c}{\sqrt{1+\left(\frac{\lambda}{2\pi R}\right)^2}} \ \exp\left(j\arctan\frac{\lambda}{2\pi R}\right) \end{bmatrix} \qquad (4.8)$$

A complex-phase difference thus exists between the velocity-sensor triad measurements and the pressure-sensor measurement in the near-field measurement-model in (4.8). This phase-difference depends on the wavelength-normalized source-sensor distance $\frac{R}{\lambda}$ and the propagation-medium's $\rho_0 c$, but not on the azimuth-elevation arriving angles.

As the wavelength-normalized distance $\frac{R}{\lambda} \to \infty$, the near-field array-manifold converges to

$$\begin{bmatrix} \cos\phi\sin\psi \\ \sin\phi\sin\psi \\ \cos\psi \\ \rho_0 c \end{bmatrix}. \qquad (4.9)$$

The above is consistent with the *far*-field array-manifold in equation (2.5) in [125], which normalizes the pressure-sensor gain from $\rho_0 c$ to unity.

4.3 Cramér-Rao Bound Analysis of the Near-Field No-Boundary Measurement Model

4.3.1 Defining the Statistical Data Model

To further characterize the acoustic vector-sensor's array-manifold, this section will derive the Cramér-Rao bound for near-field source-localization by an acoustic vector-sensor. To avoid unnecessary distractions from focusing on the near-field array-manifold, a very simple signal statistical model will be used here: The emitted signal $s(t) = e^{j(\omega t + \epsilon)}$ is a pure tone at angular frequency ω as before, now with an initial phase of ϵ. Both ω and ϵ are deterministic unknown constants. At the m-th time-instant $t = mT_s$, a 4×1 data-vector $\tilde{\mathbf{z}}(mT_s)$ is collected by the four-component acoustic vector-sensor:

$$\tilde{\mathbf{z}}(mT_s) = \mathbf{a}_{\text{near}} s(mT_s) + \tilde{\mathbf{n}}(mT_s) \qquad (4.10)$$

where T_s refers to the time-sampling period and $\tilde{\mathbf{n}}(t)$ denotes a 4×1 vector of additive zero-mean spatio-temporally uncorrelated Gaussian noise with an unknown deterministic variance of σ^2. With M number of time-samples, the collected data-set equals

$$\begin{aligned} \mathbf{z} &= \left[(\tilde{\mathbf{z}}(T_s))^T, \cdots, (\tilde{\mathbf{z}}(MT_s))^T \right]^T \\ &= \underbrace{\mathbf{s} \otimes \mathbf{a}_{\text{near}}}_{=\boldsymbol{\mu}} + \underbrace{\left[(\tilde{\mathbf{n}}(T_s))^T, \cdots, (\tilde{\mathbf{n}}(MT_s))^T \right]^T}_{=\mathbf{n}} \end{aligned} \qquad (4.11)$$

where $\mathbf{s} = e^{j\epsilon} \left[e^{jT_s\omega}, e^{j2T_s\omega}, \cdots, e^{jMT_s\omega} \right]^T$, $\otimes$ symbolizes the Kronecker product, $\mathbf{n}$ represents a $4M \times 1$ noise vector with a spatio-temporal covariance matrix of $\mathbf{\Gamma} = \sigma^2 \mathbf{I}_{4M}$, and $\mathbf{I}_{4M}$ denotes a $4M \times 4M$ identity matrix. Therefore, $\mathbf{z} \sim \mathcal{N}(\boldsymbol{\mu}, \mathbf{\Gamma})$.

The near-field source-localization problem is to estimate the azimuth-elevation arrival-angles ϕ and ψ plus the radial distance R, based on the $4M \times 1$ collected data $\mathbf{z}$.

4.3.2 Deriving the Cramér-Rao Bound for Near-Field Source-Localization by an Acoustic Vector-Sensor

In the statistical data model in Section 4.3.1, there exist six deterministic unknown entities, which are collected into a 6×1 vector $\boldsymbol{\theta} = [\phi, \psi, R, \omega, \epsilon, \sigma^2]^T$. The resulting 6×6 Fisher Information Matrix $\mathbf{J}$ would have its (i, j)th entry equal to[7]

$$
J_{i,j} = 2 \, \Re \left\{ \left(\frac{\partial \boldsymbol{\mu}}{\partial [\boldsymbol{\theta}]_i} \right)^H \mathbf{\Gamma}^{-1} \left(\frac{\partial \boldsymbol{\mu}}{\partial [\boldsymbol{\theta}]_j} \right) \right\} + \mathrm{Tr} \left\{ \mathbf{\Gamma}^{-1} \frac{\partial \mathbf{\Gamma}}{\partial [\boldsymbol{\theta}]_i} \mathbf{\Gamma}^{-1} \frac{\partial \mathbf{\Gamma}}{\partial [\boldsymbol{\theta}]_j} \right\} \tag{4.12}
$$

where $\Re \{\cdot\}$ signifies the real part of the entity inside the curly brackets, $\mathrm{Tr}\{\cdot\}$ denotes the trace operation, and $[\cdot]_i$ symbolizes the ith element of the vector inside the square brackets.

Straightforward calculus manipulations can express the Fisher Information Matrix entries in terms of the measurement-model parameters and statistical data-model parameters

---

[7]Please see equation (8.34) in [178].

as follows:

$$J_{\phi,\phi} = J_{1,1} = \frac{2M}{\sigma^2} \sin^2 \psi, \tag{4.13}$$

$$J_{\psi,\psi} = J_{2,2} = \frac{2M}{\sigma^2}, \tag{4.14}$$

$$J_{R,R} = J_{3,3} = \frac{2M}{\sigma^2} \left[\frac{\rho_0}{\left(\frac{\omega R}{c}\right)^2 + 1} \right]^2 \omega^2, \tag{4.15}$$

$$J_{\omega,\omega} = J_{4,4} = \frac{2M}{\sigma^2} \left\{ \left(R^2 - \frac{\omega^2 R^3}{c} \frac{M+1}{f_s} \right) \left[\frac{\rho_0}{\left(\frac{\omega R}{c}\right)^2 + 1} \right]^2 \right.$$
$$\left. + \frac{(M+1)(2M+1)}{6f_s^2} \left[1 + \omega^2 R^2 \rho_0 \left(\frac{\rho_0}{\left(\frac{\omega R}{c}\right)^2 + 1} \right) \right] \right\}, \tag{4.16}$$

$$J_{\epsilon,\epsilon} = J_{5,5} = \frac{2M}{\sigma^2} \left[1 + \omega^2 R^2 \rho_0 \left(\frac{\rho_0}{\left(\frac{\omega R}{c}\right)^2 + 1} \right) \right], \tag{4.17}$$

$$J_{\sigma^2,\sigma^2} = J_{6,6} = \frac{4M}{\sigma^4}, \tag{4.18}$$

$$J_{R,\omega} = J_{3,4} = J_{4,3} = \frac{2M}{\sigma^2} \left[\frac{\rho_0}{\left(\frac{\omega R}{c}\right)^2 + 1} \right]^2 \left[\omega R - \frac{\omega^3 R^2}{c} \frac{M+1}{2f_s} \right], \tag{4.19}$$

$$J_{R,\epsilon} = J_{3,5} = J_{5,3} = -\frac{2M}{\sigma^2} \left[\frac{\rho_0}{\left(\frac{\omega R}{c}\right)^2 + 1} \right]^2 \frac{\omega^3 R^2}{c}, \tag{4.20}$$

$$J_{\omega,\epsilon} = J_{4,5} = J_{5,4} = \frac{2M}{\sigma^2} \left\{ -\frac{\omega^2 R^3}{c} \left[\frac{\rho_0}{\left(\frac{\omega R}{c}\right)^2 + 1} \right]^2 + \frac{M+1}{2f_s} \left[1 + \omega^2 R^2 \rho_0 \left(\frac{\rho_0}{\left(\frac{\omega R}{c}\right)^2 + 1} \right) \right] \right\}. \tag{4.21}$$

All other entries are zero in the Fisher Information Matrix. As a consequence,

$$\mathbf{J} = \begin{bmatrix} J_{1,1} & 0 & 0 & 0 & 0 & 0 \\ 0 & J_{2,2} & 0 & 0 & 0 & 0 \\ 0 & 0 & J_{3,3} & J_{3,4} & J_{3,5} & 0 \\ 0 & 0 & J_{3,4} & J_{4,4} & J_{4,5} & 0 \\ 0 & 0 & J_{3,5} & J_{4,5} & J_{5,5} & 0 \\ 0 & 0 & 0 & 0 & 0 & J_{6,6} \end{bmatrix} \tag{4.22}$$

is block-diagonal. Hence,

$$\mathrm{CRB}(\phi) = J_{1,1}^{-1} = \frac{\sigma^2}{2M \sin^2 \psi}, \tag{4.23}$$

$$\mathrm{CRB}(\psi) = J_{2,2}^{-1} = \frac{\sigma^2}{2M}, \tag{4.24}$$

$$\mathrm{CRB}(R) = \left[\mathbf{J}^{-1} \right]_{3,3}$$
$$= \frac{J_{4,4} J_{5,5} - J_{4,5}^2}{J_{3,3} J_{4,4} J_{55} + 2J_{3,4} J_{4,5} J_{3,5} - J_{3,3} J_{4,5}^2 - J_{5,5} J_{3,4}^2 - J_{4,4} J_{3,5}^2}, \tag{4.25}$$

where $[\cdot]_{i,j}$ represents the (i,j)-th entry of the matrix inside the square brackets.

Substitution of (4.13) to (4.21) in (4.25) gives

$$\left(\frac{2\pi}{\lambda}\right)^2 \mathrm{CRB}(R) = \frac{\sigma^2}{2M} \frac{\left(\frac{1}{\rho_0 c}\right)^2 \left[\left(\frac{1}{\rho_0 c}\right)^2 + \frac{\left(\frac{2\pi R}{\lambda}\right)^2}{\left(\frac{2\pi R}{\lambda}\right)^2+1}\right]}{\left[\frac{1}{\left(\frac{2\pi R}{\lambda}\right)^2+1}\right]^2 \left[\left(\frac{1}{\rho_0 c}\right)^2 + \frac{\left(\frac{2\pi R}{\lambda}\right)^2}{\left(\frac{2\pi R}{\lambda}\right)^2+1}\right] - \left[\frac{\frac{2\pi R}{\lambda}}{\left(\frac{2\pi R}{\lambda}\right)^2+1}\right]^4} + O(M^{-2})$$

(4.26)

where $O(M^{-2})$ refers to all terms that are multiples of $M^{-2}, M^{-3}, \cdots$. For a sufficiently large M, $O(M^{-2})$ may be ignored.

4.3.3 Qualitative Observations

From (4.23) and (4.24), $\mathrm{CRB}(\phi)$ and $\mathrm{CRB}(\psi)$ are both independent of the signal frequency ω, the source-sensor distance R, the propagation-medium's $\rho_0 c$, and even the source's azimuth-angle ϕ. Moreover, $\mathrm{CRB}(\psi)$ is also unaffected by the source's elevation-angle ψ. The (4.23) and (4.24) here for the **near**-field case are identical to their **far**-field counterparts in equations (51) and (52) of [172].
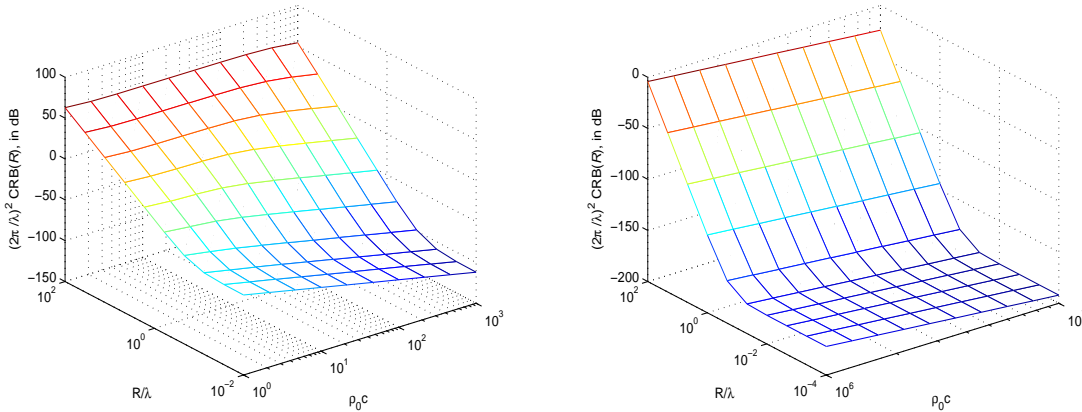
Figure 4.1a: $\left(\frac{2\pi}{\lambda}\right)^2 \mathrm{CRB}(R)$ at 20dB SNR, over ranges of $\rho_0 c$ and $\frac{R}{\lambda}$ most relevant to air-acoustic applications.

Figure 4.1b: $\left(\frac{2\pi}{\lambda}\right)^2 \mathrm{CRB}(R)$ at 20dB SNR, over ranges of $\rho_0 c$ and $\frac{R}{\lambda}$ most relevant to underwater acoustic applications.

In contrast, the wavelength-normalized $\mathrm{CRB}(R)$ of (4.26) is approximately proportional to the effective signal-to-noise ratio $\frac{M}{\sigma^2}$, and depends on the medium's $\rho_0 c$ and on the wavelength-normalized source-sensor distance $\frac{R}{\lambda}$. Furthermore, $\mathrm{CRB}(R)$ is independent of the azimuth-elevation arrival direction.

Figure 4.1a plots $\left(\frac{2\pi}{\lambda}\right)^2 \mathrm{CRB}(R)$ at 20dB SNR, over ranges of $\frac{R}{\lambda}$ and $\rho_0 c$ relevant to *air*-acoustics. Over the support-region shown there, $\left(\frac{2\pi}{\lambda}\right)^2 \mathrm{CRB}(R)$ decreases almost linearly with decreasing $\frac{R}{\lambda}$ but does not vary much with $\rho_0 c$, until the near-field condition of $\frac{R}{\lambda} < \frac{1}{2\pi}$ applies. There in the near field, $\left(\frac{2\pi}{\lambda}\right)^2 \mathrm{CRB}(R)$ becomes largely constant with respect to $\frac{R}{\lambda}$ but decreases with increasing $\rho_0 c$.

Figure 4.1b plots $\left(\frac{2\pi}{\lambda}\right)^2 \mathrm{CRB}(R)$ also at 20dB SNR, over ranges of $\frac{R}{\lambda}$ and $\rho_0 c$ relevant to *underwater* acoustics. [8] Like the air-acoustics case in Figure 4.1a, $\left(\frac{2\pi}{\lambda}\right)^2 \mathrm{CRB}(R)$ decreases

---

[8]Underwater acoustic applications have these typical values: $\frac{\omega}{2\pi} \in [10^{-3}, 10^7]$ Hz, $c = 1481$ m/s, the water density $\rho_0 = 998.2$ kg/m^3 at 20°C, and hence $\rho_0 c \approx 1.48 \times 10^6$.

almost linearly with decreasing $\frac{R}{\lambda}$ outside of the near-field, but becomes largely flat with respect to $\frac{R}{\lambda}$ inside the near field. Moreover, $\left(\frac{2\pi}{\lambda}\right)^2 \mathrm{CRB}(R)$ here decreases very slightly with increasing $\rho_0 c$ whether inside of outside the near field.

4.4 Derivation of the Acoustic Vector-Sensor's Near-Field Near-Boundary Array-Manifold

4.4.1 Extending the Measurement Model from No-Boundary to Near-Boundary

In the last section, the near-field measurement model with acoustic vector-sensor is presented, where model presumes no boundary near the acoustic vector-sensor. When a boundary exists near the acoustic vector-sensor, the measurement model largely changes due to the superposition of reflected wave and the incident wave at the receiver. [59] has investigated the measurement model with a boundary near the acoustic vector sensor, and the model variation brought by different boundary surface (reflection coefficient). However, [59] assumes far-field case where the incident waves are regarded to have plane wave front. On the contrary, in this section, a near-field measurement model is proposed to have a near boundary beside the acoustic vector-sensor

Similarly, as illustrated in Figure 4.2, assume the acoustic vector-sensor is at the origin $\mathbf{r}_0 = [0, 0, 0]^T$, and a reflecting boundary is the plane $z = -d$. $\mathbf{r}_s = [x_s, y_s, z_s]^T$ and $\mathbf{r} = [x, y, z]^T$ are the position vectors of the source and an arbitrary point near the boundary respectively. $\mathbf{r}_{ms} = [x_s, y_s, -z_s - 2d]^T$ denotes the position of the mirror source with respect to the boundary plane.

Consider a wave being emitted form a source in near-field traveling in a quiescent, isotropic, homogeneous, infinite fluid half space, bounded by an infinite planar interface. When the wave hits the boundary, it produces a reflected wave traveling back into the fluid and one or more transmitted waves that continue to propagate past the interface. If the incident wave is monochromatic, the reflected wave is also monochromatic but exhibits a change of amplitude and phase. At position $\mathbf{r}$ and time t, the complex pressure fields in the fluid, due to the incident and reflected waves, are given by

$$p_i(\mathbf{r}, t) \;=\; \frac{A}{|\mathbf{r} - \mathbf{r}_s|} \exp\left\{ j\left[\omega t - \mathbf{k}_i^T(\mathbf{r} - \mathbf{r}_s) \right] \right\} \tag{4.27}$$

$$p_r(\mathbf{r}, t) \;=\; \frac{\Gamma A}{|\mathbf{r} - \mathbf{r}_{ms}|} \exp\left\{ j\left[\omega t - \mathbf{k}_r^T(\mathbf{r} - \mathbf{r}_{ms}) \right] \right\} \tag{4.28}$$

where $\mathbf{r}_s = [x_s, y_s, z_s]^T$ and $\mathbf{r}_{ms} = [x_s, y_s, -z_s - 2d]^T$ denote the positions of the source and the mirror source with respect to the reflecting boundary respectively. A is the complex amplitude of the incident wave at $\mathbf{r}_s$, ω is the angular frequency, and Γ is the complex reflection coefficient, which specifies the attenuation and phase change of the reflected wave. $\mathbf{k}_i$ and $\mathbf{k}_r$ denote the incident and reflected wavenumber vectors at $\mathbf{r}$. Physical considerations require that the normal particle velocities on either side of the boundary are equal, which implies that the incident and reflected waves travel along the boundary
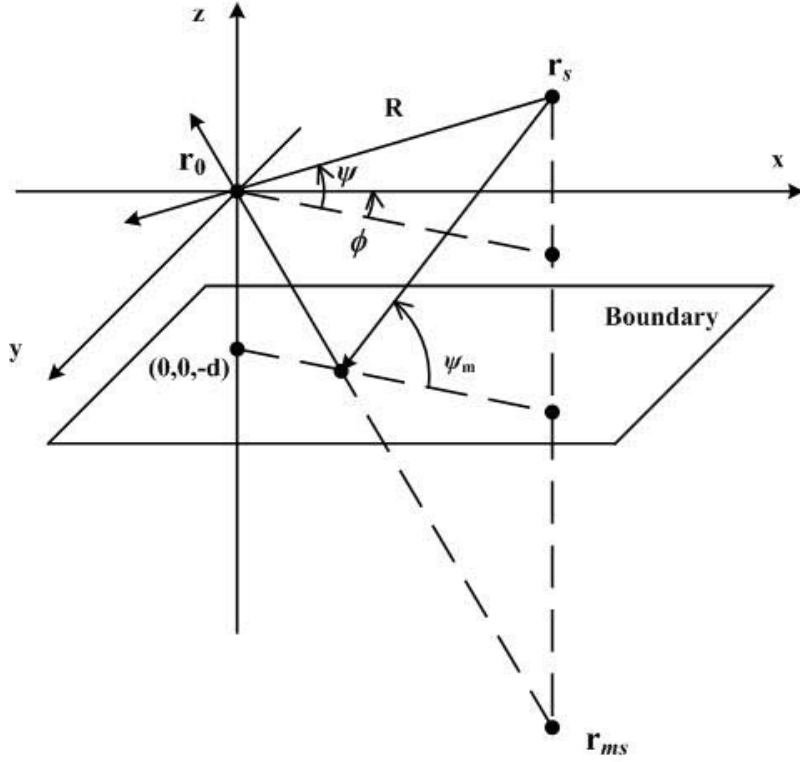
Figure 4.2: Illustration

with identical velocities. This means that the reflected wavenumber vector $\mathbf{k}_r$ is obtained by reflecting the incident wavenumber vector in the plane of the interface.

Note that the wavenumber vector points in the direction of propagation of the wave and has modulus $2\pi/\lambda$, where λ is the wavelength in the fluid. In our coordinate system in Figure 4.2,

$$\mathbf{k}_i = \frac{2\pi}{\lambda} \frac{\mathbf{r} - \mathbf{r}_s}{|\mathbf{r} - \mathbf{r}_s|} \tag{4.29}$$

$$\mathbf{k}_r = \frac{2\pi}{\lambda} \frac{\mathbf{r} - \mathbf{r}_{ms}}{|\mathbf{r} - \mathbf{r}_{ms}|} \tag{4.30}$$

where $\mathbf{r} - \mathbf{r}_s = [x - x_s, y - y_s, z - z_s]^T$ and $\mathbf{r} - \mathbf{r}_{ms} = [x - x_s, y - y_s, z + z_s + 2d]^T$, and $|\cdot|$ denotes the Euclidean distance.

The total field in the fluid is given by the superposition of the incident and reflected waves that interfere to form a standing wave pattern. By combining equation (4.27), (4.28), (4.29), (4.30), the total pressure field at the acoustic vector-sensor $\mathbf{r}_0$ equals

$$
\begin{aligned}
p(\mathbf{r}_0, t) &= p_i(\mathbf{r}_0, t) + p_r(\mathbf{r}_0, t) \\
&= \left[\frac{1}{|\mathbf{r}_0 - \mathbf{r}_s|} \exp\left(-j\frac{2\pi}{\lambda}|\mathbf{r}_0 - \mathbf{r}_s|\right) + \frac{\Gamma(\mathbf{r}_0)}{|\mathbf{r}_0 - \mathbf{r}_{ms}|} \exp\left(-j\frac{2\pi}{\lambda}|\mathbf{r}_0 - \mathbf{r}_{ms}|\right) \right] A \exp(j\omega t) \\
&= a_p \, A \exp(j\omega t)
\end{aligned}
\tag{4.31}
$$

where

$$a_p = \frac{\exp\left(-j\frac{2\pi}{\lambda}\sqrt{x_s^2 + y_s^2 + z_s^2}\right)}{\sqrt{x_s^2 + y_s^2 + z_s^2}} + \frac{\Gamma(\mathbf{r}_0)\exp\left(-j\frac{2\pi}{\lambda}\sqrt{x_s^2 + y_s^2 + z_s^2 + 4dz_s + 4d^2}\right)}{\sqrt{x_s^2 + y_s^2 + z_s^2 + 4dz_s + 4d^2}} \tag{4.32}$$

The total particle velocity at $\mathbf{r}$, i.e., $\mathbf{v}(\mathbf{r}, t)$, is related to the total pressure $p(\mathbf{r}, t)$ by the Eulers equation $\rho_0 \frac{\partial \mathbf{v}(\mathbf{r},t)}{\partial t} = -\nabla p(\mathbf{r}, t)$ (equation 1-3.7 in [145]) of the time harmonic sound where $\mathbf{v}(\mathbf{r}, t) = |\mathbf{v}(\mathbf{r}, t)| e^{j\omega t}$, so that

$$\rho_0 j \omega \mathbf{v}(\mathbf{r}, t) = -\nabla \left[p_i(\mathbf{r}, t) + p_r(\mathbf{r}, t) \right] \tag{4.33}$$

where ρ_0 is the ambient fluid density, $\nabla = \left[\frac{\partial}{\partial x}, \frac{\partial}{\partial y}, \frac{\partial}{\partial z} \right]^T$ denotes the gradient operator in the Cartesian coordinate. Hence the total velocity field at the acoustic vector-sensor $\mathbf{r}_0$ can be expressed as

$$\mathbf{v}(\mathbf{r}_0, t) = \frac{jA \exp(j\omega t)}{\omega \rho_0} \nabla \left[\frac{1}{|\mathbf{r} - \mathbf{r}_s|} \exp\left(-j\frac{2\pi}{\lambda} |\mathbf{r} - \mathbf{r}_s| \right) + \frac{\Gamma}{|\mathbf{r} - \mathbf{r}_{ms}|} \exp\left(-j\frac{2\pi}{\lambda} |\mathbf{r} - \mathbf{r}_{ms}| \right) \right] \Bigg|_{\mathbf{r}=\mathbf{r}_0}$$

$$= \frac{jA\lambda \exp(j\omega t)}{2\pi \rho_0 c} [a_x, a_y, a_z]^T \tag{4.34}$$

where $[a_x, a_y, a_z]^T$ can be calculated with MATLAB Symbolic Math Toolbox as

$$a_x = \left(j\frac{2\pi}{\lambda} \sqrt{x_s^2 + y_s^2 + z_s^2} + 1 \right) \exp\left(-j\frac{2\pi}{\lambda} \sqrt{x_s^2 + y_s^2 + z_s^2} \right) \left(x_s^2 + y_s^2 + z_s^2 \right)^{-\frac{3}{2}} x_s$$

$$+ \left[\left(\frac{j\frac{2\pi}{\lambda} \sqrt{x_s^2 + y_s^2 + z_s^2 + 4dz_s + 4d^2} + 1}{x_s^2 + y_s^2 + z_s^2 + 4dz_s + 4d^2} \right) x_s \Gamma(\mathbf{r}_0) + \frac{\partial \Gamma}{\partial x} \Bigg|_{\mathbf{r}=\mathbf{r}_0} \right]$$

$$\frac{\exp\left(-j\frac{2\pi}{\lambda} \sqrt{x_s^2 + y_s^2 + z_s^2 + 4dz_s + 4d^2} \right)}{\sqrt{x_s^2 + y_s^2 + z_s^2 + 4dz_s + 4d^2}} \tag{4.35}$$

$$a_y = \left(j\frac{2\pi}{\lambda} \sqrt{x_s^2 + y_s^2 + z_s^2} + 1 \right) \exp\left(-j\frac{2\pi}{\lambda} \sqrt{x_s^2 + y_s^2 + z_s^2} \right) \left(x_s^2 + y_s^2 + z_s^2 \right)^{-\frac{3}{2}} y_s$$

$$+ \left[\left(\frac{j\frac{2\pi}{\lambda} \sqrt{x_s^2 + y_s^2 + z_s^2 + 4dz_s + 4d^2} + 1}{x_s^2 + y_s^2 + z_s^2 + 4dz_s + 4d^2} \right) y_s \Gamma(\mathbf{r}_0) + \frac{\partial \Gamma}{\partial y} \Bigg|_{\mathbf{r}=\mathbf{r}_0} \right]$$

$$\frac{\exp\left(-j\frac{2\pi}{\lambda} \sqrt{x_s^2 + y_s^2 + z_s^2 + 4dz_s + 4d^2} \right)}{\sqrt{x_s^2 + y_s^2 + z_s^2 + 4dz_s + 4d^2}} \tag{4.36}$$

$$a_z = \left(j\frac{2\pi}{\lambda} \sqrt{x_s^2 + y_s^2 + z_s^2} + 1 \right) \exp\left(-j\frac{2\pi}{\lambda} \sqrt{x_s^2 + y_s^2 + z_s^2} \right) \left(x_s^2 + y_s^2 + z_s^2 \right)^{-\frac{3}{2}} z_s$$

$$+ \left[-\left(\frac{j\frac{2\pi}{\lambda} \sqrt{x_s^2 + y_s^2 + z_s^2 + 4dz_s + 4d^2} + 1}{x_s^2 + y_s^2 + z_s^2 + 4dz_s + 4d^2} \right) z_s \Gamma(\mathbf{r}_0) + \frac{\partial \Gamma}{\partial z} \Bigg|_{\mathbf{r}=\mathbf{r}_0} \right]$$

$$\frac{\exp\left(-j\frac{2\pi}{\lambda} \sqrt{x_s^2 + y_s^2 + z_s^2 + 4dz_s + 4d^2} \right)}{\sqrt{x_s^2 + y_s^2 + z_s^2 + 4dz_s + 4d^2}} \tag{4.37}$$

Combining equation (4.31) to (4.34), the manifold of the acoustic vector sensor in near-field and near a reflecting boundary can be obtained by omitting the common factors

$$\mathbf{a}_{\text{near-field}}^{\text{near-boundary}} = \left[a_x, \ a_y, \ a_z, \ -j\frac{2\pi}{\lambda} \rho_0 c \, a_p \right]^T \tag{4.38}$$

It can be seen that the acoustic vector-sensor manifold above is in the Cartesian coordinate, and it depends on the source's position $\mathbf{r}_s$. It's more indicative and informative if the manifold could be expressed in the spherical coordinate such that the manifold dependence on the transmitter receiver distance, the receiving DOA can be revealed. Referring to the geometry in Figure 4.2, denote the distance from the source to the acoustic

vector-sensor as R, denote the receiving azimuth and elevation angles at $\mathbf{r}_0$ as ϕ and ψ, respectively. Then with $x_s = R\cos\phi\cos\psi$, $y_s = R\sin\phi\cos\psi$, and $z_s = R\sin\psi$, the manifold in equation (4.38) can be rewritten in spherical coordinate as

$$
\mathbf{a}_{\text{near-field}}^{\text{near-boundary}} = \begin{bmatrix}
\frac{\exp\left(-j\frac{2\pi R}{\lambda}\right)}{R^2}\left(j\frac{2\pi R}{\lambda}+1\right)\cos\phi\cos\psi + \frac{\exp\left(-j\frac{2\pi}{\lambda}\sqrt{R^2+4Rd\sin\psi+4d^2}\right)}{\sqrt{R^2+4Rd\sin\psi+4d^2}} \\
\left[\left(\frac{j\frac{2\pi}{\lambda}\sqrt{R^2+4Rd\sin\psi+4d^2}+1}{R^2+4Rd\sin\psi+4d^2}\right)R\cos\phi\cos\psi\,\Gamma(\mathbf{r}_0)+\frac{\partial\Gamma}{\partial x}\big|_{\mathbf{r}=\mathbf{r}_0}\right], \\[2mm]
\frac{\exp\left(-j\frac{2\pi R}{\lambda}\right)}{R^2}\left(j\frac{2\pi R}{\lambda}+1\right)\sin\phi\cos\psi + \frac{\exp\left(-j\frac{2\pi}{\lambda}\sqrt{R^2+4Rd\sin\psi+4d^2}\right)}{\sqrt{R^2+4Rd\sin\psi+4d^2}} \\
\left[\left(\frac{j\frac{2\pi}{\lambda}\sqrt{R^2+4Rd\sin\psi+4d^2}+1}{R^2+4Rd\sin\psi+4d^2}\right)R\sin\phi\cos\psi\,\Gamma(\mathbf{r}_0)+\frac{\partial\Gamma}{\partial y}\big|_{\mathbf{r}=\mathbf{r}_0}\right], \\[2mm]
\frac{\exp\left(-j\frac{2\pi R}{\lambda}\right)}{R^2}\left(j\frac{2\pi R}{\lambda}+1\right)\sin\psi + \frac{\exp\left(-j\frac{2\pi}{\lambda}\sqrt{R^2+4Rd\sin\psi+4d^2}\right)}{\sqrt{R^2+4Rd\sin\psi+4d^2}} \\
\left[-\left(\frac{j\frac{2\pi}{\lambda}\sqrt{R^2+4Rd\sin\psi+4d^2}+1}{R^2+4Rd\sin\psi+4d^2}\right)R\sin\psi\,\Gamma(\mathbf{r}_0)+\frac{\partial\Gamma}{\partial z}\big|_{\mathbf{r}=\mathbf{r}_0}\right], \\[2mm]
-j\frac{2\pi}{\lambda}\rho_0 c\left[\frac{\exp\left(-j\frac{2\pi R}{\lambda}\right)}{R}+\frac{\Gamma(\mathbf{r}_0)\exp\left(-j\frac{2\pi}{\lambda}\sqrt{R^2+4Rd\sin\psi+4d^2}\right)}{\sqrt{R^2+4Rd\sin\psi+4d^2}}\right]
\end{bmatrix}
\tag{4.39}
$$

If Γ is independent of the position $\mathbf{r}$, and $R\to+\infty$, by noting that $\lim_{R\to+\infty}\left(\sqrt{R^2+4Rd\sin\psi+4d^2}-R\right)=2d\sin\psi$ and $\nabla\Gamma=0$, omitting the common factors and simplifying equation (4.39) results in the far-field near-boundary manifold

$$
\mathbf{a}_{\text{far-field}}^{\text{near-boundary}} = \begin{bmatrix}
\cos\phi\cos\psi\left[1+\Gamma(\mathbf{r}_0)\exp\left(-j\frac{4\pi d\sin\psi}{\lambda}\right)\right], \\
\sin\phi\cos\psi\left[1+\Gamma(\mathbf{r}_0)\exp\left(-j\frac{4\pi d\sin\psi}{\lambda}\right)\right], \\
\sin\psi\left[1-\Gamma(\mathbf{r}_0)\exp\left(-j\frac{4\pi d\sin\psi}{\lambda}\right)\right], \\
-\rho_0 c\left[1+\Gamma(\mathbf{r}_0)\exp\left(-j\frac{4\pi d\sin\psi}{\lambda}\right)\right]
\end{bmatrix}
\tag{4.40}
$$

which is identical to equation (8) in [59]. Note that equation (8) in [59] normalizes the pressure field by $-\rho_0 c$, and normalizes all lengths by the wavelength λ. Although R and d in equation (4.39) can also be normalized by λ, we don't suggest the normalization, because the manifold's dependence on the signal's frequency should not be overlooked.

Furthermore, although equations (4.39) looks complicated, one may see that each component of the manifold vector is a summations of two terms. If the 2nd terms are omitted, the manifold becomes the near-field no-boundary case

$$
\mathbf{a}_{\text{near-field}}^{\text{no-boundary}} = \begin{bmatrix}
\cos\phi\sin\psi \\
\sin\phi\sin\psi \\
\cos\psi \\
\frac{\rho_0 c}{\sqrt{1+\left(\frac{\lambda}{2\pi R}\right)^2}}\exp\left(j\arctan\frac{\lambda}{2\pi R}\right)
\end{bmatrix}
\tag{4.41}
$$

This implies that the manifold variation brought by a near boundary is purely reflected in the 2nd additive terms. It can be easily explained, because the existence of the near boundary produces the additive reflected pressure field and velocity field in equation (4.31) and (4.34).

Similarly, if $R \to +\infty$, then equation (4.41) degenerates to the classic far-field no-boundary acoustic vector-sensor manifold

$$
\mathbf{a}_{\text{far}-\text{field}}^{\text{no}-\text{boundary}} = \begin{bmatrix} \cos\phi\sin\psi \\ \sin\phi\sin\psi \\ \cos\psi \\ \rho_0 c \end{bmatrix} \tag{4.42}
$$

where the pressure field is usually normalized to 1 by the scaler $\rho_0 c$.

4.4.2 Discussion on Reflection Coefficient & Boundary Surface

Denote the specific acoustic impedance on the boundary $Z_s(\psi_m, \omega)$, where ψ_m is the incident angle on the boundary surface in Figure 4.2, then the plane-wave reflection coefficient can be expressed as (equation (5) in [97], equation (2) in [167])

$$
\Gamma_p(\psi_m, \omega) = \frac{Z_s(\psi_m, \omega)\cos\psi_m - \rho_0 c}{Z_s(\psi_m, \omega)\cos\psi_m + \rho_0 c} \tag{4.43}
$$

Denote the boundary loss factor

$$
L(\xi) = 1 + i\sqrt{\pi}\xi\exp(-\xi^2)\text{erfc}\left(-i\xi\right) \tag{4.44}
$$

where $L(+\infty) = 0$, and $L(0) = 1$ (page 69 of [8]). The parameter ξ is also known as the numerical distance, defined by

$$
\xi(\mathbf{r}_s, \omega) = \sqrt{\frac{|\mathbf{r}_m - \mathbf{r}_s|\omega}{2c}}(1 + i)\left[\cos\psi_m + \frac{\rho_0 c}{Z_s(\psi_m, \omega)}\right] \tag{4.45}
$$

Hence, the complex reflection coefficient applied in the near-field spherical wave propagation is specifically determined according to [97]

$$
\Gamma(\mathbf{r}_s, \omega) = \Gamma_p(\psi_m, \omega) + [1 - \Gamma_p(\psi_m, \omega)]L(\xi) \tag{4.46}
$$

Note that the complex reflecting coefficient Γ depends on the source position $\mathbf{r}_s$ (or ψ_m equivalently) and the signal frequency ω, where it's generally a complicated function. However there are some ideal cases of practical interests that simplify the situation. Listed below are three reflection cases [59] which are commonly assumed in acoustics and they are idealized as some typical situation in practice. The common point of these three idealizations is that the Z_s is independent of ψ_m.

(A) If $|Z_s| \to \infty$, then $\Gamma_p \to 1$, and $\Gamma \to 1$ for all incident angles, and for all values of the boundary loss factor. This is usually known as the *perfect reflection*. Such a surface is called a *rigid* boundary and occurs at high frequency in hull-mounted sonar and in room acoustics.

(B) If $|Z_s| \to 0$, then $\Gamma_p \to -1$, and $\Gamma \to 2L(\xi) - 1$. Such a boundary is called *Pressure-release* boundary and occurs at low frequency in a vessel's hull or at the water surface. However, unlike the case in the far-field that the reflection coefficient is independent of the incident angle, the reflection coefficient for near-field depends on both the distance and the incident angle.

(C) If $|Z_s|$ is independent of the incident angle, such a boundary surface is called *locally reacting* boundary. The porous sound-absorbing materials and grass-covered ground could be regarded as locally reacting.

For the rigid boundary, $\Gamma(\mathbf{r}_s, \omega) = 1$ is a constant for any source position and frequency, and the boundary loss factor has no impact on the complex reflection coefficient. The acoustic vector-sensor's manifold is simply shown in equation (4.39) by setting $\frac{\partial \Gamma}{\partial x}\big|_{\mathbf{r}=\mathbf{r}_0} = 0$, $\frac{\partial \Gamma}{\partial y}\big|_{\mathbf{r}=\mathbf{r}_0} = 0$, $\frac{\partial \Gamma}{\partial z}\big|_{\mathbf{r}=\mathbf{r}_0} = 0$, and $\Gamma(\mathbf{r}_0) = 1$.

For the pressure-release and/or locally reacting boundary surfaces, the exact expression of the near-field near-boundary manifold becomes very complicated because it depends on $\frac{\partial \Gamma}{\partial x}\big|_{\mathbf{r}=\mathbf{r}_0}$, $\frac{\partial \Gamma}{\partial y}\big|_{\mathbf{r}=\mathbf{r}_0}$, and $\frac{\partial \Gamma}{\partial z}\big|_{\mathbf{r}=\mathbf{r}_0}$. However, for a even more ideal case where the boundary loss factor is independent of the source position, then the manifold can be simplified by setting $\frac{\partial \Gamma}{\partial x}\big|_{\mathbf{r}=\mathbf{r}_0} = 0$, $\frac{\partial \Gamma}{\partial y}\big|_{\mathbf{r}=\mathbf{r}_0} = 0$, and $\frac{\partial \Gamma}{\partial z}\big|_{\mathbf{r}=\mathbf{r}_0} = 0$ in equation (4.39).

4.5 Summary

This chapter derives the near-field array-manifold for an acoustic vector-sensor, with no-boundary and near-boundary.

For the no-boundary case, comparing with the far-field array-manifold, the near-boundary array-manifold has a complex-phase existing between the pressure measurement and the particle-velocity vector measurement. This phase-difference depends on the wavelength-normalized source-sensor distance $\frac{R}{\lambda}$ and the propagation-medium's $\rho_0 c$, but not on the azimuth-elevation arriving angles. For three-dimensional source-localization, the azimuth-elevation arrival-angle estimation accuracy could remain the same for the near-field case as for the far-field case. However, the distance-estimation could have a wavelength-normalized accuracy that decreases almost linearly with decreasing $\frac{R}{\lambda}$ outside the near field, but becomes largely flat inside the near field. Furthermore, this distance-estimation could also be independent of the source's azimuth-elevation arrival direction.

For the near-boundary case, the proposed near-field array-manifold is much more complicated than the far-field array-manifold. It depends not only on the source's DOA, range, and frequency, but also the gradient of the boundary surface reflection coefficient. However, when the ideal grid boundary is considered, the array-manifold could be largely simplified.

Chapter 5

Near-field "Blind" Source Localization Using a Spatially Extended Acoustic Vector-Sensor

5.1 Preliminary

5.1.1 Literature Review of Source Localization in Sensor Network

Source localization is increasingly important in the sensor network. [109] and [198] overview various localization methods which may be classified into 5 categories.

(1) Global Positioning System (GPS) offers very accurate localization, but requires complicated hardware at each sensor-node. GPS is expensive, power-hungry, hence unsuited for small networks or ad hoc networks.

(2) In the DOA (or AOA) approaches as [19], [87], [84], [28], [2], [94], [141], [75], [107], the source's DOA is estimated at each sensor-node with respect to that node, Each DOA-estimate constitute a straight line of possible locations of the emitter. The intersection of all such lines gives the emitter's location. This DOA-based approach requires at each node the complex and expensive hardware, e.g, antenna-array or ultrasound receiver.

(3) Ranging techniques, such as TOA/TDOA and (Receiving Signal Strength Indicator) RSSI. The TOA/TDOA approaches are often more accurate than RSSI approaches. However, the former approaches require highly accurate time-synchronization and iterative solution to the nonlinear equations. On the contrary, the RSSI-based approaches [96], [169], [30], [162], [29], [204], [90], [4], [49], and [197] require no additional hardware but are sensitive to any changes in the propagation environment.

(4) The Maximum Likelihood (ML) approaches [158], [131], [169], [204], [4], [130], [159], [112], and [182]. can be highly accurate, but require prior knowledge of the noise statistics, computationally an initial guess to start off the iteration.

The scenario in this section is more adverse than many sensor-networking scenarios, where the emitter constitutes a sensor-node in the network [169], [30], [204], [90], [4], [49], [197]. There, the emitter may act cooperatively, for example, emitting a signature waveform a priori known to the other sensors. This chapter deals with the case of a non-cooperative node, in that no such signature a priori info known.

This chapter will deploy a single velocity-sensor triad which is separated from the pressure-sensor. The velocity-sensor triad and the pressure-sensor can thus be regarded as a two-nodes sensor network. However, the to-be-located source here is not a sensor node in the sensor network.

5.1.2 The Proposed Localization Approach with a Spatially Extended Acoustic Vector-Sensor

As shown in the last chapter, when a velocity-sensor triad is located at the coordinates' origin, its 3×1 array manifold equals [125, 115]:

$$\mathbf{a}_v(\phi, \psi) \stackrel{\text{def}}{=} \begin{bmatrix} \sin \psi \cos \phi \\ \sin \psi \sin \phi \\ \cos \psi \end{bmatrix} \tag{5.1}$$

where $\pi/2 \leq \psi \leq \pi/2$ symbolizes the elevation angle measured from the x-y plane, $0 \leq \phi < 2\pi$ denotes the azimuth angle measured from the positive x-axis, $u = \cos \psi \cos \phi$ refers to the direction-cosine along the x-axis, $v = \cos \psi \sin \phi$ refers to the direction-cosine along the y-axis, and $w = \sin \psi$ refers to the direction-cosine along the z-axis.

It is clear from (5.1) that a velocity-sensor triad measures all three Cartesian components of the acoustic-velocity vector-field, thereby recognizing the vector-field nature (i.e., the velocity-field) of the acoustic wavefield. An estimate of (5.1) would allow the estimation of the incident source's azimuth-elevation angle-of-arrival (AOA). This direction-finding approach differs from the more customary interferometry approaches, which deploy only pressure-sensors and which treat the acoustical wavefield merely as a scalar wavefield (i.e., intensity-field).

This velocity-sensor-triad approach of direction finding is versatile: This velocity-sensor-triad array manifold in (5.1) is independent of the incident signal frequency, the incident signal bandwidth, and the incident source's location in the near field as opposed to the far field – all these due to the spatial co-location of all constituent sensors of a velocity-sensor triad. In contrast, an array of spatially displaced pressure-sensors (being a spatial finite-impulse-response (FIR filter)) has a directivity dependent on the frequency-dependent inter-sensor spatial phase-factor.

The measurement model of the velocity-sensor triad was introduced to the signal processing research community in [125] and [59]. Direction-finding algorithms that exploit the vector-sensor's unique array-manifold have been developed for maximum-likelihood-based DOA-estimation [63], [6], for Capon-based spectrum estimation [58], for ESPRIT-based DOA-estimation [187], [188], [190], [191], [172], [205, 196], for MUSIC-based DOA-

estimation [191], [27], for Root-MUSIC-based DOA-estimation [189], for Quaternion-MUSIC-based DOA-estimation [118], for least-squares-based DOA-estimation [60], for beamspace-based DOA-estimation [58], [26], [106], and for DOA-tracking [101], [192].

The present work advances a new approach that exploits the directionality in the acoustic particle-velocity field, in conjunction with the DOA and RSSI methods discussed in the last subsection. The new approach would require a velocity-sensor triad and a dislocated pressure-sensor, each of which is physically compact and may be placed at sensor-nodes in any arbitrary known locations. The acoustic velocity-sensor triad measures the three Cartesian components of the incident acoustic particle-velocity field and reports its estimated RSSI and azimuth-elevation DOA-estimate of the source. The acoustic pressure-sensor measures its RSSI. By fusing the data from the velocity-sensor triad and the pressure-sensor, three-dimensional source localization can be realized. The proposed three-dimensional geolocation algorithm couples the uni-acoustic-vector-sensor DOA estimate [172], with a power-level (RSSI) algorithm to be presented later.

The proposed method needs not communicate the entire data-stream across the sensor-network, as in cross-correlation methods. Moreover, the proposed method can accommodate non-free-space propagation models of path-loss exponent of any arbitrary known value.

Unlike purely RSSI-based methods, the proposed approach can localize the source in 3D space with only two sensor nodes (a velocity-sensor triad and a dislocated pressure-sensor), while the purely RSSI-based methods requires at least 5 sensor nodes [183].

Unlike methods using two or more microphone-arrays, the proposed approach can locate either the narrowband or the wideband source in either far-field or near-field.

The proposed method can contribute to "command, control, communications, computers, intelligence, surveillance and reconnaissance" (C4ISR) systems. For example, aircrafts and helicopters emit sounds at extremely high pressures, and they often constitute the predominant acoustic source despite background noises. This proposed method could thus be useful for unattended passive monitoring of aircrafts and helicopters in the air or on the ground (say, in an airport).

5.2 The Measurement Data Model for the Near-Field Source-Localization Problem Using a "Spatially Extended" Acoustic $Vector$-Sensor

The measurement system is a "spatially distributed" four-component acoustic $vector$-sensor, which consists of (i) a $velocity$-sensor triad centered at the Cartesian coordinates $(0, 0, 0)$ plus (ii) an isotropic pressure-sensor located at $(D, 0, 0)$. Please see Figure 5.1. A point-source, located in the upper half-space of the three-dimensional Cartesian coordinates (x_s, y_s, z_s)[1] in either the near field or the far field, emits a real-valued signal $\sqrt{P_T} s(t)$. The signal has a constant transmitted power P_T, unknown to the receive-sensors. The

---

[1] Or, in the spherical coordinates (r_v, ϕ_s, ψ_s), where $r_v \geq 0$, $0 \leq \phi_s < 360°$ and $0 \leq \psi_s \leq 90°$.
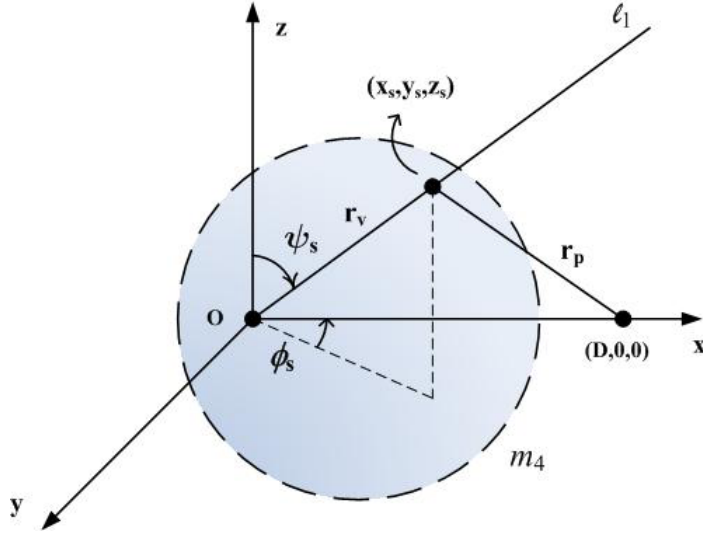
Figure 5.1: Geometry illustration in 3D space.

unit-power signal $s(t)$ may have arbitrary and, possibly, an a priori unknown frequency-spectrum.

The *velocity*-sensor triad makes a 3×1 data-measurement at time t:

$$\mathbf{z}_v(t) = \mathbf{a}_v(\phi_s, \psi_s)\sqrt{P(r_v)}\, s(t - \tau(r_v)) + \mathbf{n}_v(t) \tag{5.2}$$

where $r_v = \sqrt{x_s^2 + y_s^2 + z_s^2}$ symbolizes the unknown separation between the emitter and the velocity-sensor triad, $P(r_v) = \frac{P_T}{r_v^n K}$ denotes the power of the signal at the velocity-sensor triad[2], $\tau(r_v) = \frac{r_v}{c}$ refers to the signal's propagation time from the emitter to the velocity-sensor triad, c represents the propagation speed, and $\mathbf{n}_v(t)$ refers to a zero-mean stochastic sequence of additive noise uncorrelated over time and uncorrelated across its three components.

Similarly, the pressure-sensor makes a scalar measurement at time t:

$$z_p(t) = \sqrt{P(r_p)}\, s(t - \tau(r_p)) + n_p(t) \tag{5.4}$$

where $r_p = \sqrt{(x_s - D)^2 + y_s^2 + z_s^2}$ symbolizes the unknown separation between the emitter and the pressure-sensor, $P(r_p) = \frac{P_T}{r_p^n K}$ denotes the power of the signal at the pressure-sensor, $\tau(r_p) = \frac{r_p}{c}$ refers to the signal's propagation time from the emitter to the pressure-sensor, and $n_p(t)$ refers to an uncorrelated noise zero-mean sequence not cross-correlated with $\mathbf{n}_v(t)$.

---

[2] $P(r_v)$ and $P(r_p)$ relate to the path-loss model of the environment. Usually, the path-loss L_p is regarded as inversely proportional to the power of the distance R from the the transmitter to the receiver, that is, $\frac{L_p}{R^n} = K$ where K is a constant, and n is a positive exponent which usually differs in different propagation environment. When $n = 2$, this is widely known as inverse-square law in physics. Apply the path-loss model to our application,

$$\begin{cases} P(r_v) = \frac{P_T}{r_v^n K} \\ P(r_p) = \frac{P_T}{r_p^n K} \end{cases} \tag{5.3}$$

For different environments, the constant K may also vary. However, before the source estimation algorithm being applied, K in a specific environment could be obtained by measuring the Tx-Rx distance, transmitting and receiving powers in an experiment in that specific environment.

Over N time-instants, the overall observed data equal:

$$\mathbf{Z} = \left[\begin{array}{ccc} \mathbf{z}_v(t_1) & \cdots & \mathbf{z}_v(t_N) \\ z_p(t_1) & \cdots & z_p(t_N) \end{array} \right] = \left[\begin{array}{c} \mathbf{Z}_v \\ \mathbf{z}_p \end{array} \right] \qquad (5.5)$$

The present problem is to estimate $\{\phi_s, \psi_s, r_v\}$ based on $\mathbf{Z}$.

5.3 Localization Algorithm

The source localization is divided into two stages. At the first stage, the direction-of-arrival (DOA) of the receiving signal is estimated by the 3-element vector sensor. At the second stage, the source is located by comparing the receiving power levels between the 3-element vector sensor and the pressure sensor.

5.3.1 Azimuth-Elevation Angle-of-Arrival Estimation Using a Velocity-Sensor Triad

[124], [125], [172].

Towards estimating $\mathbf{a}_v(\phi_s, \psi_s)$, form an acoustic particle-velocity-field correlation-matrix

$$\mathbf{R} = \left[\begin{array}{ccc} \mathbf{z}_v(t_1) & \cdots & \mathbf{z}_v(t_N) \end{array} \right] \left[\begin{array}{ccc} \mathbf{z}_v(t_1) & \cdots & \mathbf{z}_v(t_N) \end{array} \right]^H \qquad (5.6)$$

where the superscript ^{H} denotes the Hermitian transposition.

The velocity-sensor-triad array-manifold $\mathbf{a}_v(\phi_s, \psi_s)$ may be estimated via the eigenvector $\hat{\mathbf{a}}_v$ corresponding to the largest-magnitude eigenvalue of $\mathbf{R}$. In an hypothetical noiseless scenario, $\hat{\mathbf{a}}_v = e^{j\eta}\mathbf{a}_v(\phi_s, \psi_s)$, where η symbolizes an unknown phase.

Hence, (5.1) gives the azimuth-angle and elevation-angle estimates:

$$\hat{\phi}_s = \arctan \frac{[\hat{\mathbf{a}}_v]_2}{[\hat{\mathbf{a}}_v]_1} \qquad (5.7)$$

$$\hat{\psi}_s = \arccos |[\hat{\mathbf{a}}_v]_3| \qquad (5.8)$$

where $[\hat{\mathbf{a}}_v]_k$ symbolizes the kth entry in $\hat{\mathbf{a}}_v$. In terms of the Cartesian coordinates, the incident source must therefore lie on the straight line,

$$\ell_1 = \left\{ x, \ y = \tan\hat{\phi}_s x, \ z = \frac{x}{\cos\hat{\phi}_s \tan\hat{\psi}_s} > 0 \right\} \qquad (5.9)$$

Two-dimensional direction finding has thus been accomplished using a single velocity-sensor triad with *no* prior information of the signal's bandwidth and spectra. This is viable because the array manifold in (5.1) is entirely independent of signal frequency, due to the spatial co-location of its constituent sensors. The complicating effects of a near-field wave-front's curvature is avoided here because of the spatial co-location of the three velocity-sensors.

5.3.2 Received Signal Strength Indication (RSSI)

The estimates $(\hat{P}_v, \hat{P}_p)$ of $P(r_v)$ and $P(r_p)$ may be obtained from (5.5):

$$\hat{P}_v \quad = \quad \frac{1}{N} \left[\mathbf{Z}_v^{(1)}, \mathbf{Z}_v^{(2)}, \mathbf{Z}_v^{(3)} \right] \left[\mathbf{Z}_v^{(1)}, \mathbf{Z}_v^{(2)}, \mathbf{Z}_v^{(3)} \right]^H \tag{5.10}$$

$$\hat{P}_p \quad = \quad \frac{1}{N} \mathbf{z}_p \mathbf{z}_p^H, \tag{5.11}$$

where $\mathbf{Z}_v^{(1)}$, $\mathbf{Z}_v^{(2)}$, and $\mathbf{Z}_v^{(3)}$ are the 1st, 2nd and 3rd row of $\mathbf{Z}_v$, respectively.

Let P_T be the emitter's transmission power that produces (a) $P(r_v)$ at the velocity-sensor triad located at a distance of r_v from the emitter, and (b) $P(r_p)$ at the pressure-sensor at a distance of r_p from the emitter. The propagation-path power-loss model gives:

$$\hat{P}_v \quad = \quad \frac{P_T}{r_1^n K} \tag{5.12}$$

$$\hat{P}_p \quad = \quad \frac{P_T}{r_2^n K}. \tag{5.13}$$

The incident source must then lie on a spherical surface of radius r_1 centered at the velocity-sensor triad at $(0,0,0)$, as well as on a spherical surface of radius r_2 centered at the pressure-sensor at $(D,0,0)$. These two spheres are defined, respectively, as

$$x^2 + y^2 + z^2 \quad = \quad r_1^2 \tag{5.14}$$

$$(x - D)^2 + y^2 + z^2 \quad = \quad r_2^2. \tag{5.15}$$

These two spheres intersect as this following circle perpendicular to the x-axis:

$$\ell_2 : \quad \begin{cases} x & = \quad \frac{1}{2D} \left[\left(\frac{P_T}{\hat{P}_v K} \right)^{\frac{2}{n}} - \left(\frac{P_T}{\hat{P}_p K} \right)^{\frac{2}{n}} \right] + \frac{D}{2} \\ y^2 + z^2 & = \quad \left(\frac{P_T}{\hat{P}_v K} \right)^{\frac{2}{n}} - x^2, \end{cases} \tag{5.16}$$

which is a circle perpendicular to the x-axis.

As P_T varies, the circle ℓ_2 would span a curved manifold m_3. To determine this manifold, combine (5.12), (5.13), (5.14), and (5.15) to eliminate P_T to give:

$$m_3 : \quad \frac{x^2 + y^2 + z^2}{(x - D)^2 + y^2 + z^2} \quad = \quad \frac{\beta}{\alpha} \tag{5.17}$$

where $\alpha = \left(\hat{P}_v \right)^{\frac{2}{n}}$ and $\beta = \left(\hat{P}_p \right)^{\frac{2}{n}}$.

The intersection between the straight line ℓ_1 and the surface m_3 gives the emitter's three-dimensional location.

For $\hat{P}_v = \hat{P}_p$, equation (5.17) degenerates to a plane perpendicular to the x-axis. Combine (5.9) and (5.17) to give the estimates:

$$\begin{cases} \hat{x} = \frac{D}{2} \\ \hat{y} = \frac{aD}{2} \\ \hat{z} = \frac{bD}{2} \end{cases} \tag{5.18}$$

where $a = \tan \hat{\phi}_s$ and $b = \frac{1}{\cos \hat{\phi}_s \tan \hat{\psi}_s}$.

For $\hat{P}_v \neq \hat{P}_p$, equation (5.17) can be rewritten as

$$m_4 : \quad \left(x - \frac{D\beta}{\alpha - \beta}\right)^2 + y^2 + z^2 \quad = \quad \left(\frac{D\sqrt{\alpha\beta}}{\alpha - \beta}\right)^2 \tag{5.19}$$

which represents a sphere. Please see Figure 5.1.

combine (5.9) and (5.19) to give the estimates:

$$\begin{cases} \hat{x} = \frac{-D\beta \pm D\sqrt{\beta^2 + \beta(\alpha - \beta)(1+a^2+b^2)}}{(\alpha - \beta)(1+a^2+b^2)} \\ \hat{y} = a\hat{x} \\ \hat{z} = b\hat{x} \end{cases} \tag{5.20}$$

As in the over-the-horizon air-defense application, the enemy's signal source is presumed to be nearer to the velocity-sensor than the pressure sensor. Hence the received power level at the velocity-sensor is expected to be higher than the received power level at the pressure-sensor, that is, $\hat{P}_v > \hat{P}_p$, or $\alpha > \beta$.

When $\alpha > \beta$,

$$\beta^2 + \beta(\alpha - \beta)\left(1 + a^2 + b^2\right) \geq \beta^2 + \beta(\alpha - \beta) = \alpha\beta > \beta^2 > 0 \tag{5.21}$$

Let $\hat{x}_+$ and $\hat{x}_-$ denote the two x-axis solutions in (5.20), and apply the second inequality to these two solutions, then it's clear that $\hat{x}_+ > 0$ and $\hat{x}_- < \frac{-2D\beta}{(\alpha-\beta)(1+a^2+b^2)} < 0$. Note that the last inequality guarantees that the solutions are real.

The corresponding solutions of $\hat{x}_+$ and $\hat{x}_-$ on z-axis must have opposite sign because $\hat{x}_+ \hat{x}_- < 0$. From equation (5.9), the straight line ℓ_1 always has $z > 0$. Hence, whether $\hat{x}_+$ or $\hat{x}_-$ should be picked is determined by the direction of ℓ_1.

5.4   Elimination of The Ambiguity

Let $\hat{x}_+$ and $\hat{x}_-$ denote the two x-axis solutions in (5.20). There are three disjoint cases, depending on whether $\beta^2 + \beta(\alpha - \beta)\left(1 + a^2 + b^2\right)$ exceeds, equals, or is less than zero. These cases are separately discussed in the three following subsections. Because α, β, a, and b are all obtainable from the observed data $\mathbf{Z}$, the selection among these three case is by the data.

5.4.1   If $\beta^2 + \beta(\alpha - \beta)\left(1 + a^2 + b^2\right) > 0$

Under condition A, $\hat{x}_+$ and $\hat{x}_-$ are both real-value and $\hat{x}_+ \neq \hat{x}_-$.

If $\hat{P}_v > \hat{P}_p$ ($\alpha > \beta$), then

$$\sqrt{\beta^2 + \beta(\alpha - \beta)\left(1 + a^2 + b^2\right)} \geq \sqrt{\beta^2 + \beta(\alpha - \beta)} = \sqrt{\alpha\beta} > \beta \tag{5.22}$$

The first inequality holds because $(1 + a^2 + b^2) \geq 1$. From the first equation of (5.20), it's clear that $\hat{x}_+ > 0$ and $\hat{x}_- < \frac{-2D\beta}{(\alpha-\beta)(1+a^2+b^2)} < 0$. Because $0 < \phi_s < 90°$ and $0 < \theta_s < 90°$, $\hat{x}_-$ means this intersection is not at the first octant of the Cartesian coordinate. So this intersection is not the location estimate and the ambiguity is eliminated because the real

estimate is $\hat{x}_s = \hat{x}_+$. This elimination of ambiguity is easy to understand because when the velocity-sensor triad is inside the sphere ℓ_3, the line ℓ_1 intersects the sphere ℓ_3 at two points which are on the opposite directions. However, our DOA estimation suggests only one of these two directions. Hence, the ambiguity is eliminated.

If $\hat{P}_v = \hat{P}_p$ ($\alpha = \beta$), the sphere ℓ_3 degenerates to a plane, and there is only one solution without ambiguity which is already given out in the last section as $\hat{x}_s = \hat{x}_+ = \hat{x}_- = \frac{D}{2}$.

If $\hat{P}_v < \hat{P}_p$ ($\alpha < \beta$), then

$$\sqrt{\beta^2 + \beta(\alpha - \beta)(1 + a^2 + b^2)} \leq \sqrt{\beta^2 + \beta(\alpha - \beta)} = \sqrt{\alpha\beta} < \beta \qquad (5.23)$$

From the first equation of (5.20), it's clear that $0 < \hat{x}_+ < \hat{x}_- < \frac{-2D\beta}{(\alpha-\beta)(1+a^2+b^2)}$, which means the two intersections between ℓ_1 and ℓ_3 are all at the first octant, and the ambiguity can not be eliminated as in the case where $\hat{P}_v > \hat{P}_p$.

Note that the pressure sensor locates at $(D, 0, 0)$, let's consider the following factorization.

$$
\begin{aligned}
\hat{x} - D &= \frac{-D\beta \pm D\sqrt{\beta^2 + \beta(\alpha - \beta)(1 + a^2 + b^2)}}{(\alpha - \beta)(1 + a^2 + b^2)} - D \\
&= \frac{D\sqrt{\beta + (\alpha - \beta)(1 + a^2 + b^2)}\left(-\sqrt{\beta + (\alpha - \beta)(1 + a^2 + b^2)} \pm \sqrt{\beta}\right)}{(\alpha - \beta)(1 + a^2 + b^2)}
\end{aligned}
\qquad (5.24)
$$

From equation (5.24), it can be seen that $\hat{x}_+ - D < 0$ and $\hat{x}_- - D > 0$, which means $\hat{x}_+$ and $\hat{x}_-$ are at two sides of the pressure sensor's x-coordinate D respectively. In our application, since the pressure sensor locates right beside boundary (could be a wall of a room), and the source is actually inside this bounding space, the ambiguity is physically eliminated. The location estimate is $\hat{x}_s = \hat{x}_+$.

5.4.2   If $\beta^2 + \beta(\alpha - \beta)(1 + a^2 + b^2) = 0$

Under this condition, $(\alpha - \beta)(1 + a^2 + b^2) = -\beta$. And there's only one intersection between the line ℓ_1 and the sphere ℓ_3, without ambiguity. This solution can be derived out from equation (5.20) as

$$
\begin{cases}
\hat{x}_s = D \\
\hat{y}_s = aD \\
\hat{z}_s = bD
\end{cases}
\qquad (5.25)
$$

Note that the reason why there is no ambiguity is different from the one in the last subsection where $\hat{P}_v = \hat{P}_p$. In that case, there's no ambiguity because the sphere ℓ_3 degenerates to a plane and there is only one intersection between the line ℓ_1 and the plane. Here, the line ℓ_1 cut the sphere ℓ_3 at the only point.

5.4.3   If $\beta^2 + \beta(\alpha - \beta)(1 + a^2 + b^2) < 0$

Under this condition, there's on real-value solution for equation (5.20), which indicates that the line ℓ_1 and the sphere ℓ_3 have no intersection. This happens when the estimate $\hat{P}_v$, $\hat{P}_h$, $\hat{\phi}_s$ and $\hat{\theta}_s$ are not accurate. However, it doesn't mean that we have no way to

do the estimation at all. In this case, a numerical search method is used to estimate the source. As one may foresee, usually the estimation will not be accurate when we are forced to use this method.

To numerically find the estimate of the source location, the following algorithm could be applied. Since the source's DOA is estimated, the line ℓ_1 is determined. Assume on grid point i of ℓ_1, a series of hypothesized power levels are assumed as $P_{j,i}, j = 1, 2, \ldots$. Their corresponding receiving power levels at the velocity-sensor triad and the pressure sensor can be calculated from the path-loss model as $P_{j,i}(r_v)$ and $P_{j,i}(r_p)$, respectively. Find the least squared error of grid point i as $\text{LSE}_i = \min_{j=1,2,\ldots} \left(|P_{j,i}(r_v) - \hat{P}_v|^2 + |P_{j,i}(r_p) - \hat{P}_p|^2 \right)$. And then the estimate of the source location is the grid point which corresponds to the smallest LSE among $\text{LSE}_i, i = 1, 2, \ldots$.

5.5 Cramer-Rao Bound Analysis for Sinusoid Source Signal

5.5.1 CRB Derivation

In this section, the Cramer-Rao bound of the proposed measurement model will be analyzed. Note that in our proposed measurement model, the only characteristic of the source signal $\sqrt{P_s}s(t)$ and the noise $\mathbf{n}_v(t)$, $n_p(t)$ is that they should have time invariant power. In other words, the source signal needs not to be narrow band, the noises need not to be white or Gaussian as in many previous research works, which is one of the major advantages of the proposed measurement model. However, to simplify the analysis, the following assumptions are made:

A1 $\mathbf{n}_v(t)$ and $n_p(t)$ are zero-mean white Gaussian processes not cross-correlated with each other. The spatial covariance matrix for $[\mathbf{n}_v^T(t), n_p(t)]^T$ is $\Gamma = \sigma^2 \mathbf{I}_4$, where $\mathbf{I}_i$ is i-order identity matrix, σ^2 is an unknown deterministic constant.

A2 The source signal is sinusoid with power P_s, radial frequency ω_s, and initial phase ϵ_s, all unknown deterministic constants.

Thus, for the proposed near-field path-loss measurement model with dislocated acoustic vector sensor, the data model can be rewritten from equation (5.2) and (5.4) as

$$\mathbf{Z}(t) = \begin{bmatrix} \mathbf{a}_v(\phi_s, \psi_s) A_v \sin\left[\omega_s \left(t - \frac{r_v}{c}\right) + \epsilon_s\right] \\ A_p \sin\left[\omega_s \left(t - \frac{r_p}{c}\right) + \epsilon_s\right] \end{bmatrix} + \begin{bmatrix} \mathbf{n}_v(t) \\ n_p(t) \end{bmatrix} \tag{5.26}$$

where $A_v = \sqrt{\frac{2P_s}{r_v^n K}}$, $A_p = \sqrt{\frac{2P_s}{r_p^n K}}$, $r_p = \sqrt{r_v^2 - 2Dr_v \cos\phi_s \sin\psi_s + D^2}$.

Define $\boldsymbol{\theta} = [\phi_s, \psi_s, r_v, P_s, \omega_s, \epsilon_s, \sigma^2]^T$. Under assumptions **A1** and **A2**, $\mathbf{Z} \sim \mathrm{N}(\boldsymbol{\mu}(\boldsymbol{\theta}), \boldsymbol{\Gamma}(\boldsymbol{\theta}))$, where

$$\boldsymbol{\mu}(\boldsymbol{\theta}) \stackrel{\text{def}}{=} \begin{bmatrix} A_v \, \mathbf{a}_v \otimes \mathbf{s}_1 \\ A_p \, \mathbf{s}_2 \end{bmatrix}, \tag{5.27}$$

$$\boldsymbol{\Gamma}(\boldsymbol{\theta}) = \sigma^2 \mathbf{I}_{4N}, \tag{5.28}$$

$$\mathbf{s}_1 \stackrel{\text{def}}{=} \begin{bmatrix} \sin\left[\omega_s\left(t_1 - \frac{r_v}{c}\right) + \epsilon_s\right] \\ \sin\left[\omega_s\left(t_2 - \frac{r_v}{c}\right) + \epsilon_s\right] \\ \vdots \\ \sin\left[\omega_s\left(t_N - \frac{r_v}{c}\right) + \epsilon_s\right] \end{bmatrix}, \tag{5.29}$$

$$\mathbf{s}_2 \stackrel{\text{def}}{=} \begin{bmatrix} \sin\left[\omega_s\left(t_1 - \frac{r_p}{c}\right) + \epsilon_s\right] \\ \sin\left[\omega_s\left(t_2 - \frac{r_p}{c}\right) + \epsilon_s\right] \\ \vdots \\ \sin\left[\omega_s\left(t_N - \frac{r_p}{c}\right) + \epsilon_s\right] \end{bmatrix}, \tag{5.30}$$

[3] and $\otimes$ denotes the Kronecker product, P_s, ω_s, ϵ_s and σ^2 are nuisance parameters.

Hence, the FIM (Fisher Information Matrix) with respect to $\boldsymbol{\theta}$ equals [77]

$$\lfloor \mathbf{J}(\boldsymbol{\theta}) \rfloor_{i,j} = \left(\frac{\partial \boldsymbol{\mu}(\boldsymbol{\theta})}{\partial \theta_i}\right)^T \boldsymbol{\Gamma}^{-1}(\boldsymbol{\theta}) \left(\frac{\partial \boldsymbol{\mu}(\boldsymbol{\theta})}{\partial \theta_j}\right) + \frac{1}{2}\mathrm{tr}\left[\boldsymbol{\Gamma}^{-1}(\boldsymbol{\theta})\frac{\partial \boldsymbol{\Gamma}(\boldsymbol{\theta})}{\partial \theta_i}\boldsymbol{\Gamma}^{-1}(\boldsymbol{\theta})\frac{\partial \boldsymbol{\Gamma}(\boldsymbol{\theta})}{\partial \theta_j}\right] \tag{5.31}$$

where $\lfloor \cdot \rfloor_{i,j}$ represents the (i,j)-th entry of the matrix.

The elements of the vector $\partial \boldsymbol{\mu}(\boldsymbol{\theta})/\partial \boldsymbol{\theta}$ are

$$\frac{\partial \boldsymbol{\mu}(\boldsymbol{\theta})}{\partial \phi_s} = \begin{bmatrix} A_v \frac{\partial \mathbf{a}_v}{\partial \phi_s} \otimes \mathbf{s}_1 \\ \frac{\partial A_p}{\partial \phi_s} \mathbf{s}_2 + A_p \frac{\partial \mathbf{s}_2}{\partial \phi_s} \end{bmatrix} \tag{5.32}$$

$$\frac{\partial \boldsymbol{\mu}(\boldsymbol{\theta})}{\partial \psi_s} = \begin{bmatrix} A_v \frac{\partial \mathbf{a}_v}{\partial \psi_s} \otimes \mathbf{s}_1 \\ \frac{\partial A_p}{\partial \psi_s} \mathbf{s}_2 + A_p \frac{\partial \mathbf{s}_2}{\partial \psi_s} \end{bmatrix} \tag{5.33}$$

$$\frac{\partial \boldsymbol{\mu}(\boldsymbol{\theta})}{\partial r_v} = \begin{bmatrix} \frac{\partial A_v}{\partial r_v} \mathbf{a}_v \otimes \mathbf{s}_1 + A_v \mathbf{a}_v \otimes \frac{\partial \mathbf{s}_1}{\partial r_v} \\ \frac{\partial A_p}{\partial r_v} \mathbf{s}_2 + A_p \frac{\partial \mathbf{s}_2}{\partial r_v} \end{bmatrix} \tag{5.34}$$

$$\frac{\partial \boldsymbol{\mu}(\boldsymbol{\theta})}{\partial P_s} = \begin{bmatrix} \frac{\partial A_v}{\partial P_s} \mathbf{a}_v \otimes \mathbf{s}_1 \\ \frac{\partial A_p}{\partial P_s} \mathbf{s}_2 \end{bmatrix} \tag{5.35}$$

$$\frac{\partial \boldsymbol{\mu}(\boldsymbol{\theta})}{\partial \omega_s} = \begin{bmatrix} A_v \mathbf{a}_v \otimes \frac{\partial \mathbf{s}_1}{\partial \omega_s} \\ A_p \frac{\partial \mathbf{s}_2}{\partial \omega_s} \end{bmatrix} \tag{5.36}$$

$$\frac{\partial \boldsymbol{\mu}(\boldsymbol{\theta})}{\partial \epsilon_s} = \begin{bmatrix} A_v \mathbf{a}_v \otimes \frac{\partial \mathbf{s}_1}{\partial \epsilon_s} \\ A_p \frac{\partial \mathbf{s}_2}{\partial \epsilon_s} \end{bmatrix} \tag{5.37}$$

$$\frac{\partial \boldsymbol{\mu}(\boldsymbol{\theta})}{\partial \sigma^2} = \mathbf{O}_{4N,1} \tag{5.38}$$

where $\mathbf{O}_{i,j}$ is $i \times j$ zero matrix.

---

[3]In the 2nd equation above, note that $\boldsymbol{\Gamma}$ who represents the temporal-spatial covariance is a 4N-by-4N matrix but not 4-by-4.

Using equation (5.32) to (5.38), the FIM $\mathbf{J}(\boldsymbol{\theta})$ can be element-wise obtained. Hence, the Cramer-Rao bound for ϕ_s, ψ_s and r_v are [77]

$$\mathrm{CRB}(\phi_s) = \lfloor \mathbf{J}^{-1}(\boldsymbol{\theta}) \rfloor_{1,1} \tag{5.39}$$

$$\mathrm{CRB}(\psi_s) = \lfloor \mathbf{J}^{-1}(\boldsymbol{\theta}) \rfloor_{2,2} \tag{5.40}$$

$$\mathrm{CRB}(r_v) = \lfloor \mathbf{J}^{-1}(\boldsymbol{\theta}) \rfloor_{3,3} \tag{5.41}$$

5.5.2 Simulation

In the simulation, the source signal is modeled as a sinusoid wave with constant power $P_s = 10^4$. The source location in near-field is ($\phi_s = 102°, \psi_s = 23°, r_v = 12$) (i.e. ($x_s = -0.9749, y_s = 4.5863, z_s = 11.0461$)). The separation between the velocity-sensor triad and the pressure-sensor is $D = 20$. For path-loss model, the common free space model is used, where $n = 2$ and $K = 1$. Totally $N = 500$ time samples were used in the simulation.

100 Monte Carlos runs are conducted for signal to noise ratio (SNR) from -10 dB to 60 dB. The standard deviation of estimates of azimuth, elevation and radial distance, together with the Cramer-Rao bounds are shown in Figure 5.2a to 5.3a, respectively. From the figures, the standard deviations of $\hat{\phi}$ is less than 0.1 when SNR is approximately no less than 2 dB, the standard deviations of $\hat{\psi}$ is less than 0.1 when SNR is approximately no less than -4 dB, and the standard deviations of $\hat{r}_v$ is less than 1 when SNR is approximately no less than 7 dB.
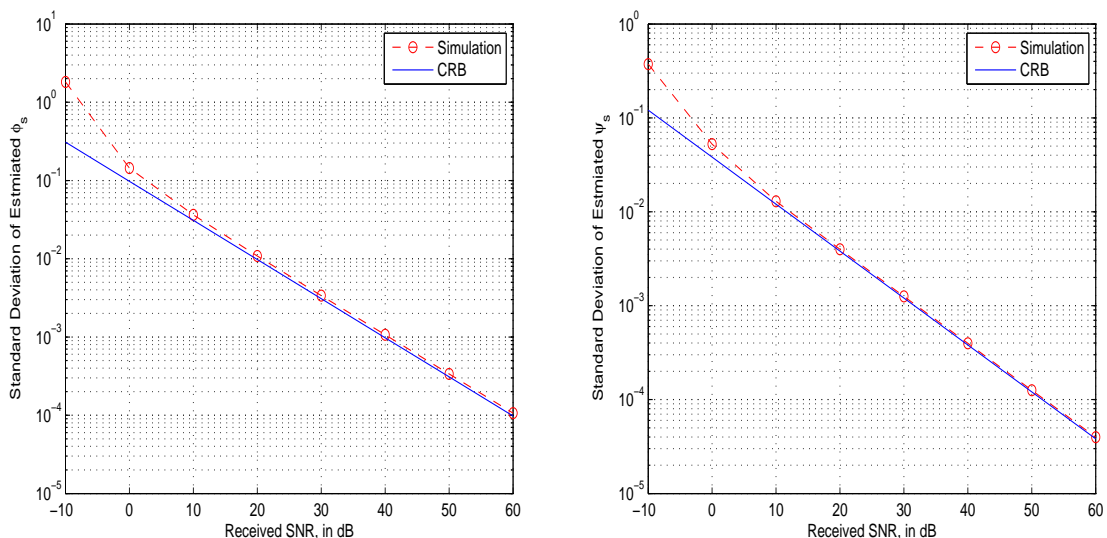
Figure 5.2a: Standard deviation of $\hat{\phi}_s$ versus received SNR over 100 Mont Carlo simulation, $N = 500$

Figure 5.2b: Standard deviation of $\hat{\psi}_s$ versus received SNR over 100 Mont Carlo simulation, $N = 500$

Let $e_s = \sqrt{(\hat{x}_s - x_s)^2 + (\hat{y}_s - y_s)^2 + (\hat{z}_s - z_s)^2}$ denotes the source location estimation error, which determines the largest radius of a sphere containing all the estimated source location. The relative-estimation-error $\left(\frac{e_s}{r_v}\right)$ hence indicates the accuracy of the estimation and the performance of the source localization algorithm. Figure 5.4 shows the mean
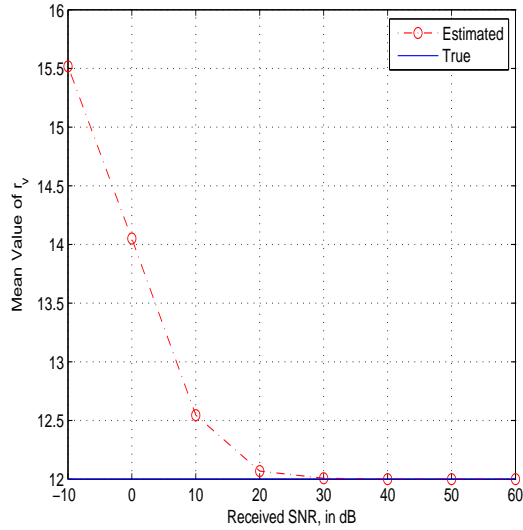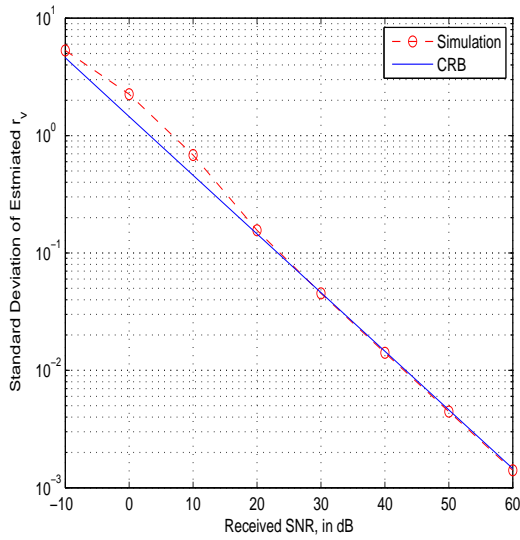
Figure 5.3a: Standard deviation of $\hat{r}_v$ versus received SNR over 100 Mont Carlo simulation, $N = 500$

Figure 5.3b: Mean value of $\hat{r}_v$ versus received SNR
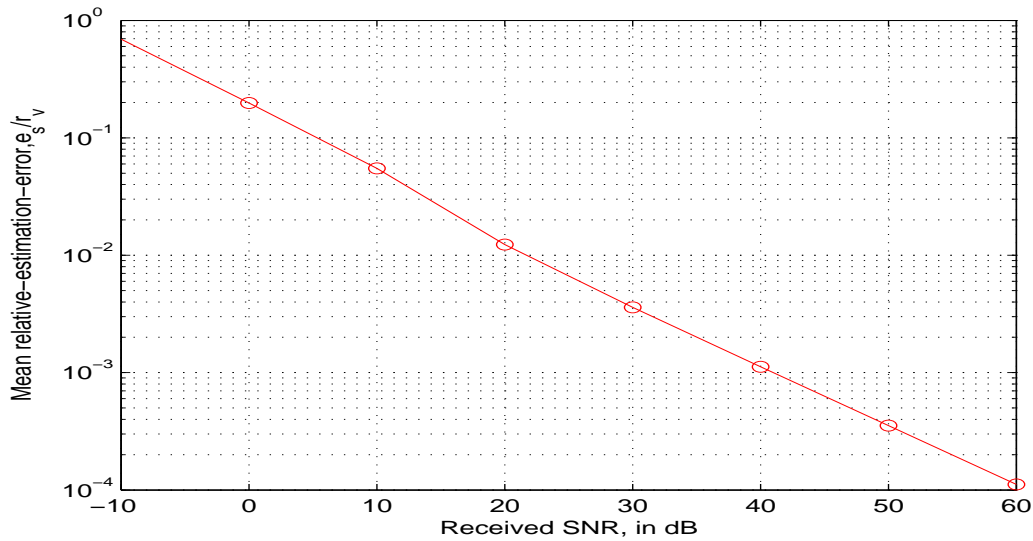
Figure 5.4: Mean relative-estimation-error versus received SNR

relative-estimation-error versus signal to noise ratio (SNR). It can be seen that the mean relative-estimation-error of the source location in 3D space is within 1% of the radial distance from the source to the velocity-sensor triad, when the SNR is no less than approximate 5 dB.

5.6 Summary

In this chapter, we proposes a DOA and RSSI-based geolocation algorithm with a spatially extended acoustic vector-sensor to locate a near-field source in 3D space. The proposed algorithm needs no iterative and/or grid search, and no priori information of the noise statistics. The algorithm is simple and fast, which is very adequate to small and/or ad hoc networks. The closed-form solution is derived, and the CRB of the measurement model is analyzed.

Chapter 6

Beacon-Aided Adaptive Localization of Noise-Sources Aboard a Pass-By Rail-Car Using a Track-Side Microphone-Array

6.1 Preliminary

Railway noise-pollution degrades the public health of neighborhoods near rail-tracks. The World Health Organization and the European Commission both warn of adverse physiological effects for humans under long exposure to high noise levels. These adverse effects include hearing impairment in children and cardiovascular harm. Such health-hazardous train noise-pollution is especially problematic in densely populated cities, like Hong Kong. Indeed, 16% of Hong Kong's population is exposed *at home* to unacceptably loud traffic noise. Furthermore, train-noise investigation is increasingly imperative in many countries, due to a modal shift from road-transport and air-transport, to rail-transport for environmental reasons.

Annoying and health-hazardous noise-pollution could be reduced if the offending noise-sources' individual locations could be pin-pointed on the rail-car carriage. Such train noises are highly varied and unpredictable in their temporal / spectral / spatial / directional structures, because the noises arise amid complex factors like the train speed, the roughness of the wheel/rail, the aerodynamic contours of the rail-car's carriage, the rail-car's internal components.

(a) There can be **no** assumption of any temporal stationarity in the noise waveforms, which could instead be impulsive, on-and off irregularly.

(b) The noise-sources are generally not point-like in spatial extent, nor emitting isotropically over the azimuth and the elevation. Instead, the onboard noise-sources likely produce spatially diffuse and directional echoes.

(c) The rail-car noise-sources may lie in the near field of the roadside receiving-microphone(s), *in*validating the customary planar-wavefront assumption.

(d) These onboard noise-sources move through three-dimensional space with a variable speed (unknown to the algorithm), as the rail-car treads along its track (which may be curved and has varying elevation).

(e) These onboard noise-sources move in a cluster, but present themselves to the roadside receiving-microphone(s) at varying aspect-angles as the track twists and turns.

(f) Localization needs to be achieved despite loud interfering sound-sources (e.g., car traffic, construction noise, pedestrian noise) that are common in urban neighborhoods, but that are altogether uncontrollable, a priori unknown, and unpredictable.

The use of an array of multiple microphones, instead of a single microphone, allows azimuth (or azimuth-elevation) directional beam-forming. Wayside emissions (from acoustic sources aboard a pass-by train) have been measured by an immobile microphone-array placed along the track-side (since at least as early as the late 1970s) in [80, 9, 10, 21, 175, 11, 120, 64, 173, 40, 22, 151, 81, 117]. However, [80, 21, 175, 11, 120, 64, 40, 151, 81, 117] explain little or nothing of the beamforming algorithm used. They appear to be using the traditional "delay-and-sum" (DAS) algorithm or the "sweeping focus" algorithm in [9], [10]. The "delay-and-sum" (DAS) beamformer forms a spatial filter, focussed towards a pre-set direction-of-arrival, which may be temporally adjusted to track the pass-by rail-car's movement in the "sweeping focus" mode. The rail-car's movement is often estimated by auxiliary infrastructure, such as infrared light barriers [9, 10, 11], optical gates [21], [173], radar, or video cameras. The microphone-array's "delay-and-sum" beamformer, in order to track the mobile train, would "sweep" its focus in synchronization with the radar / video estimate of the train's movement. All these presume (A) a pre-existing infrastructure of radar / video train-tracking apparatus, and (B) prior synchronization of the radar / video system with the microphone array.

To avoid such pre-existing infra-structure and prior synchronization, this paper proposes a simple measurement-system consisting of:

(i) an array of calibrated microphones placed at a *un*known location besides a rail-track of *un*known spatial geometry.

(ii) two humanly *in*audible acoustic beacons at known locations on the exterior of the rail-car carriage near the carriage's two ends.

No other track-side auxiliary hardware (such as infrared light barrier, radar, photo cells, or video cameras needed in many existing systems) will be required in the proposed scheme to track the moving train's motion. This hardware simplification will enhance system affordability, operational simplicity, and measurement accuracy.

This work is the first in the open literature, to the best of the authors' knowledge, to propose the use of on-board acoustic beacon signals to self-synchronize with

the microphone-array and to track the rail-car. [1] These beacons will provide reference-signals (with time-frequency characteristics a priori known to the microphone-array), for "reference-signal distortionless-response minimum-variance" (DRMV) beamforming at the microphone-array, to track the rail-car's motions. These beacons have these characteristics:

(1) The beacons will be placed near the rail-car carriage's two ends to facilitate interpolative scanning of the carriage's middle sections.

(2) The beacons will be placed away from the likely locations of the dominant noise-sources[2]

(3) Each beacon's acoustic emittance will be narrowband, so that each beacon-signal may be isolated using narrowband bandpass filtering, resulting in minimal "contamination" from the noise-sources. This means that much of the noise-sources' power (which lies outside this narrow passband) would not affect the DRMV beamforming.

(4) The beacons are to transmit at an intensity inaudible to humans, who may be on or off the train.

These beacon-aided rail-car tracking also means that no prior knowledge is any longer needed of the spatial geometry between the rail-track and the roadside microphone-array. This contrasts with [80, 9, 10, 21, 175, 11, 120, 64, 173, 40, 22, 151, 81, 117] – all of which appear to need such prior knowledge.

Moreover, [80, 9, 10, 175, 120, 64, 173, 81] achieve only one-dimensional source-localization along the length of the rail-car, whereas [21, 11, 40, 22, 151, 117] are capable for two-dimensional length-height source-localization. In contrast, this proposed scheme can potential localize the sources in three dimension, along the rail-car's length, height, and width.

The rest of this paper is organized as follows: Section 6.2 will describe the first algorithmic step in the proposed scheme – beacon-aided rail-car *tracking*. Section 6.3 will describe the second algorithmic step in the proposed scheme – localization of the onboard noise-sources with respect to the moving rail-car's carriage. Section 6.4 will validate the proposed scheme via Monte Carlo simulations. Section 6.5 will do the same via anechoic chamber testing. Section 6.6 will conclude the entire paper.

---

[1]Beacon sources are graphically indicated in a Bruel & Kjaer Power-Point file, entitled "Pass-By Beam-forming", which contains no further information on the "why", the "what", the "for what", or the "how" of the "beacons".

[2]Prior train-noise studies show that the rail-car's dominant wayside noises come from the rail wheels.
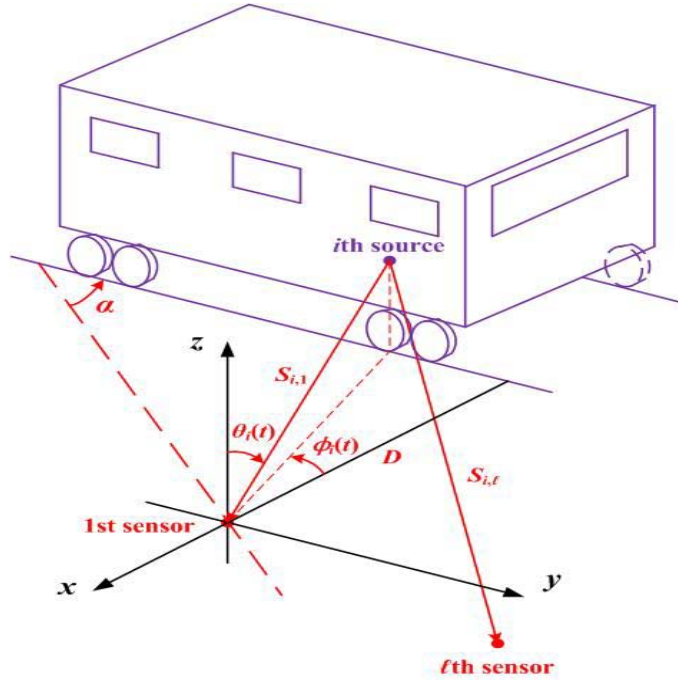
Figure 6.1: The spatial geometry between the ith onboard emitter impinging from an elevation-angle of $\theta_i(t)$ and an azimuth-angle of $\phi_i(t)$) towards the $\ell = $ 1st microphone (which lies on the x-axis).

6.2 The Proposed Algorithmic Step #1: Beacon-Aided Rail-Car Tracking

6.2.1 The Measurement Model for Subsequent Algorithmic Development

To estimate the three-dimensional positions of the sound sources, needed is an array at least two-dimensional in aperture. Place such an array of L microphones next to a straight section (which needs not to be) of the rail-track. Traveling down this rail-track is a rail-car, equipped with two acoustic beacons, as described in the preceding section. In between these two beacons, there exist a (possibly unknown) number of polluting noise-sources. Figure 6.1 show the spatial geometry between the pass-by rail-car and the microphone-array. This figure also define the mathematical notation subsequently used.

As the rail-car may pass in front of the microphone-array as close as only a few meters,[3] near-field considerations hold in the subsequent analysis. That is, the microphone array manifold depends implicitly on the sources' Cartesian coordinates in 3D space, or alternatively on both the DOA (azimuth angle & elevation angle) and the radial distance between any onboard noise-source and any microphone. However, these three geometric parameters (i.e., the x-, y-, and z-coordinate) are geometrically inter-dependent, given the (a priori known) spatial relationships between the rail-track and the microphone array in Figure 6.1.

---

[3]Given $2L^2/\lambda$ as the demarcation between the far field and the near field, the onboard noise-source are in the near-field of the microphone-array.

At time t, the microphone-array collects an $L \times 1$ vector-measurement,

$$
\begin{aligned}
\boldsymbol{\chi}(t) \;=\; & b_1(t)\mathbf{a}(x_{b_1}(t), y_{b_1}(t), z_{b_1}(t), f_1) + b_2(t)\mathbf{a}(x_{b_2}(t), y_{b_2}(t), z_{b_2}(t), f_2) + \\
& \sum_{i=1}^{I(t)} \int_{\{x_i(t), y_i(t), z_i(t)\}} [p_i(x_i(t), y_i(t), x_i(t), f, t)\mathbf{a}(x_i(t), y_i(t), z_i(t), f)]\, df\, dx_i(t) dy_i(t) dz_i(t) \\
& + \mathbf{n}(t)
\end{aligned}
\tag{6.1}
$$

where

$$
\mathbf{a}(x_i, y_i, z_i, f) \;=\; \left[1,\; e^{-j\frac{2\pi f}{c}(S_{i,2}-S_{i,1})},\; e^{-j\frac{2\pi f}{c}(S_{i,3}-S_{i,1})},\; \cdots,\; e^{-j\frac{2\pi f}{c}(S_{i,L}-S_{i,1})} \right]^{T} \tag{6.2}
$$

denotes the near-field steering-vector for a point-source impinging from $(x_i(t), y_i(t), z_i(t))$ as a pure-tone signal at frequency f and time t. Moreover, c denotes the speed of sound, and $S_{i,\ell} =$
$\sqrt{(x_i - x_\ell)^2 + (y_i - y_\ell)^2 + (z_i - z_\ell)^2}$ equals the distance from the ith source to the ℓth sensor locates at (x_ℓ, y_ℓ, z_ℓ), $\forall \ell = 1, 2, 3, \cdots, L$. Furthermore, $b_1(t)$ and $b_2(t)$ refer to the two beacons' pure-tone signals (with their frequencies a priori known to the microphone array), $\mathbf{a}(\cdot, \cdot, \cdot)$ represents the microphone-array's known array-manifold, $(x_{b_1}, y_{b_1}, z_{b_1})$ and $(x_{b_2}, y_{b_2}, z_{b_2})$ refer to coordinates of $b_1(t)$ and $b_2(t)$, respectively. Lastly, $\{x_i(t), y_i(t), z_i(t)\}$ refers to the unknown spatial spread of the ith onboard noise-source, $p_i(x_i(t), y_i(t), z_i(t), f, t)$ denotes the ith onboard noise-source's power at time t, and $\mathbf{n}(t)$ denotes an $L \times 1$ vector of unknown thermal noises.

The above measurement model can thus accommodate onboard noise-sources that are spatially spread, spatio-temporally non-stationary (in the stochastic sense), and/or on-and-off irregularly. Indeed, also possibly unknown is the total number $I(t)$ of such noise-sources at any time instant t.

6.2.2 Adaptive Localization of Beacons Aboard the Moving Rail-Car in the Microphone-Array's Near Field via Reference-Signal Beamforming

This proposed scheme needs first to track the rail-car, before localizing the onboard noise-sources with reference to the rail-car itself. This rail-car tracking is aided by two beacons, but no radar, no photo cell, and no video camera. The pure-tone beacons' frequencies are a priori known to the algorithm. The microphone-array can form two "reference-signal" beams [185], [179] to separately (but simultaneously) track each of the two beacons. For the beam that tracks the first beacon, that beam's spectrum would peak at the first beacon's instantaneous location $(x_{b_1}(t), y_{b_1}(t), z_{b_1}(t))$ (with respect to the microphone-array). This coordinate estimate $(\hat{x}_{b_1}(t), \hat{y}_{b_1}(t), \hat{z}_{b_1}(t))$ locates that beacon's instantaneous spatial location without any prior knowledge of the spatial geometry. The algorithmic details are presented below, using the first beacon as an example. Similar processing applies to the second beacon.

First, as each beacon's frequency is a priori known to the receiver, the out-of-band noises may be suppressed to improve the signal-to-noise ratio (SNR) at the beamformer

Table 6.1: Summary of the RLS Adaptation Steps

For each discrete-time index n, initialize the algorithm by setting $\mathbf{w}^{(b_1)}(n, 0) = \mathbf{0}$ and $\mathbf{P}(0) = \delta^{-1}\mathbf{I}$, where δ is a small positive constant. For the iteration-index $m = 1, 2, ...M$, do:

$$
\begin{aligned}
\boldsymbol{\pi}(m) &= \left[\boldsymbol{\chi}^{(b_1)}(n - M + m)\right]^H \mathbf{P}(m - 1) \\
\kappa(m) &= \gamma + \boldsymbol{\pi}(m)\boldsymbol{\chi}^{(b_1)}(n - M + m) \\
\mathbf{k}(m) &= \frac{\mathbf{P}(m - 1)\boldsymbol{\chi}^{(b_1)}(n - M + m)}{\kappa(m)} \\
\alpha(m) &= b(n - M + m) - \left[\mathbf{w}^{(b_1)}(n, m - 1)\right]^H \boldsymbol{\chi}^{(b_1)}(n - M + m) \\
\mathbf{w}^{(b_1)}(n, m) &= \mathbf{w}^{(b_1)}(n, m - 1) + \mathbf{k}(m)\alpha^*(m) \\
\mathbf{P}'(m - 1) &= \mathbf{k}(m)\boldsymbol{\pi}(m) \\
\mathbf{P}(m) &= \frac{1}{\gamma}\left[\mathbf{P}(m - 1) - \mathbf{P}'(m - 1)\right]
\end{aligned}
$$

After the above iteration, set $\mathbf{w}_{\text{opt}}^{(b_1)}(n) = \mathbf{w}^{(b_1)}(n, M)$.

---

input, by band-passing all microphones' received data $\boldsymbol{\chi}(t)$ individually at the first beacon's (a priori known) frequency f_1 to give $\boldsymbol{\chi}^{(b_1)}(t)$.

If the $L \times 1$ microphone-array data $\boldsymbol{\chi}^{(b_1)}(t)$ and the beacon's reference signal $b_1(t)$ **were** jointly stationary over time (in the stochastic sense), the $L \times 1$ reference-signal beamforming weight vector would equal:

$$
\begin{aligned}
\mathbf{w}_{\text{opt}}^{(b_1)} &= \arg \min_{\mathbf{w}} E\{|\mathbf{w}^H \boldsymbol{\chi}^{(b_1)}(t) - b_1(t)|^2\} \\
&= \left[\underbrace{E\left\{\boldsymbol{\chi}^{(b_1)}(t)\left(\boldsymbol{\chi}^{(b_1)}\right)^H(t)\right\}}_{\overset{\text{def}}{=}\mathbf{R}_{\boldsymbol{\chi}^{(b_1)},\boldsymbol{\chi}^{(b_1)}}}\right]^{-1} \underbrace{E\{\boldsymbol{\chi}^{(b_1)}(t)b_1(t)\}}_{\overset{\text{def}}{=}\mathbf{r}_{\boldsymbol{\chi}^{(b_1)},b_1}}
\end{aligned} \tag{6.3}
$$

where the superscript ^{H} denotes the Hermitian operator.

In reality, $\{\boldsymbol{\chi}^{(b_1)}(t), \boldsymbol{\chi}^{(b_2)}(t)\}$ and the onboard noise-source s' intensities $\{p_i(x_i(t), y_i(t), z_i(t), t), \forall i\}$ are jointly non-stationary in general. Moreover, $\mathbf{R}_{\boldsymbol{\chi}^{(b_1)},\boldsymbol{\chi}^{(b_1)}}$ and $\mathbf{r}_{\boldsymbol{\chi}^{(b_1)},b_1}$ are a priori *un*known. Hence, for any $t = nT_s$ (where T_s represents the time-sampling period), re-place (6.3) by:

$$
\mathbf{w}_{\text{opt}}^{(b_1,n)} = \left[\hat{\mathbf{R}}_{\boldsymbol{\chi}^{(b_1)},\boldsymbol{\chi}^{(b_1)}}(n)\right]^{-1} \hat{\mathbf{r}}_{\boldsymbol{\chi}^{(b_1)},b_1}(n) \tag{6.4}
$$

where

$$\hat{\mathbf{R}}_{\boldsymbol{\chi}^{(b_1)},\boldsymbol{\chi}^{(b_1)}}(n) = \left[(\mathbf{1}_L\boldsymbol{\gamma}) \odot \mathbf{X}^{(b_1)}(n)\right]\left(\mathbf{X}^{(b_1)}(n)\right)^H \quad (6.5)$$

$$\hat{\mathbf{r}}_{\boldsymbol{\chi}^{(b_1)},b_1}(n) = \left[(\mathbf{1}_L\boldsymbol{\gamma}) \odot \mathbf{X}^{(b_1)}(n)\right](\mathbf{b}_1(n))^H \quad (6.6)$$

$$\mathbf{X}^{(b_1)}(n) = \left[\boldsymbol{\chi}^{(b_1)}(n-M+1), \boldsymbol{\chi}^{(b_1)}(n-M+2), \ldots, \boldsymbol{\chi}^{(b_1)}(n)\right],$$

$$\mathbf{b}_1(n) = [b_1(n-M+1), b_1(n-M+2), \ldots, b_1(n)],$$

$$\boldsymbol{\gamma} = \left[\gamma^{M-1}, \gamma^{M-2}, \ldots, \gamma^0\right],$$

and M denotes window size of the processed data, $\odot$ signifies an element-by-element matrix-product, $\mathbf{1}_L$ symbolizes an $L \times 1$ vector of all ones, and $0 < \gamma \leq 1$ represents a "forgetting factor" to de-emphasize the more dated data. [4]

A computationally efficient method to update (6.5) and (6.6) for (6.4) is the "recursive least squares" (RLS) algorithm [61] and is summarized in Table 6.1. Other adaptive algorithms could be used in place of RLS, of course.

The beacon's location, at time $t = nT_s$, is estimated as:

$$(\hat{x}_{b_1}(n), \hat{y}_{b_1}(n), \hat{z}_{b_1}(n)) = \arg\max_{x,y,z} \underbrace{\left|\left(\mathbf{w}_{\text{opt}}^{(b_1)}(n)\right)^H \mathbf{a}(x, y, z, f_{b_1})\right|}_{=B^{(b_1)}(x,y,z,n)}, \quad (6.8)$$

Similarly, $(\hat{x}_{b_2}(n), \hat{y}_{b_2}(n), \hat{z}_{b_2}(n))$ may be computed.

---

[4]Occasionally, the data-correlation matrix $\hat{\mathbf{R}}_{\boldsymbol{\chi}^{(b_1)},\boldsymbol{\chi}^{(b_1)}}(n)$ could be ill-conditioned; and the matrix-inversion in (6.4) becomes numerically unstable. To alleviate this problem, set

$$\hat{\mathbf{R}}_{\boldsymbol{\chi}^{(b_1)},\boldsymbol{\chi}^{(b_1)}}(n) = \mathbf{I}, \qquad \forall n, \qquad (6.7)$$

instead of using (6.5). The resulting beamformer can be shown to be equivalent to that obtained using (6.5) for noiseless data.

6.3 The Proposed Algorithmic Step #2: Localization of Noise-Sources w.r.t. the Moving Rail-Car's Carriage

The two beacons' above-estimated locations help to locate the rail-car. Spatial match-filtering (i.e., delay-and-sum beamforming) will next scan the rail-car's three-dimensional space to locate any onboard acoustic noise-source. The location-power-spectrum is defined as:

$$
P_f(x, y, z) = \frac{1}{M} \sum_{m=n-M+1}^{n} \left| \mathbf{a}^H\left(\hat{x}_{b_1}(n) + x, \hat{y}_{b_1}(n) + y, \hat{z}_{b_1}(n) + z, f\right) \underbrace{\gamma^{n-m}\bar{\boldsymbol{\chi}}(m)}_{\text{weighted data}} \right|^2 \quad (6.9)
$$

where $\{\bar{\boldsymbol{\chi}}(m)\}$ is obtained by notch-filtering $\{\boldsymbol{\chi}(m)\}$, with notches at the (a priori known) frequencies f_{b_1} and f_{b_2} to suppress the two beacons.

As the array-manifold $\mathbf{a}(\cdot, \cdot, \cdot, f)$ is a function of frequency, the location-power-spectrum in (6.9) depends on the scanning-frequency. Hence, the above electronic scanning spectrum is frequency-specific. As the noise-sources could be spectrally colored, the scanning needs to be performed over many frequency-bins and then summed to give the composite spectrum,

$$
P_{\text{rms}}(x, y, z) = \sqrt{\frac{1}{J} \sum_{j=1}^{J} \left[\frac{P_{f_j}(x, y, z)}{\left| \max\limits_{\forall x, y, z} \{P_{f_j}(x, y, z)\} \right|} \right]^2} \quad (6.10)
$$

The amplitude-normalization in (6.10) aims to avoid domination of the composite spectrum by any single scanning-frequency's spectrum.

6.4 Validation of the Proposed Scheme by Monte Carlo Simulations

The track-side array consists of 10×10 identical isotropic microphones, placed on a vertical rectangular grid, of horizontal non-uniform grid-spacings $[0.5, 2.5, 3.5, 2.5, 2, 1.5, 2.5, 2, 3]\lambda$ and vertical non-uniform grid-spacings $[1.5, 2, 3, 0.5, 2.5, 2.5, 2, 4, 2]\lambda$, with $\lambda = 0.115$ meter (i.e., the wavelength of the 3kHz beacon). The rail-car travels at 40 km/h (i.e., 11 meters/second) along a straight rail-track, making an $\alpha = 15°$ angle with the microphone-array's horizontal axis. This rail-car's length, width, and height are respectively 23 meters, 3 meters, and 4.8 meters. Two beacons, placed at two corners of the rail-car, have the Cartesian coordinates of $(-4.2, -5.5, 0.8)$ and $(-7.2, 17.5, 5.6)$, at time-sample $n = 1$. (See Figure 6.1.) The corresponding beacon-tones are at 3kHz (with a wavelength of 0.115 meter) and 2kHz, of unity power, and with statistically independent initial temporal phases (randomly distributed over $[0, 2\pi)$) across Monte Carlo trials. Two noise-sources are aboard the rail-car carriage, at $(-6.2, 2.7, 2.4)$ and $(-4.8, 12.1, 3.3)$, at time-sample $n = 1$. The additive thermal noise is zero-mean, spatio-temporally white, Gaussian, with a total power equal to $\frac{1}{100}$ of each onboard noise-source's power.
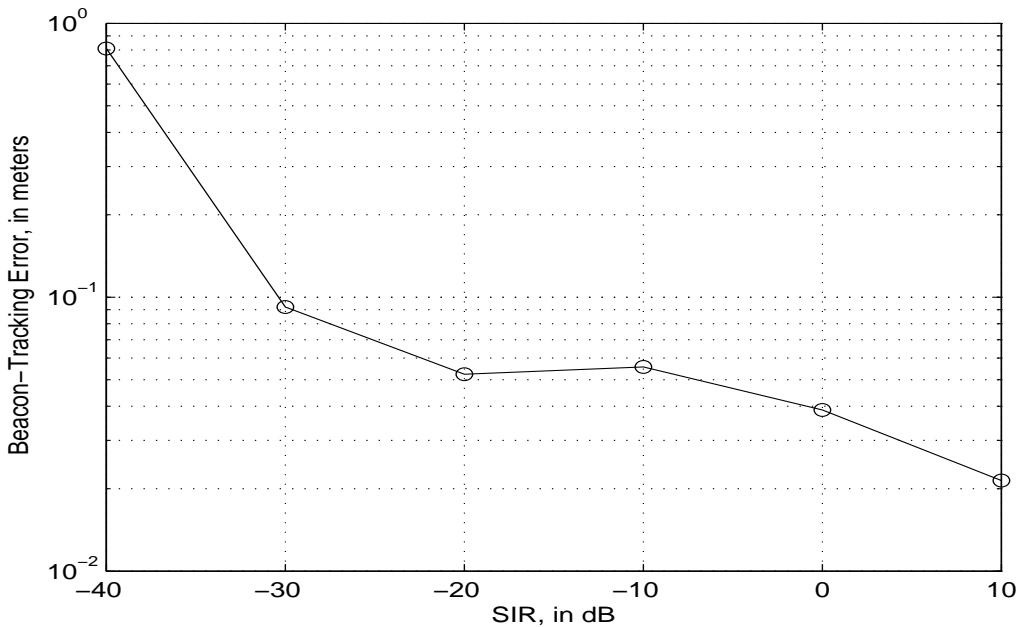
Figure 6.2: Beacon-tracking error in the algorithm's step #1.

Figure 6.2 demonstrates the performance of the proposed beacon-localization step of Section 6.2 in tracking the first beacon. The performance metric is defined as

$$d_e(n) = \sqrt{[x_{b_1}(600) - \hat{x}_{b_1}(600)]^2 + [y_{b_1}(600) - \hat{y}_{b_1}(600)]^2 + [z_{b_1}(600) - \hat{z}_{b_1}(600)]^2} \quad (6.11)$$

Figure 6.2's SIR considers the first beacon as the signal, but all onboard noise-sources plus thermal noise as interference. The results in Figure 6.2 are obtain without bandpass-filtering around the beacon for SIR-enhancement. Each data-point therein is averaged
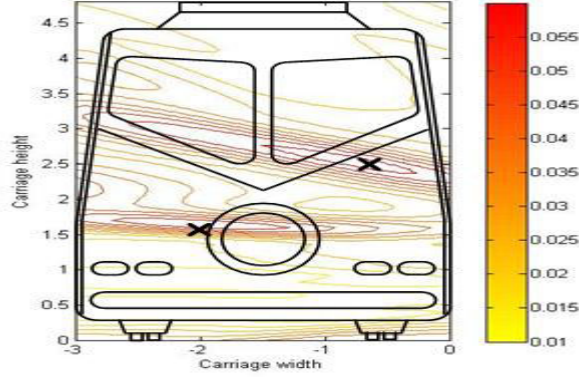
Figure 6.3: The power-contour map along the rail-car's cross-section, with SIR $= -10$dB, $n = 600$, $M = 30$, and $\gamma = 1$.
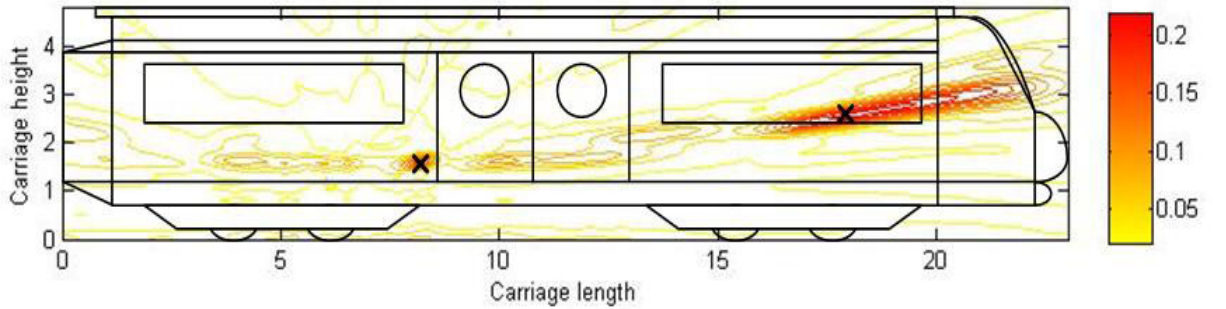
Figure 6.4: The power-contour map along the rail-car's length from the side, with SIR $= -10$dB, $n = 600$, $M = 30$, and $\gamma = 1$.

from 20 independent Monte Carlo trials. For the present scenario, Figure 6.2 suggests that the proposed algorithm can track the rail-car to within 10cm for an SIR as low as -30 dB – allowing the proposed scheme to operate with inaudible beacons.

Figure 6.3 and 6.4 map the rail-car, cross-sectionally and longitudinally,[5] in power-scan contours, averaged from 20 independent Monte Carlo trials, at time-sample $n = 600$, under SIR = -10 dB. These power-scans are for the single scanning-frequency of f_{b_1}, without any notch-filter pre-processing[6] nor any spectral averaging of (6.10).[7] The black "x" icons, on these power-scan maps, locate the two onboard noise-sources' actual positions of
$(x_1(n = 600), y_1(n = 600), z_1(n = 600)) = (-2, 8.2, 1.6) + (x_{b_1}(n = 600), y_{b_1}(n = 600), z_{b_1}(n = 600))$,
$(x_2(n = 600), y_2(n = 600), z_2(n = 600)) = (-0.6, 17.6, 2.5) + (x_{b_2}(n = 600), y_{b_2}(n = 600), z_{b_2}(n = 600))$.
The proposed scanning algorithm here locates the two onboard noise-sources to roughly coincide with the power-contour's peaks.

---

[5]The cross-sectional map in Figure 6.3 is averaged from 100 longitudinal cuts, evenly spaced along the length of the rail-car. The longitudinal map in Figure 6.4 is averaged from 100 cross-sectional cuts, evenly spaced along the width of the rail-car.

[6]Hence, $\chi(m)$ substitutes for $\bar{\chi}(m)$ in (6.9).

[7]The f_{b_1} beacon is too weak to show up in the power-contour maps. The f_{b_2} beacon does not appear, because the scanning-frequency is f_{b_1}.

6.5 Validation of the Proposed Scheme by Anechoic Chamber Experiments

Figure 6.5: The model rail-car (for anechoic-chamber testing) mounts several loud-speakers (as beacons or onboard noise-sources) on a 1.1-meter long steel bar. The inter-loud-speaker spacing is identical. Each loudspeaker is 25mm in diameter and is driven by a voice coil. The microphone-array (for anechoic-chamber testing) has 12 identical microphones: Bruel & Kjaer Type 4935. The inter-microphone spacings in mm: 145.05, 124.88, 134.94, 151.96, 30, 115.05, 83.33, 41.54, 134.94, 181.96, and 198.38.

Anechoic chamber experiments, deploying a model-train, further verify the proposed algorithm's efficacy. Most acoustic reflections would be absorbed by the walls, the roof, and the floor of the anechoic chamber, which thus constituted a free-field propagation-environment to mimic a controlled outdoor environment.

Figure 6.5 is a photograph of the equipments set up in the anechoic chamber. There, a 1.1-meter long model-train had two beacons, $b_1(t)$ and $b_2(t)$, were pure-tones at 1 kHz and 0.5 kHz, at respective positions of 0 and 1.1 meters along the length of the model-train and with respective intensities of 55dB and 66dB. MAC iPods fed independent white Gaussian noises of 56dB intensity, to two loudspeakers at positions 0.37 and 0.73 meters along the model-train's length, to mimic onboard noise-sources. This model-train was manually string-pulled along a 4.7 meter wooden track, with a variable speed roughly 0.085 to 0.17 meter per second.[8] In parallel to, and 1.1 meters away from, the rail-track was a linear array of twelve identical, but non-uniformly spaced, microphones. The onboard sources

---

[8]This would scale to about 8 to 15 km per hour, as the model-train constitutes a $\frac{1}{24}$ scale-down model of an actual carriage of 23 to 25 meters long.

can thus be located only along the carriage's length (but not along its height nor along its width) by this one-dimensional array. This above-described track/array geometry was a priori known to the algorithm. Each microphone's measurement was sampled at 65.536 kHz. There were $M = 1000$ time-samples; and $n = 1049575$. The Bruel & Kjaer Type 3560D frequency-analyzer was used.
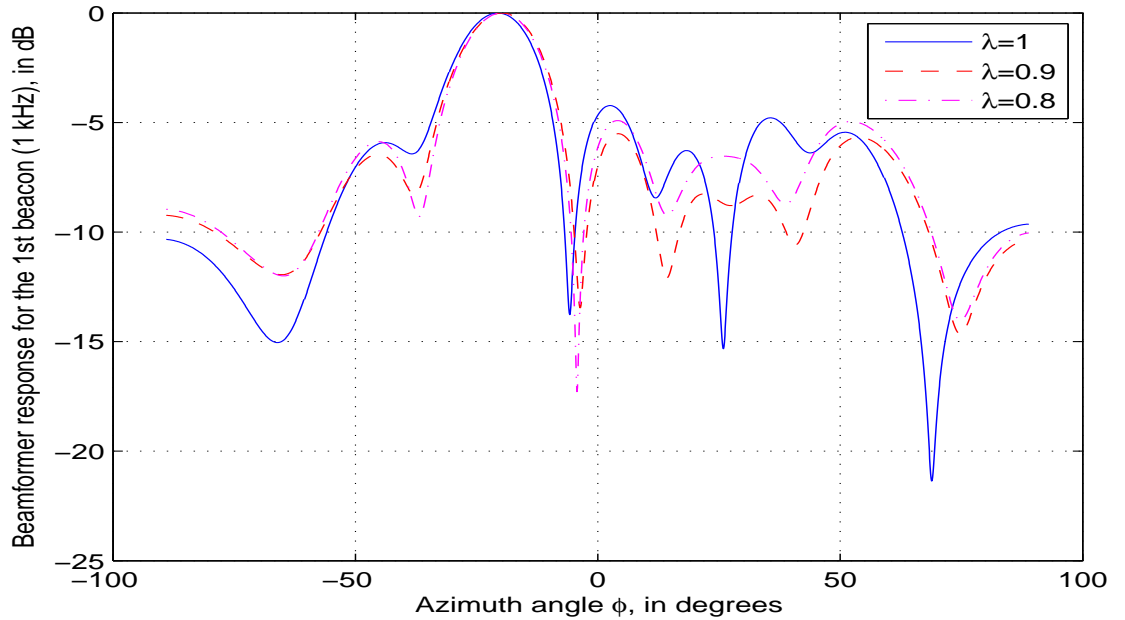
Figure 6.6: For algorithmic step #1: The beacon-tracking azimuth-spectrum $B^{(b_1)}(\cdot, \cdot, \cdot, n = 1049575)$ from anechoic chamber data.
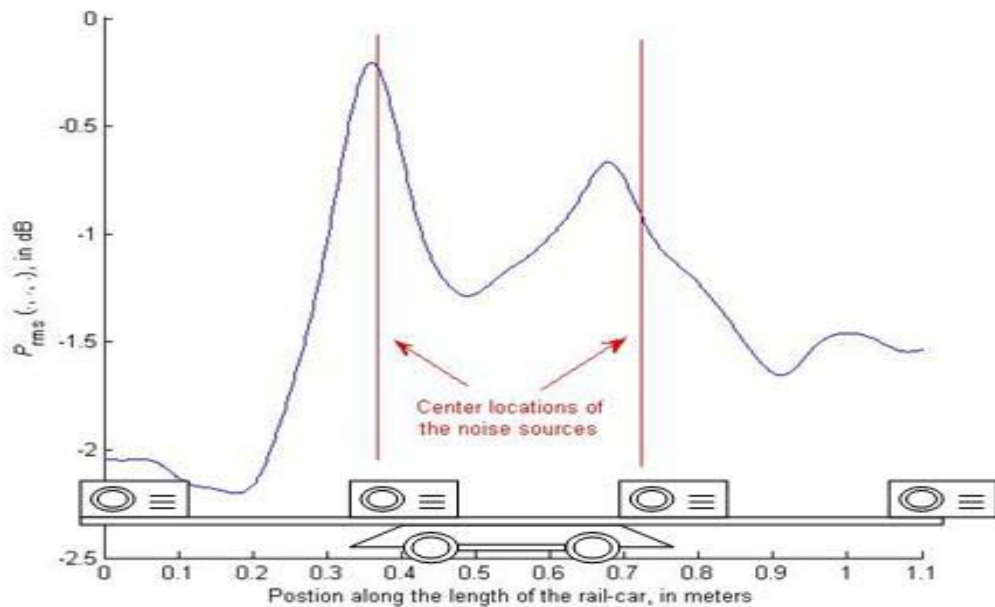
Figure 6.7: For algorithmic step #2: The carriage-scanning composite spectrum $P_{\text{rms}}(\cdot, \cdot, \cdot)$ (amplitude-normalized to give a unit-height peak) from anechoic chamber data.

Recall that the earlier developed algorithm presumes complex-value for the microphones data in (6.1). Actual measurements ($\boldsymbol{\chi}^{(\mathrm{re})}(t)$) are, of course, real-value. Hence, the Hilbert Transform is used to convert the measured data to their equivalent complex-value analytical signals $\boldsymbol{\chi}(t) = \boldsymbol{\chi}^{(\mathrm{re})}(t) + \boldsymbol{\chi}^{(\mathrm{im})}(t)$. Specifically, the ℓth-element $[\boldsymbol{\chi}(t)]_\ell$ of $\boldsymbol{\chi}(t)$ is obtained as:

$$[\boldsymbol{\chi}^{(\mathrm{im})}(t)]_\ell \quad = \quad \frac{1}{\pi} \int_{-\infty}^{+\infty} \frac{[\boldsymbol{\chi}^{(\mathrm{re})}(\tau)]_\ell}{t - \tau} d\tau \tag{6.12}$$

For the beacon *tracking* step: Figure 6.6 verifies the efficacy of the beacon-tracking algorithm, computing the beamformer weights via (6.7), at various values of the forgetting factor λ, with the azimuth-angle respectively estimated as $-20.6°$, $-19.7°$, $-19.8°$. [9]

For the rail-car *scanning* step: Figure 6.7 shows the composite azimuth-spectrum, formed from $J = 10$ different scanning-frequencies, evenly distributed from 0.5kHz to 5kHz. There in Figure 6.7, the two red solid lines mark the two noise-sources' true locations onboard the toy-car. A forgetting factor of $\gamma = 1$ was used. The proposed scheme can roughly locate the two onboard noise-sources here to within about a foot.

6.6   Summary

Herein proposed is a new method to localize noise-sources onboard a rail-car, passing along rail-track with a prior unknown speed. No auxiliary apparatus, besides two onboard beacons, is needed to synchronize the trackside microphone-array's data with the rail-car's movements. Three-dimensional source-localization is thereby made possible even with no prior knowledge of the spatial geometry between the roadside microphone-array and the rail-track, according to limited Monte Carlo simulations. Limited anechoic chamber testing verifies the proposed scheme's efficacy for one-dimensional source-localization.

---

[9]The mobile rail-car's true azimuth-angle at any particular time-instant has not be exactly determined, partly because the rail-car was hand pulled. However, this would not hinder the localization of the onboard noise-sources with reference to the rail-car frame.

Chapter 7

Conclusion

In Chapter 2, we thoroughly assessed geometric models in terms of their DOA-distributions against all empirical data available from the open literature.

In Chapter 3, a new geometric model for the uplink/downlink multipahs' TOA-distribution is proposed. The proposed TOA-model can better fit certain empirical data than can customary geometric models can.

In chapter 4, we pioneer the AVS near-field measurement-model, based on rigorous acoustic physics. Section 4.1 to 4.3 derive the near-field model, with no boundary near the acoustic vector-sensor. The closed-form CRB is derived and analyzed. Section 4.4 extends the measurement model to allow the boundary case.

In chapter 5, we propose a new algorithm to geolocate a source in 3D near-field space, using only one spatially spread acoustic vector-sensor. This algorithm requires no prior knowledge of the temporal structure of the impinging signal, nor any iterative solution. However, this method can allow only one incident source with constant emitting power - a limitation common to basically all "received signal Strength Indication" (RSSI) methods of geolocation.

A new adaptive "beamforming" signal-processing algorithm is developed in chapter 6 to locate noise-sources aboard a rail-car that passes by a track-side immobile microphone-array. This proposed microphone-array beamformer tracks the rail-car's spatial movement, with the aid of two inaudible acoustic beacons placed abroad the rail-car. The proposed scheme then localizes the noise-sources with reference to the rail-car's coordinates. No auxiliary infrastructure (e.g., no radar nor video-camera) is needed besides the onboard beacons. Monte Carlo simulations and anechoic chamber experiments verify the proposed scheme's efficacy.

Some future work may be conducted, such as

(1) In Chapter 2 and 3, to further study the landmobile channel model, some new geometric models which can more efficiently describe the empirical data in the open literature could be proposed.

(2) In Chapter 4 and 5, the near-field source location problem using acoustic vector-sensor, can be further investigated with the presence of different type of reflection

boundary. Such as how would different material of the reflection boundary can affect the source localization accuracy.

(3) In Chapter 6, we study the sound source location onboard a moving train. However, only lab test was conducted to verify the efficacy of the algorithm. In the future, a field test may take place, with the cooperation from H.K. MTR, to further apply our algorithm in practice.

Bibliography

[1] A. Abdi, H. Guo & P. Sutthiwan, "A New Vector Sensor Receiver for Underwater Acoustic Communication," *IEEE Oceans Conference*, 2007.

[2] A. M. Ali, K. Yao, T. C. Collier, C. E. Taylor, D. T. Blumstein & L. Girod, "An Empirical Study of Collaborative Acoustic Source Localization," *International Conference on Information Processing in Sensor Networks*, pp. 41-50, 2007.

[3] A. Andrade & D. Covarrubias, "Radio Channel Spatial Propagation Model for Mobile 3G in Smart Antenna System," *IEICE Transactions on Communications*, vol. E86-B, no. 1, pp. 213-220, January 2003.

[4] D. Anzai & S. Hara, "Experimental Evaluation of a Simple Outlier RSSI Data Rejection Algorithm for Localization Estimation in Wireless Sensor Networks," *IEICE Transactions on Communications*, vol. E91-B, no. 11, pp. 3442-3449, November 2008.

[5] M. R. Arias & B. Mandersson, "Time Domain Cluster PDF and Its Application in Geometry Based Statistical Channel Models," *IEEE International Symposium on Personal, Indoor and Mobile Radio Communications*, 2007.

[6] K. P. Arunkumar & G. V. Anand, "Multiple Source Localization in Shallow Ocean using a Uniform Linear Horizontal Array of Acoustic Vector Sensors," *IEEE Region 10 Conference*, 2007.

[7] K. P. Arunkumar & G. V. Anand, "Source Localisation in Shallow Ocean using a Vertical Array of Acoustic Vector Sensors," *European Signal Processing Conference*, 2007.

[8] K. Attenborough, "Sound Propagation Close To The Ground," *Annu. Rev. Fluid Mech.*, 2002.

[9] B. Barsikow, W.F. King III & E. Pfizenmaier, "Wheel/Rail Noise Generated by a High-Speed Train Investigated with a Line Array of Microphones," *Journal of Sound & Vibration*, no. 118, pp. 99-122, October 1987.

[10] B. Barsikow, & W. F. King III, "On Removing the Doppler Frequency Shift from Array Measurements of Railway Noise," *Journal of Sound & Vibration*, no. 120, pp. 190-196, January 1988.

[11] B. Barsikow, "Experiences with Various Configurations of Microphone Arrays Used to Locate Sound Sources on Railway Trains Operated by the DB AG," *Journal of Sound & Vibration*, no. 193, no. 1, pp. 283-293, May 1996.

[12] M. D. Batariere, T. K. Blankenship & J. F. Kepler, "Wideband MIMO Mobile Impulse Response Measurements at 3.7 GHz," *IEEE Vehicular Technology Conference*, vol. 1, pp. 26-30, Spring 2002.

[13] M. R. Benjamin, D. Battle, D. Eickstedt, H. Schmidt & A. Balasuriya, "Autonomous Control of an Autonomous Underwater Vehicle Towing a Vector Sensor Array," *IEEE International Conference on Robotics and Automation*, pp. 4562-4569, 2007.

[14] M. J. Berliner & J. F. Lindberg, *Acoustical Particle Velocity Sensors: Design, Performance and Applications*, Woodbury, New York, U.S.A.: AIP Press, 1996.

[15] D. D. N. Bevan, V. T. Ermolayev, A. G. Flaksman & I. M. Averin, "Gaussian Channel Model for Mobile Multipath Environment," *EURASIP Journal on Applied Signal Processing*, vol. 2004, no. 9, pp. 1321-1329, 2004.

[16] J. J. Blanz, A. Klein & W. Mohr, "Measurement-based Parameter Adaptation of Wideband Spatial Mobile Radio Channel Models," *IEEE Symposium on Spread Spectrum Techniques and Applications*, vol. 1, pp. 22-25, 1996.

[17] N. Blaunstein & E. Tsalolihin, "Signal Distribution in the Azimuth, Elevation, and Time-Delay Domains in Urban Radio Commnicatio Links," *IEEE Antennas & Propagation Magazine*, vol. 46, no. 5, pp. 171-178, October 2004.

[18] J. Blumenthal, R. Grossmann, F. Golatowski & D. Timmermann, "Weighted Centroid Localization in Zigbee-based Sensor Networks," *IEEE International Symposium on Intelligent Signal Processing*, pp. 1-6, 2007.

[19] R. Blumrich & J. Altmann, "Medium-range Localisation of Aircraft via Triangulation," *Applied Acoustics*, vol. 61, no. 1, pp. 65-82, September 2000. New York, U.S.A.: AIP Press, 1996.

[20] F. Bohagen, P. Orten & G. E. Oien, "Design of Optimal High-Rank Line-of-Sight MIMO Channels," *IEEE Transactions on Wireless Communications*, vol. 6, no. 4, pp. 1420-1425, April 2007.

[21] S. Bruhl & K. P. Schmitz, "Noise Source Localization on High Speed Trains Using Different Array Types," *Inter-Noise Conference*, Leuven, Belgium, pp. 1311-1314, 1993.

[22] S. Bruhl & A. Roder, "Acoustic Noise Source Modelling Based on Microphone Array Measurements," *Journal of Sound & Vibration*, no. 231, pp. 611-617, March 2000.

[23] G. C. Chen & W. S. Hodgkiss, "VLF Source Localization with a Freely Drifting Acoustic Sensor Array," *IEEE Journal of Oceanic Engineering*, vol. 18, no. 3, pp. 209-223, July 1993.

[24] T.-A. Chen, M. P. Fitz, W.-Y. Kuo & M. D. Zoltowski, "A Space-Time Model for Frequency Nonselective Rayleigh Fading Channels with Applications to Space-Time Modems," *IEEE Journal on Selected Areas in Communications*, vol. 18, no. 7, pp. 1175-1190, July 2000.

[25] J. Zhao, H. Chen & J. Li, "Two-Dimensional Direction Finding for Low-Attitude Targets Based on Intensity Measurement Using an Acoustics Vector Sensor," *Acta Acustica*, vol. 29, no. 3, pp. 277-283, May 2004.

[26] H.-W. Chen & J.-W. Zhao, "Wideband MVDR Beamforming for Acoustic Vector Sensor Linear Array," *IEE Proceedings – Radar, Sonar & Navigation*, vol. 151, no. 3, pp. 158-162, June 2004.

[27] H.-W. Chen & J. Zhao, "Coherent Signal-Subspace Processing of Acoustic Vector Sensor Array for DOA Estimation of Wideband Sources," *Signal Processing*, vol. 85, pp. 837-847, April 2005.

[28] C.-E. Chen, A. M. Ali & H. Wang, "Design and Testing of Robust Acoustic Arrays for Localization and Enhancement of Several Bird Sources," *International Conference on Information Processing in Sensor Networks*, 2006.

[29] S. Choi, C. R. Berger, S. Zhou, & P. Willett, "Estimation of Target Trajectories Based on Distributed Channel Energy Measurements," *IEEE International Conference on Information Fusion*, pp. 1-6, 2008.

[30] H. C. Chu & R. H. Jan, "A GPS-less, Outdoor, Self-positioning Method for Wireless Sensor Networks," *Ad Hoc Networks*, vol. 5, pp. 547-557, July 2007.

[31] J. A. Clark & G. Tarasek, "Localization of Radiating Sources along the Hull of a Submarine Using a Vector Sensor Array," *IEEE Oceans Conference*, 2006.

[32] H. Cox, "Super-Directivity Revisited," *IEEE Instrumentation & Measurement Technology Conference*, pp. 87-90, 2004.

[33] H. Cox & H. Lai, "Endfire Supergain with a Uniform Line Array of Pressure and Velocity Sensors," *Asilomar Conference on Signals, Systems and Computers*, pp. 2271-2275, 2006.

[34] P. J. Cullen, P. C. Fannin & A. Molina, "Wide-Band Measurement and Analysis Techniques for the Mobile Radio Channel," *IEEE Transactions on Vehicular Technology*, vol. 42, no. 4, pp. 589-603, November 1993.

[35] H.-E. de Bree, W. F. Druyvesteyn, E. Berenschot & M. Elwenspoek, "Three-Dimension Sound Intensity Measurements Using Microflown Particle Velocity Sensors," *IEEE International Conference on Electro Mechanical Systems*, pp. 124-129, 1999.

[36] Y. L. C. de Jong & M. H. A. J. Herben, "High-Resolution Angle-of-Arrival Measurement of the Mobile Radio Channel," *IEEE Transactions on Antennas and Propagation*, vol. 47, pp. 1677-1687, November 1999.

[37] Y. L. C. de Jong & M. H. A. J. Herben, "Experimental Verification of Ray-Tracing Based Propagation Prediction Models for Urban Microcell Environments," *IEEE Vehicular Technology Conference*, pp. 1434-1438, Fall 1999.

[38] Y. L. C. de Jong, M. H. A. J. Herben & A. Mawira, "Transmission of UHF Radiowaves through Buildings in Urban Microcell Environments," *Electronics Letters*, vol. 35, no. 9, pp. 743-745, 29th April 1999.

[39] F. Desharnals & G. L. D'Spain, "Acoustic Intensity Measurements with Swallow Floats," *Canadian Acoustics*, vol. 22, part 3, pp. 159-160, September 1994.

[40] M. G. Dittrich & M. H. A. Janssens, "Improved Measurement Methods for Railway Rolling Noise," *Journal of Sound & Vibration*, no. 231, pp. 595-609, March 2000.

[41] G. L. D'Spain, W. S. Hodgkiss & G. L. Edmonds, "Energetics of the Deep Ocean's Infrasonic Sound Field," *Journal of the Acoustical Society of America*, vol. 89, no. 3, pp. 1134-1158, March 1991.

[42] G. L. D'Spain, W. S. Hodgkiss & G. L. Edmonds, "The Simultaneous Measurement of Infrasonic Acoustic Particle Velocity and Acoustic Pressure in the Ocean by Freely Drifting Swallow Floats," *IEEE Journal of Oceanic Engineering*, vol. 16, no. 1, pp. 195-207, April 1991.

[43] G. L. D'Spain, W. S. Hodgkiss, G. L. Edmonds, J. C. Nickles, F. H. Fisher & R. A. Harriss, "Initial Analysis of The Data From The Vertical DIFAR Array," *IEEE Oceans Conference*, vol. 1, pp. 346-351, 1992.

[44] G. L. D'Spain, "Relationship of Underwater Acoustic Intensity Measurements to Beamforming," *Canadian Acoustics*, vol. 22, part 3, pp. 157-158, September 1994.

[45] P. C. F. Eggers, "Generation of Base Station DOA Distribution by Jacobi Transformation of Scattering Areas," *Electronics Letters*, vol. 34, no. 1, pp. 24-26, January 8, 1998.

[46] P. Eggers, I. Kovacs, K. Djama, J. B. Andersen & K. Olesen, "Assessment of UMTS Up/Down-Link Channel Balance in Adaptive BS Antenna Systems," *IEEE Vehicular Technology Conference*, vol. 1, pp. 82-86, Fall 2002.

[47] R. B. Ertel, P. Cardieri, K. W. Sowerby, T. S. Rappaport & J. H. Reed, "Overview of Spatial Channel Models for Antenna Array Communication Systems," *IEEE Personal Communications*, vol. 5, no. 1, pp. 10-22, February 1998.

[48] R. B. Ertel & J. H. Reed, "Angle and Time of Arrival Statistics for Circular and Elliptical Scattering Models," *IEEE Journal on Selected Areas in Communications*, vol. 17, no. 11, pp. 1829-1840, November 1999.

[49] J. Y. Fang, H. C. Chu, R. H. Jan & W. Yang, "A Multiple Power-level Approach for Wireless Sensor Network Positioning," *Computer Networks*, vol. 52, pp. 3101-3118, December 2008.

[50] F. Haihong, L. Guolong & H. Junying, "The Direction Estimation Using Combined Sensor with Pressure and Particle Velocity," *Acta Acustica*, vol. 25, no. 6, November 2000.

[51] B. H. Fleury, M. Tschudin, R. Heddergott, D. Dahlhaus & K. I. Pedersen, "Channel Parameter Estimation in Mobile Radio Environments Using the SAGE Algorithm," *IEEE Journal on Selected Areas in Communications*, vol. 17, no. 3, pp. 434-450, March 1999.

[52] J. Fuchs & H. Chuberre, "A Deconvolution Approach to Source Localization," *IEEE Signal Processing Transaction*, vol. 42, no. 6, pp. 1462-1470, June 1994.

[53] A. Giorgetti, M. Chiani, M. Shafi & P. J. Smith, "Level Crossing Rates and MIMO Capacity Fades: Impacts of Spatial/Temporal Channel Correlation," *International Conference on Communications*, vol. 5, pp. 3046-3050, 2003.

[54] L. Guanfang, Z. Anbang, H. Junying & S. Guocang, "The Application of Empirical Mode Decomposition in Target-starting Sound Detection," *IEEE Vehicle Power and Propulsion Conference*, 2008.

[55] S. Guiqing, Y. Desen, J. Lanyue & S. Shengguo, "Maximum Likelihood Ratio Detection and Maximum Likelihood DOA Estimation Based on the Vector Hydrophone," *Acta Acustica*, vol. 28, no. 1, January 2003.

[56] S. Guiqing & L. Qihu, "Acoustic Vector Sensor Signal Processing," *Acta Acustica*, vol. 29, no. 6, November 2004.

[57] C. H. Hansen, *Noise Control : From Concept to Application*, London, U.K. : Taylor & Francis, 2005.

[58] M. Hawkes & A. Nehorai, "Acoustic Vector-Sensor Beamforming and Capon Direction Estimation," *IEEE Transactions on Signal Processing*, vol. 46, no. 9, pp. 2291-2304, September 1998.

[59] M. Hawkes & A. Nehorai, "Acoustic Vector-Sensor Processing in the Presence of a Reflecting Boundary," *IEEE Transactions on Signal Processing*, vol. 48, no. 11, pp. 2981-2993, November 2000.

[60] M. Hawkes & A. Nehorai, "Wideband Source Localization Using a Distributed Acoustic Vector-Sensor Array," *IEEE Transactions on Signal Processing* vol. 51, no. 6, pp. 1479-1491, June 2003.

[61] S. Haykin, *Adaptive Filter Theory*, 2nd edtion, U.S.A.: Prentice-Hall, 1991.

[62] J. He, S. Jiang, J. Wang & Z. Liu, "Direction Finding in Spatially Correlated Noise Fields with Arbitrarily-Spaced and Far-Separated Subarrays at Unknown Locations," *IET Radar, Sonar & Navigation*, vol. 3, no. 3, pp. 278-284, June 2009.

[63] B. Hochwald & A. Nehorai, "Identifiability in Array Processing Models with Vector-Sensor Applications," *IEEE Transactions on Signal Processing*, vol. 44, no. 1, pp. 83-95, January 1996.

[64] G. Holzl, "Low Noise Goods Wagons," *Journal of Sound & Vibration*, no. 193, pp. 359-366, May 1996.

[65] V. J. Hughes, J. G. Boulton, J. M. Coles, T. R Empson and N. J. Kerry, "Why an Optically-Based Hydrophone Works Better," *Sensor Review*, vol. 7, no. 3, pp. 123-126, July 1987.

[66] J. Hui, H. Liu, M. Fan & G. Liang, "Study on the Physical Basis of Pressure and Particle Velocity Combine Processing," *Chinese Journal of Acoustics*, vol. 20, no. 3, pp. 203-212, 2001.

[67] R. Janaswamy, "Angle and Time of Arrival Statistics for the Gaussian Scatter Density Model," *IEEE Transactions on Wireless Communications*, vol. 1, no. 3, pp. 488-497, July 2002.

[68] L. Jiang & S. Y. Tan, "Simple geometrical-based AOA model for mobile communication systems," *Electronics Letters*, vol. 40, no. 19, pp. 1203-1205, September 2004.

[69] L. Jiang & S. Y. Tan, "Geometrical-Based Propagation Model for Mobile Communication Systems," *International Conference on Microwave and Millimeter Wave Technology*, pp. 834-837, 2004.

[70] L. Jiang & S. Y. Tan, "Geometrically-Based Channel Model for Mobile-Communication Systems," *Microwave and Optical Technology Letters*, vol. 45, no. 6, pp. 522-527, June 2005.

[71] M. A. Josserand & C. Maerfeld, "PVF2 Velocity Hydrophone," *Journal of the Acoustical Society of America*, vol. 78, no. 3, pp. 860-867, 1985.

[72] M. Kalivodaa, U. Danneskiold-Samseb, F. Krugerc & B. Barsikow, "EU Rail Noise: a Study of European Priorities and Strategies for Railway Noise Abatement" *Journal of Sound & Vibration*, no. 267, part 3, pp. 387-396, October 2003.

[73] M. Kalivodaa, M. Kudrnaa & G. Presle, "Application of MetaRail Railway Noise Measurement Methodology: Comparison of Three Track Systems," *Journal of Sound & Vibration*, no. 267, pp. 701-707, October 2003.

[74] K. Kalliola & P. Vainikainen, "Characterization System for Radio Channel of Adaptive Array Antennas," *IEEE International Symposium on Personal, Indoor & Mobile Radio Communications*, vol. 1, pp. 95-99, 1997.

[75] L. M. Kaplan, T. Damarla & T. Pham, "QoI for Passive Acoustic Gunfire Localization," *IEEE International Conference on Mobile Ad Hoc and Sensor Systems*, pp. 754-759, 2008.

[76] A. Kavak, W. Yang & G. Xu, "Characterization of Fast Fading Wireless Vector Channels," *Asilomar Conference*, vol. 1, pp. 780-784, 1998.

[77] S. M. Kay, Fundamentals of Statistical Signal Processing: Estimation Theory. Upper Saddle River, NJ: Prentice-Hall, 1993.

[78] N. M. Khan, M. T. Simsim & P. B. Rapajic, "A Generalized Model for the Spatial Characteristics of the Cellular Mobile Channel," *IEEE Transactions on Vehicular Technology*, vol. 57, no. 1, pp. 22-37, January 2008.

[79] W. F. King III, "On the Role of Aerodynamically Generated Sound in Determining Wayside Noise Levels from High Speed Trains," *Journal of Sound & Vibration*, no. 54, part 3, pp. 361-378, October 1977.

[80] W. F. King III & D. Bechert, "On the Sources of Wayside Noise Generated by High-Speed Trains," *Journal of Sound & Vibration*, no. 66, pp. 311-332, October 1979.

[81] T. Kitagawa & D.J. Tohmpson, "Comparison of Wheel/Rail Noise Radiation on Japanese Railways Using the TWINS Model and Microphone Array Measurement," *Journal of Sound & Vibration*, no. 293, pp. 496-509, June 2006.

[82] A. Klein & W. Mohr, "A Statistical Wideband Mobile Radio Channel Model Including the Directions-of-Arrival," *IEEE International Symposium Spread Spectrum Technology and Applications* vol. 1, pp. 102-106, 1996.

[83] C. Kloch, G. Liang, J. B. Andersen, G. F. Pedersen & H. L. Bertoni, "Comparison of measured and Predicted Time Dispersion and Direction of Arrival for Multipath in a Small Cell Environment," *IEEE Transactions on Antennas & Propagation*, vol. 49, no. 9, pp. 1254-1263, September 2001.

[84] T. B. Koay, P. J. Seeking, M. Chitre, S. P. Tan & M. Hoffmann-Kuhnt, "Advanced PANDA for High Speed Autonomous Ambient Noise Data Collection and Boat Tracking - System and Results," *IEEE Oceans Conference - Asia Pacific*, 2006.

[85] A. Kuchar, M. Taferner, M. Tangemann & C. Hoek, "Field Trial with GSM/DCS1800 Smart Antenna Base Station," *IEEE Vehicular Technology Conference*, vol. 1, pp. 42-46, Fall 1999.

[86] A. Kuchar, J. P. Rossi & E. Bonek, "Directional Macro-Cell Channel Characterization from Urban Measurements," *IEEE Transactions on Antennas and Propagation*, vol. 48, no. 2, pp. 137-146, February 2000.

[87] Y. Kung, J. C. Chen & R. E. Hudson, "Maximum-Likelihood Acoustic Source Localization: Experimental Results," *IEEE International Conference on Acoustcis, Speech & Signal Processing*, vol. 3, pp. 2949-2952, 2002.

[88] H. Lai, K. Bell & H. Cox, "DOA Estimation Using Vector Sensor Arrays," *Asilomar Conference*, pp. 293-297, 2008.

[89] M. Larsson, "Spatio-Temporal Channel Measurements at 1800 MHz for Adaptive Antennas," *IEEE Vehicular Technology Conference*, vol. 1, pp. 376-380, Fall 1999.

[90] E. E. L. Lau & W. Y. Chung, "Accuracy Refinement Algorithm for Mobile Target Location Tracking by Radio Signal Strength Indication Approach," *IEICE Transactions on Fundamentals of Electronics, Communications and Computer Sciences*, vol. E91-A, no. 7, pp. 1659-1666, July 2008.

[91] J. Laurila, A. F. Molisch & E. Bonek, "Influence of the Scatterer Distribution on Power Delay Profiles and Azimuthal Power Spectra of Mobile radio Channels," *International Symposium Spread Spectrum Technology & Applications*, vol. 1, pp. 267-271, 1998.

[92] J. Laurila, K. Kalliola, M. Toeltsch, K. Hugl, P. Vainikainen & E. Bonek, "Wide-Band 3-D Characterization of Mobile Radio Channels in Urban Environment," *IEEE Transactions on Antennas & Propagation*, vol. 50, no. 2, pp. 233-243, February 2002.

[93] C. L. LeBlanc, *Handbook of Hydrophone Element Design Technology*, Naval Underwater Systems Center Technical Report 5813, 1978.

[94] . Ledeczi, G. Kiss, B. Feher, P. Volgyesi & G. Balogh, "Acoustic Source Localization Fusing Sparse Direction of Arrival Estimates," *International Workshop on Intelligent Solutions in Embedded Systems*, 2006.

[95] C. B. Leslie, J. M. Kendall & J. L. Jones, "Hydrophone for Measuring Particle Velocity," *Journal of the Acoustical Society of America*, vol. 28, no. 4, pp. 711-715, July 1956.

[96] D. Li & Y. H. Hu, "Energy-based Collaborative Source Localization Using Acoustic Microsensor Array," *EURASIP Journal on Applied Signal Processing*, vol. 4, pp. 321-337, 2003.

[97] K. M. Li & K. K. Lu, "Propagation of Sound in Long Enclosures," *Journal of Acoustical Society of America*, vol. 116, no. 5, pp. 2759-2770, November 2004.

[98] J. C. Liberti & T. S. Rappaport, "A Geometrically Based Model for Line-of-Sight Multipath Radio Channels," *IEEE Vehicular Technology Conference*, vol. 2, pp. 844-848, 1996.

[99] J. C. Liberti, Jr. & T. S. Rappaport, *Smart Antennas for Wireless Communications: IS-95 and Third Generation CDMA Applications*, Upper Saddle River, New Jersey, USA: Prentice Hall, 1999.

[100] S. Y.-D. Lien & M. Cherniakov, "Analytical Approach for Multipath Delay Spread Power Distribution," *IEEE Global Telecommunications Conference*, pp. 3680-685, 1998.

[101] X. Liu, J. Xiang & Y. Zhou, "Passive Tracking and Size Estimation of Volume Target Based on Acoustic Vector Intensity," *Chinese Journal of Acoustics*, vol. 20, no. 3, pp. 225-238, 2001.

[102] M. E. Lockwood & D. L. Jones, "Beamformer Performance with Acoustic Vector Sensors in Air," *Journal of the Acoustical Society of America*, vol. 119, no. 1, pp. 608-619, January 2006.

[103] M. P. Lotter & P. van Rooyen, "Modeling Spatial Aspects of Cellular CDMA/SDMA Systems," *IEEE Communications Letters*, vol. 3, no. 5, pp. 128-131, May 1999.

[104] D. Lubman, "Antifade Sonar Employs Acoustic Field Diversity to Recover Signals from Multipath Fading," in *Design, Performance and Applications*, pp. 335-344, Woodburg, New York, U.S.A.: AIP Press, 1996.

[105] D. Lubman, "Antifade Sonar Employs Acoustic Field Diversity to Recover Signals from Multipath Fading," in *Design, Performance and Applications*, pp. 335-344, Woodburg, New York, U.S.A.: AIP Press, 1996.

[106] Q. Lu, S. Yang, J. Zhang & S. Piao, "High Resolution DOA Estimation in Beam Space Based on Acoustic Vector-Sensor Array," *Journal of Harbin Engineering University*, vol. 25, no. 4, pp. 440-445, August 2004.

[107] N. Ma & C. S. Chia, "Target Localization by Two Fixed Non-Coherent Passive Linear Arrays," *IEEE Oceans Conference*, 2008.

[108] S. Mahmoud, Z. M. Hussain & P. OShea, "Space-Time Geometrical-Based Channel Models: A Comparative Study," *Australian Telecommunications, Networks and Applications Conference*, 2003.

[109] G. Mao, B. Fidan & B. D. O. Anderson, "Wireless Sensor Network Localization Techniques," *Computer Networks*, vol. 51, pp. 2529-2553, July 2007.

[110] B. H. Maranda, "The Statistical Accuracy of an Arctangent Bearing Estimator," *IEEE Oceans Conference*, vol. 4, pp. 2127-2132, 2003.

[111] U. Martin, "Spatio-temporal Radio Channel Characteristics in Urban Macrocells," *IEE Proceedings on Radar, Sonar, and Navigation*, vol. 145, no. 1, pp. 42-49, February 1998.

[112] E. Masazade, R. Niu, P. K. Varshney & M. Keskinoz, "An Energy Efficient Iterative Method for Source Localization in Wireless Sensor Networks," *IEEE Annual Conference on Information Sciences and Systems*, pp. 623-628, 2009.

[113] P. A. Matthews, D. Molkdar & B. Mohebbi, "Direction of Arrival and Frequency Response Measurements at UHF," *International Conference on Mobile Radio & Personal Communications*, pp. 43-47, 1989.

[114] J. D. Maynard, E. G. William & Y. Lee, "Nearfield Acoustic Holography: I. Theory of Generalized Holography and the Development of NAH," *Journal of Acoustical Society of America*, vol. 78, no. 4, pp. 1395-1413, October 1985.

[115] J. A. McConnell, "Analysis of a Compliantly Suspended Acoustic Velocity Sensor," *Journal of the Acoustical Society of America*, vol. 113, no. 3, pp. 1395-1405, March 2003.

[116] J. F. McEachern, J. A. McConnell, J. Jamieson & D. Trivett, "ARAP - Deep Ocean Vector Sensor Research Array," *IEEE Oceans Conference*, 2006.

[117] C. Mellet, F. Letourneaux, F. Poisson & C. Talotte, "High Speed Train Noise Emission: Latest Investigation of the Aerodynamic/Rolling Noise Contribution," *Journal of Sound & Vibration*, no. 293, pp. 535-546, June 2006.

[118] S. Miron, N. Le Bihan & J. I. Mars, "Quaternion-MUSIC for Vector-Sensor Array Processing," *IEEE Transactions on Signal Processing*, vol. 54, no. 4, pp. 1218-1229, April 2006.

[119] P. E. Mogensen, K. I. Pedersen, P. Leth-Espensen, B. Fleury, F. Frederiksen, K. Olesen & S. L. Larsen, "Preliminary Measurement Results from an Adaptive Antenna Array Testbed for GSM/UMTS," *IEEE Vehicular Technology Conference*, vol. 3, pp. 1592-1596, 1997.

[120] Y. Moritoh, Y. Zenda, & K. Nagakura, "Noise Control of High Speed Shinkansen," *Journal of Sound & Vibration*, no. 193, pp. 319-334, May 1996.

[121] P. M. Morse & K. U. Ingard, *Theoretical Acoustics*, New York, U.S.A.: McGraw-Hill, 1968.

[122] S. Muhammed, Al-Ahmadi & A. U. H. Shiekh, "Spatial Domain Modeling of Microcellular Systems Operating in Multipath Nakagami Channels," *Personal, Indoor and Mobile Radio Communications Conference*, vol. 4, pp. 1942-1946, September 2002.

[123] K. G. Nagananda & G. V. Anand "Subspace Intersection Method of Bearing Estimation in Shallow Ocean Using Acoustic Vector Sensors," *European Signal Processing Conference*, 2008

[124] A. Nehorai & E. Paldi, "Performance Analysis of Two Direction Estimation Algorithms Using an Acoustic Vector-Sensor Array Processing," *IEEE International Conference on Acoustics, Speech, Signal Processing*, vol. 4, pp. 360-363, April 1993.

[125] A. Nehorai & E. Paldi, "Acoustic Vector-Sensor Array Processing," *IEEE Transactions on Signal Processing*, vol. 42, no. 10, pp. 2481-2491, September 1994.

[126] A. Nehorai & P. Tichavský, "Cross-Product Algorithms for Source Tracking Using an EM Vector Sensor," *IEEE Transactions on Signal Processing*, vol. 47, no. 10, pp. 2863-2867, October 1999.

[127] W. T. Ng & V. K. Dubey, "Comments on "On the Doppler Spectrum at the Mobile Unit Employing a Directional Antenna," " *IEEE Communications Letters*, vol. 6, no. 11, pp. 472-474, November 2002.

[128] W. T. Ng & V. K. Dubey, "Effect of Employing Directional Antennas on Mobile OFDM System With Time-Varying Channel, IEEE Communications Letters, vol. 7, no. 4, pp. 165-167, April 2003.

[129] J. C. Nickles, G. L. Edmonds, R. A. Harriss, F. H. Fisher, W. S. Hodgkiss, J. Giles & G. D'Spain, "A Vertical Array of Directional Acoustic Sensors," *IEEE Oceans Conference*, vol. 1, pp. 340-345, 1992.

[130] Y. Nishi & T. Ohtsuki, "A Distributed Localization with Unknown Attenuation Coefficient in Wireless Sensor Networks," *Asia-Pacific Conference on Communications*, 2008.

[131] R. Niu & P. K. Varshney, "Target Location Estimation in Sensor Networks With Quantized Data," *IEEE Transactions on Signal Processing*, vol. 54, no. 12, pp. 4519-4528, December 2006.

[132] A. Y. Nooralahiyan, M. Dougherty, D. McKeown & H. R. Kirby, "A Field Trial of Acoustic Signature Analysis for Vehicle Classification," *Transportation Research*, vol. 5, no. 3-4, pp. 165-177, 1997.

[133] A. Y. Olenko, K. T. Wong & E. H.-O. Ng, "Analytically Derived TOA-DOA Statistics of Uplink/Downlink Wireless Multipaths Arisen from Scatterers on an Hollow-Disc Around the Mobile," *IEEE Antennas & Wireless Propagation Letters*, vol. 2, issue 22, pp. 345-348, 2003.

[134] A. Y. Olenko, K. T. Wong & M. Abdulla, "Analytically Derived TOA-AOA Distributions of Uplink/Downlink Wireless-Cellular Multipaths Arisen from Scatterers with an Inverted-Parabolic Spatial Distribution Around the Mobile," *IEEE Signal Processing Letters*, vol. 9, no. 7, pp. 516-519, July 2005.

[135] A. Y. Olenko, K. T. Wong, S. A. Qasmi & J. Ahmadi-Shokouh, "Analytically Derived Uplink/Downlink TOA & 2D-DOA Distributions with Scatterers in a 3D Hemispheroid Surrounding the Mobile," *IEEE Transactions on Antennas & Propagation*, vol. 54, no. 9, pp. 2446-2454, September 2006.

[136] J. W. Parkins, S. D. Sommerfeldt & J. Tichy, "Error Analysis of a Practical Energy Density Sensor," *Journal of the Acoustical Society of America*, vol. 108, no. 1, pp. 211-222, July 2000.

[137] K. I. Pedersen, B. H. Fleury & P. E. Mogensen, "High Resolution of Electromagnetic Waves in Time-Varying Radio Channels," *IEEE International Symposium on Personal, Indoor & Mobile Radio Communications*, vol. 2, pp. 650-654, 1997.

[138] K. I. Pedersen, P. E. Mogensen & B. H. Fleury, "Spatial Channel Characteristics in Outdoor Environments and Their Impact on BS Antenna System Performance," *IEEE Vehicular Technology Conference*, vol. 2, pp. 719-723, 1998.

[139] K. I. Pedersen, P. E. Mogensen & B. H. Fleury, "Dual-Polarized Model of Outdoor Propagation Environments for Adaptive Antennas," *IEEE Vehicular Technology Conference*, vol. 2, pp. 990-995, Spring 1999.

[140] K. I. Pedersen, P. E. Mogensen & B. H. Fleury, "A Stochastic Model of the Temporal and Azimuthal Dispersion Seen at the Base Station in Outdoor Propagation Environments," *IEEE Transactions on Vehicular Technology*, vol. 49, no. 2, pp. 437-447, March 2000.

[141] P. Pertila & M. Parviainen, "Robust Speaker Localization in Meeting Room Domain," *IEEE International Conference on Acoustcis, Speech & Signal Processing*, vol. IV, pp. 497-500, 2007.

[142] P. Petrus, J. H. Reed & T. S. Rappaport, "Effects of Directional Antennas at the Base Station on the Doppler Spectrum," *IEEE Communications Letters*, vol. 1, no. 2, pp. 40-42, March 1997.

[143] P. Petrus, J. H. Reed & T. S. Rappaport, "Geometrical-Based Statistical Macrocell Channel Model for Mobile Environments," *IEEE Transactions on Communications*, vol. 50, no. 3, pp. 495-502, March 2002.

[144] R. J. Piechocki, G. V. Tsoulos & J. P. McGeehan, "Simple General Formula for PDF of Angle of Arrival in Large Cell Operational Environments," *Electronics Letters*, vol. 34, no. 18, pp. 1784-1785, September 3, 1998.

[145] A. D. Pierce, *Acoustics—An Introduction to its Physical Principles and Applications.* New York: McGraw-Hill, 1989.

[146] B. Porat, Digital Processing of Random Signals: Theory and Methods. Englewood Cliffs, NJ: Prentice-Hall, 1994.

[147] A. J. Poulsen, R. R. Nadakuditi & A. B. Baggeroer, "Robust Adaptive Vector Sensor Processing in the Presence of Mismatch and Finite Sample Support," *SAM*?????, pp. 473-477, 2008.

[148] N. Qi & T. Tian, "Acoustic Vector Hydrophone Array Supergain Energy Flux Beamforming," *International Conference on Signal Processing*, vol. 4, 2006.

[149] A. Rabaoui, Z. Lachiri & N. Ellouze, "Automatic Environmental Noise Recognition," *IEEE International Conference on Industrial Technology*, vol. 3, pp. 1670-1675, 2004.

[150] I. Sarris & A. R. Nix "Design and Performance Assessment of High-Capacity MIMO Architectures in the Presence of a Line-of-Sight Component," *IEEE Transactions on Vehicular Technology*, vol. 56, no. 4, pp. 2194-2202, July 2007.

[151] B. Schulte-Werning, K. Jager, R. Strube & L. Willenbrink "Recent Developments in Noise Research at Deutsche Bahn (Noise Assessment, Noise Source Localization and Specially Monitored Track)," *Journal of Sound & Vibration*, no. 267, pp. 689-699, October 2003.

[152] S. Y. Seidel, T. S. Rappaport, S. Jain, M. L. Lord & R. Singh, "Path Loss, Scattering, and Multipath Delay Statistics in Four European Cities for Digital Cellular and Microcellular Radiotelephone," *IEEE Transactions on Vehicular Technology*, vol. 40, no. 4, pp. 721-730, November 1991.

[153] V. A. Shchurov, "Coherent and Diffuse Fields of Underwater Acoustic Ambient Noise," *Journal of the Acoustical Society of America*, vol. 90, no. 2, part 1, pp. 991-1001, August 1991.

[154] V. A. Shchurov, V. I. Ilyichev, V. P. Kuleshov & M. V. Kuyanova, "The interaction of Energy Flows of Underwater Ambient Noise and a Local Source," *Journal of the Acoustical Society of America*, vol. 90, no. 2, part 1, pp. 1002-1004, August 1991.

[155] V. A. Shchurov, V. I. Ilyichev & V. P. Kuleshov, "Ambient Noise Energy Motion in the Near Surface Layer in Ocean Wave-Guide," *Journal de Physique*, vol. 4, no. 5, part 2, pp. 1273-1276, May 1994.

[156] V. A. Shchurov & M. V. Kuyanova, "Use of Acoustic Intensity Measurements in Underwater Acoustics (Modern State and Prospects)," *Chinese Journal of Acoustics*, vol. 18, no. 4, pp. 315-326, 1999.

[157] V. Shchurov, *Vector Acoustics of the Ocean*, Vladivostok, Russia: Dalnauka, 2006.

[158] X. Sheng & Y. H. Hu, "Maximum Likelihood Multiple-Source Localization Using Acoustic Energy Measurements with Wireless Sensor Networks," *IEEE Transactions on Signal Processing*, vol. 53, no. 1, pp. 44-54, January 2005.

[159] Q. Shi & C. He, "A New Incremental Optimization Algorithm for ML-Based Source Localization in Sensor Networks," *IEEE Signal Processing Letters*, vol. 15, pp. 45-48, 2008.

[160] J. C. Shipps & K. Deng, "A Miniature Vector Sensor for Line Array Applications," *IEEE Oceans Conference*, vol. 5, pp. 2367-2370, 2003.

[161] J. C. Shipps & B. M. Abraham, "The Use of Vector Sensors for Underwater Port and Waterway Security," *ISA/IEEE Sensors for Industry Conference*, pp. 41-44, 2004.

[162] J. Shirahama & T. Ohtsuki, "RSS-Based Localization in Environments with Different Path Loss Exponent for Each Link," *IEEE Vehicular Technology Conference*, pp. 1509-1513, 2008.

[163] M. T. Silvia & R. T. Richards, "A Theoretical and Experimental Investigation of Low-Frequency Acoustic Vector Sensors," *IEEE Oceans Conference*, vol. 3, pp. 1886-1897, 2002.

[164] M. T. Simsim, N. M. Khan, R. Ramer & P. B. Rapajic, "Time of Arrival Statistics in Cellular Environments," *IEEE Vehicular Technology Conference*, vol. 6, pp. 2666-2670, Spring 2006.

[165] P. J. Stein, S. E. Euerle, R. K. Menoche & R. E. Janiesch, "Pressure Gradient Sensors for Bearing Determination in Shallow Water Tracking Ranges," in *Design, Performance and Applications*, pp. 359-373, Woodburg, New York, U.S.A.: AIP Press, 1996.

[166] M. Steinbauer, A. F. Molisch & E. Bonek, "the Double-Directional Radio Channel," *IEEE Antennas & Propagation Magazine*, vol. 43, no. 4, pp. 51-63, August 2001.

[167] M. R. Stinson, "A Note on the Use of an Approximate Formula to Predict Sound Fields above an Impedance Plane due to a Point Source," *Journal of Acoustical Society of America*, vol. 98, no. 3, pp. 1810-1812, April 1995.

[168] J.-I. Takada, J. Fu, H. Zhu & T. Kobayashi, "Spatio-Temporal Channel Characterization in a Suburban Non Line-of-Sight Microcellular Environment," *IEEE Journal on Selected Areas in Communications*, vol. 20, no. 3, pp. 532-538, April 2002.

[169] J. Taketsugu & J. Yamakita, "A Modification Strategy of Maximum Likelihood Method for Localization Estimation Based on Received Signal Strength in Sensor Networks," *IEICE Transactions on Fundamentals of Electronics, Communications and Computer Sciences*, vol. E90-A, no. 5, pp. 1093-1105, May 2007.

[170] S. Tanaka, A. Harada, M. Sawahasji & F. Adachi, "Experiments on Coherent Adaptive Antenna Array Diversity for Wideband DS-CDMA Mobile Radio," *IEEE Journal on Selected Areas in Communications*, vol. 18, no. 8, pp. 1495-1504, August 2000.

[171] R. S. Thoma, D. Hampicke, A. Richter, G. Sommerkorn, A. Schneider, U. Trautwein & W. Wirnitzer, "Identification of Time-Variant Directional Mobile Radio Channels," *IEEE Transactions on Instrumentation & Measurement*, vol. 49, no. 2, pp. 357-364, April 2000.

[172] P. Tichavský, K. T. Wong & M. D. Zoltowski, "Near-Field/Far-Field Azimuth and Elevation Angle Estimation Using a Single Vector Hydrophone," *IEEE Transactions on Signal Processing*, vol. 49, no. 11, pp. 2498-2510, November 2001.

[173] W. M. To & S. M. Yung, "Power Estimation of Sound Sources on Low-Speed Electric Trains Using a Deconvolution Approach," *Journal of Acoustical Society of America* vol. 104, no. 4, pp. 2350-2358, April 1999.

[174] M. Toeltsch, J. Laurila, A. F. Molisch, K. Kalliola, P. Vainikainen, & E. Bonek, "Spatial Characterization of Urban Mobile Radio Channels," *IEEE Vehicular Technology Conference*, vol. 1, pp. 204-208, Spring 2001.

[175] J. D. van der Toorn, H. Hendriks & T. C. van den Dool, "Measuring TGV Source Strength with Syntacan," *Journal of Sound & Vibration*, no. 193, pp. 113-121, May 1996.

[176] J. W. van Honschoten, V. B. Svetovoy, G. J. M. Krijnen & M. C. Elwenspoek, "Optimization of a Thermal Flow Sensor for Acoustic Particle Velocity Measurements," *Journal of Microelectromechanical Systems*, vol. 14, no. 3, pp. 436-443, June 2005.

[177] D. R. Van Rheeden & S. C. Gupta, "A Geometric Model for Fading Correlation in Multipath Radio Channels," *IEEE International Conference Communications*, vol. 3, pp. 1655-1659, 1998.

[178] H. L. Van Trees, *Detection, Estimation, and Modulation Theory, Part IV: Optimum Array Processing*, New York, U.S.A.: Wiley, 2002.

[179] B. D. Van Veen & K. M. Buckley, "Beamforming: A Versatile Approach to Spatial Filtering," *IEEE Acoustics, Speech & Signal Processing Magazine*, vol. 5, no. 2, pp. 4-24, April 1988.

[180] C. Wan, A. Kong & C. Liu, "A Comparative Study of DOA Estimation Using Vector/Gradient Sensors," *IEEE Oceans Conference Asia-Pacific*, 2006.

[181] Y. H. Wang, J. Q. Zhang, B. Hu & J. He, "Hypercomplex Model of Acoustic Vector Sensor Array with Its Application for the High Resolution Two Dimensional Direction of Arrival Estimation," *IEEE International Instrumentation and Measurement Technology Conference*, 2008.

[182] G. Wang & K. Yang, "Efficient Semidefinite Relaxation for Energy-Based Source Localization in Sensor Networks," *IEEE International Conference on Acoustics, Speech and Signal Processing*, pp. 2257-2260, 2009.

[183] J. Weng & K. Y. Guentchev, "Three-dimensional Sound Localization from a Compact Non-coplanar Array of Microphones Using Tree-based Learning," *Journal of Acoustical Society of America*, vol. 110, no. 1, pp. 310-323, July 2001.

[184] P. Wetta & B. Beguet, "Experimental Analysis of Wheel/Rail Noise by Near Field Acoustical Imaging," *Journal of Sound & Vibration*, no. 120, part 2, pp. 255-265, January 1988.

[185] B. Widrow, P. E. Mantey, L. J. Griffiths & B. B. Goode, "Adaptive Antenna Systems," *Proceedings of the IEEE*, no. 12, vol. 55, pp. 2143-2159, December 1967.

[186] M. Wirnsberger, M. G. Dittrich, J. Lub, G. Pollone, M. Kalivoda, P. V. Buchem, W. Hanreich & P. Fodiamn, *Methodologies and Actions for Rail Noise and Vibration Control: Final Report for Publication*, METARAIL Consortium, December 1999.

[187] K. T. Wong & M. D. Zoltowski, "Closed-form Underwater Acoustic Direction-Finding with Arbitrarily Spaced Vector-Hydrophones at Unknown Locations," *IEEE Journal of Oceanic Engineering*, vol. 22, no. 3, pp. 566-575, July 1997.

[188] K. T. Wong & M. D. Zoltowski, "Extended-Aperture Underwater Acoustic Multi-source Azimuth/Elevation Direction-Finding Using Uniformly But Sparsely Spaced Vector Hydrophones," *IEEE Journal of Oceanic Engineering*, vol. 22, no. 4, pp. 659-672, October 1997.

[189] K. T. Wong & M. D. Zoltowski, "Root-MUSIC-Based Azimuth-Elevation Angle-of-Arrival Estimation with Uniformly Spaced but Arbitrarily Oriented Velocity Hydrophones," *IEEE Transactions on Signal Processing*, vol. 47, no. 12, pp. 3250-3260, December 1999.

[190] K. T. Wong, "Adaptive Source Localization & Blind Beamforming for Underwater Acoustic Wideband Fast Frequency-Hop Signals of Unknown Hop Sequences & Unknown Arrival Angles Using a Vector-Hydrophone," *IEEE Wireless Communications & Networking Conference*, vol. 2, pp. 664-668, 1999.

[191] K. T. Wong & M. D. Zoltowski, "Self-Initiating MUSIC-Based Direction Finding in Underwater Acoustic Particle Velocity-Field Beamspace," *IEEE Journal of Oceanic Engineering*, vol. 25, no. 2, pp. 262-273, April 2000.

[192] K. T. Wong & M. K. Awad, "Source Tracking with a Vector-Hydrophone," *IEEE Oceans Conference Asia-Pacific*, 2006.

[193] H. Wu, M. Siegel & P. Khosla, "Vehicle Sound Signature Recognition by Frequency Vector Principal Component Analysis," *IEEE Transactions on Instrumentation & Measurement*, vol. 48, no. 5, pp. 1005-1009, October 1999.

[194] Y. I. Wu, K. T. Wong & S. K. Lau, "Beacon-Aided Adaptive Localization of Sound-Sources aboard a Pass-By Rail-Car Using a Track-Side Acoustic Microphone Array," *Inter-Noise Conference*, Shanghai, China, 26-29 October, 2008.

[195] Y. I. Wu, K. T. Wong & S. K. Lau, "Beacon-Aided Adaptive Azimuth-Elevation Localization of Sound-Sources aboard a Pass-By Rail-Car Using a Track-Side Acoustic Microphone Planar Array," *International Conference on Sensing Technology*, Tainan, Taiwan, 30 November to 3 December, 2008.

[196] Y. Xu, Z. Liu & J. Cao, "Perturbation Analysis of Conjugate MI-ESPRIT for Single Acoustic Vector-Sensor-Based Noncircular Signal Direction Finding," *Signal Processing*, vol. 87, no. 7, pp. 1597-1612, July 2007.

[197] C. T. Xuan, E. Kim & I. Koo, "An Efficient RSS-Based Localization Scheme with Calibration in Wireless Sensor Networks," *IEICE Transactions on Communications*, vol. E91-B, no. 12, pp. 4013-4017, December 2008.

[198] J. Yick, B. Mukherjee & D. Ghosal, "Wireless Sensor Network Survey," *Computer Network*, vol. 52, pp. 2292-2330, April 2008.

[199] Y. Yuan, B. Zhang, D. Fan & G. Tong "DFT and PSD for Estimating DOA with an Active Acoustic Array," *IEEE International Conference on Automation and Logistics*, pp. 694-699, 2008.

[200] G. Yunchao, S. Enfang, L. Baifeng & S. Zhengyan, "Application of Complex Empirical Mode Decomposition in Separation of Multiple Targets Using a Single Vector Sensor," *IEEE International Conference Neural Networks & Signal Processing*, pp. 294-298, 2008.

[201] G. Yunchao, S. Enfang & S. Zhengyan, "Comparison of EMD and Complex EMD in Signal Processing," *Congress on Image and Signal Processing*, pp. 141-145, 2008.

[202] L. Yun-fei & Z. Cui-e, "A Study of Channel Estimation in OFDM System Based on a Single Vector Sensor for Underwater Acoustic Communications," *International Conference on Wireless Communications, Networking and Mobile Computing*, 2008.

[203] W. Zamojski, J. Mazurkiewicz & T. Walkowiak, "Mobile Object Localisation Based on Acoustic Information," *IEEE International Symposium on Industrial Electronics*, vol. 3, pp. 813-818, 1997.

[204] R. Zemek, S. Hara, K. Yanagihara & K. Kitayama, "A Traffic Reduction Method for Centralized RSSI-Based Location Estimation in Wireless Sensor Networks," *IEICE Transactions on Communications*, vol. E91-B, no. 6, pp. 1842-1852, June 2008.

[205] D. Zha & T. Qiu, "Underwater Sources Location in Non-Gaussian Impulsive Noise Environments," *Digital Signal Processing*, vol. 16, pp. 149-163, March 2006.

[206] D. Zha, "Underwater 2-D Source Localization Based On Fractional Order Correlation Using Vector Hydrophone," *Congress on Image and Signal Processing*, pp. 31-34, 2008.

[207] X. Zhao, J. Kivinen, P. Vainikainen & K. Skog, "Propagation Characteristics for Wideband Outdoor Mobile Communications at 5.3 GHz," *IEEE Journal on Selected Areas in Communications*, vol. 20, no. 3, pp. 507-510, April 2002.

[208] H. Zhu, J. Fu, J.-i. Takada, K. Araki, H. Masui, M. Ishii, K. Sakawa, H. Shimizu & T. Kobayahsi, "A Spatio-Temporal Channel Measurement and Ray-Tracing Validation in Suburban Microcell Environments," *IEEE Antennas & Propagation Society International Symposium*, vol. 2, pp. 1138-1141, 2000.

[209] H. Zhu, J. Takada & T. Kobayahsi, "The Verification of a Deterministic Spatio-Temporal Channel Modeling Approach by Applying a Deconvolution Technique in the Measurement," *IEEE Vehicular Technology Conference*, vol. 1, pp. 362-366, Spring 2001.

[210] M. D. Zoltowski & K. T. Wong, "Closed-Form Eigenstructure-Based Direction Finding Using Arbitrary but Identical Subarrays on a Sparse Uniform Cartesian Array Grid," *IEEE Transactions on Signal Processing*, vol. 48, no. 8, pp. 2205-2210, August 2000.

[211] N. Zou, C. C. Swee & B. A. L. Chew, "Vector Hydrophone Array Development and Its Associated DOA Estimation Algorithms," *IEEE Oceans Conference Asia-Pacific*, 2006.